UNIVERSITÀ DEGLI STUDI DI MILANO

SCUOLA DI DOTTORATO IN FISICA, ASTROFISICA E FISICA APPLICATA

DIPARTIMENTO DI FISICA

CORSO DI DOTTORATO DI RICERCA IN FISICA, ASTROFISICA E FISICA APPLICATA, CICLO XXIII

Synchrotron radiation based characterization of complex morphology clusters in the gas-phase

Settore Scientifico Discliplinare FIS/03

Tesi di Dottorato di:

Michele Devetta

Supervisore: Prof. Paolo Milani

Coordinatore: Prof. Marco Bersanelli

Anno Accademico 2009/2010

a mio nonno Piero...

Contents

I Introduction **5**

1 Clusters **8**

1.1 Gas-phase Synthesis 9

1.2 Characterization Techniques 9

1.2.1 Mobility Analysis 10

1.2.2 Near edge X-ray absorption fine structure spectroscopy 16

1.2.3 Photo-electron spectroscopy 16

1.2.4 Photo-fragmentation in intense photon beams 17

2 Supersonic Beam Apparatus for gas-phase cluster characterization **21**

2.1 Setup for time-resolved XAS of free clusters 22
Article: *CESyRa: A versatile setup for core-level absorption experiments on freemetallic clusters using synchrotron radiation*, J. El. Spec. 166–167, pp. 28–37 (2008)

2.2 Setup for time-resolved photo-electron spectroscopy of free clusters . 33

2.3 Setup for photo-fragmentation of free clusters 35

II Results and discussion **42**

3 *sp*-rich carbon clusters **43**

3.1 *In-situ* Raman spectroscopy of carbon 44

3.2 Stabilization of *sp* carbon chains in an sp^2 matrix 45

Article: *Effect of Axial Torsion on sp Carbon Atomic Wires*, Phys. Rev. Lett. 102, 245502 (2009)

3.3 NEXAFS spectroscopy of deposited carbon films 50

3.4 NEXAFS spectroscopy of carbon clusters in the gas-phase 51

Article: *sp hybridization in free carbon nanoparticles –presence and stability observed by Near Edge X-ray Absorption Fine Structure spectroscopy*, ChemComm, *accepted* (2010)

4 Accessing the fractal dimension of free clusters **57**

4.1 First results of SBMA in XAS experiments 57

4.2 SBMA with FEL 63

4.2.1 Estimate of the original mass distribution 63

4.2.2 Event-by-event charge assignment 65

4.2.3 Estimate of gas density and velocity 66

4.2.4 Accessing fractal dimension 70

4.3 Conclusions 71

5 Photo-fragmentation of titanium clusters **73**

5.1 Analysis of fragmentation 73

5.1.1 Fragment yield 74

5.1.2 Ion mass spectra 76

5.1.3 Fragments kinetic energy 77

5.2 Interpretation of fragmentation: Montecarlo simulations 79

5.2.1 Genetic algorithm framework 79

5.2.2 FEL-cluster interaction model 80

5.2.3 Conclusions 83

6 Photo-electron spectroscopy of lead clusters **84**

6.1 Mass distribution of lead clusters 84

6.2 Analysis of XPS line-shape 87

7 Conclusions and perspectives **94**

Bibliography **96**

Part I

Introduction

Cluster science is a rather new and rapidly developing field of research, motivated by concurrent interests at both fundamental and applied level. First of all one can recognize the fascinating fundamental question of how the properties of bulk materials evolve from the corresponding ones of single atoms, but clusters attract great interest also in the ever-growing field of nanotechnology, where they can be employed as building blocks to assemble novel nanostructured materials with interesting properties.

To fully understand and eventually control the properties of these materials it is fundamental to reach an insight into the properties of the original particles, without the modifications that are necessarily introduced by the interaction with the supporting surface and between clusters themselves. For this reason it is very interesting to study clusters in the gas-phase, completely isolated from the surrounding environment.

Laser optical and photo-electron spectroscopy techniques have proven to be very powerful to characterize the electronic properties of clusters, while the most advanced synchrotron radiation based characterization techniques that offer larger insight for nano-scale objects characterization have found to date only little application to free isolated nanostructures due to the very low density of gas-phase samples. The advent of intense short-wavelength light sources such as the new generation of FELs (Free Electron Lasers) is expected to bridge the gap between the most advanced characterization methods and the state of the art of free particles preparation methods. The combination of such sources to isolated clusters shows a strong additional potential for the observation of new physical phenomena from matter under extreme conditions.

My work reports on the recent developments of free particle characterization methods with synchrotron radiation carried out at the Molecular Beams Laboratory of the Università degli Studi di Milano in collaboration with leading international groups.

This thesis is divided into two main parts. In the first one a brief introduction is given about the characterization techniques we used (in chapter 1) and the apparatus we originally developed for the experiments (in chapter 2).

The second part is devoted to the description and discussion of the results of

the experiments:

- Chapter 3 reports on the X-ray absorption experiment on complex carbon clusters; it allowed to identify an evolution on the millisecond time-scale of the content of carbon atoms with *sp* hybridization with the residence time in the aggregation region.
- Chapter 4 reports the results of a novel technique, that we developed and named Supersonic Beam Mobility Analysis. This technique is used to characterize the nano-scale morphology of clusters seeded in a molecular beam, by means of an accurate measurement of their coupling with the carrier gas in a supersonic expansion.
- Chapter 5 reports experiments of photo-fragmentation of titanium clusters in an intense FEL photon beam.
- Chapter 6 reports the characterization of the complex morphology of lead clusters by means of combined mass and photo-electron spectroscopies.

Chapter 1

Clusters

Atomic clusters are aggregates of atoms, from few to several thousands, with size up to tens of nanometers. The term can be used, and will be used, as a synonym of nanoparticle, as the generally given definitions of the two terms refer to classes of objects with partially overlapping size ranges.

The first interest in cluster science is to follow the evolution of the geometric and electronic structure as a function of size, to understand the link between isolated atoms and the bulk solid. The electronic structure for instance changes drastically with size, from localized atomic orbitals over molecular-like orbitals for small clusters to band-like states for large clusters approaching the infinite solid.

Moreover, clusters have also triggered great interest for applications in the growing field of nanotechnology, opening the way to the synthesis of new materials based on a bottom-up building-block approach.

Clusters (or nanoparticles) can be synthesized mainly following two methodologies: the chemical synthesis and the gas-phase vapor condensation.

The first approach has the advantage of simplicity, quite good reproducibility and defined size distribution, but presents the great disadvantage of making the characterization of the products quite difficult because the particles cannot be analyzed isolated, without the interaction with the fluid in which they are dispersed or a surface on which they are deposited.

On the other hand gas-phase synthesis, despite the general need of much more expensive and complicated experimental setup, gives the possibility to characterize

the particles as isolated objects, i.e. unaffected by the environment.

1.1 Gas-phase Synthesis

Gas-phase synthesis of clusters is often based on the condensation of a vapor of the material of interest in an inert atmosphere.

If the precursor for cluster formation is already in the gas-phase, like is the case for molecular or rare gas clusters, it is generally sufficient to produce an adiabatic expansion through a nozzle into a vacuum, to obtain the clusters formation via vapor condensation. The process is well known and many empirical scaling laws have been developed to link the size distribution of the clusters to the stagnation pressure and temperature of the gas prior to expansion.

For refractory material, like metals, the vapor can be obtained by the non-thermal vaporization of a solid target. This can be accomplished in many ways: violent heating by an intense laser pulse or arc discharge [46], by magnetron [48] or pulsed sputtering [3]; only for a limited number of metals, clusters can be formed by direct evaporation in a crucible [37].

The vapor is condensed in a bath of inert gas, then expanding in a free jet and thus forming a molecular beam seeded with clusters. After the transition to the molecular regime, clusters are in all respects isolated from each other and from the surrounding environment. Depending on the vapor temperature and thermodynamic conditions during aggregation time, different morphologies may be synthesized for clusters of refractory materials.

1.2 Characterization Techniques

As discussed in the previous section, gas-phase production of clusters has the great advantage of decoupling their properties from that of a matrix or substrate. However characterization of nanoparticles in the gas-phase is a non-trivial task for many reasons, first of all the high dilution of the sample, and a great improvement of standard techniques is needed to make them suitable for this purpose.

In the following sections I will present the principles of four characterization techniques that I contributed to develop during my PhD thesis and that I employed

for the characterization of carbon and metal clusters with complex structure and morphology.

1.2.1 Mobility Analysis

When a particle moves into a dispersive medium it loses energy because of interactions. So when a constant external force is applied, the particle velocity saturates mean terminal velocity, that is the equilibrium point between the energy given by the external force and that dispersed by the interactions. The ratio between the terminal velocity and the applied force is defined as the mobility:

$$\mu = \frac{v_d}{F} \tag{1.1}$$

Mobility is in general proportional to the cross-section of the particle with respect to the medium in which is immersed and so it can be exploited to investigate the properties of the particle.

One example of the application of this concept is the study of nanoparticles in aerosols. In this case solid particles are suspended in a gas flow. In this case the mobility depends on the nature of the interactions with the atoms or molecules of the gas and enables the measurement of the collisional cross-section of the particle.

If considering compact spherical particles, the cross-section can be directly related to the size of the particles and hence measurement of mobility could be employed to obtain the mass distribution of the particles. However considering more complex particles characterized by a fractal structure, this relation is not well defined and the mobility gives only the indication of an “effective size” of the particle, which should be coupled to another independent measurement to give information about the real mass and the fractal dimension.

The next two sections introduce, in the first one of the most widely diffused techniques that employs mobility analysis to characterize nanoparticles, that is electrical mobility analysis, in the second an innovative approach for gas-phase characterization of fractal particles by mobility measurements, employing the properties of a supersonic expansion.

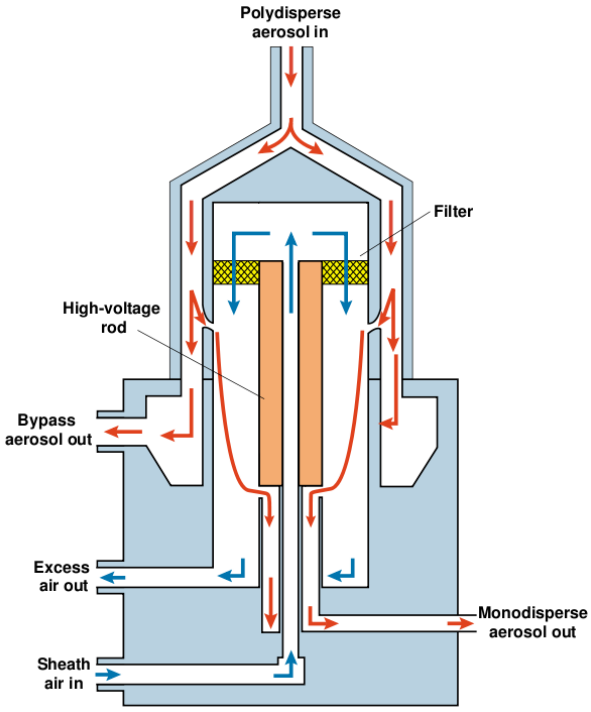

Figure 1.1: Scheme of differential mobility analyzer (DMA) (from TSI corporation)

Electrical Mobility Analysis

The principle beyond electrical mobility analysis (EMA) is that in a gas flow charged particles with different mobility and subject to the same external field, acquire different velocities and so follow different trajectories; this effect is used for particle separation and selection.

A typical design of an apparatus for EMA is reported in figure 1.1. An aerosol of the particles of interest, in conditions of laminar flow, is first passed through a charger (typically a diffusion charger to softly ionize particles, obtaining mainly singly charged particles and avoiding fragmentation), then introduced into a separation column and in the end the selected fraction of particles in counted.

The selection column is usually made by a cylindrical capacitor, in which the aerosol is injected axially between the plates. A high voltage is applied to form a radial field. The particles are then subject to two forces, the drag of the flow that is almost only axial and the drift imposed by the electric field that is mostly radial. The composition of the two perpendicular components of the velocity makes the

particles follow different trajectories depending on their mobility. At a specified position an outlet is placed, so that particles with a specific mobility can be extracted from the apparatus. By varying the electric field it is possible to select particles with different mobility.

Many different version of this apparatus are found in literature, but the concept beyond them is always the same. The difference deals mostly with the dimensions of the particle that could be detected, with resolution and with the efficiency of the measurement.

Supersonic Beam Mobility Analysis

The properties of a molecular beam obtained by supersonic expansion, can be exploited to characterize the morphology of nanoparticles in the gas-phase by modeling their acceleration in the beam through collisions with the carrier gas and by concurrent measurement of their terminal velocity and mass. This technique allows to estimate the fractal dimension of the aggregates under study.

The properties of a supersonic beam are mainly determined by the size and shape of the nozzle and by the thermodynamic properties of the gas upstream of the nozzle and simple models can provide appropriate semi-quantitative predictions [43]. Ideal thermodynamic analysis based on the first law can be employed to determine stream velocity, temperature, pressure and density along the jet axis versus distance from the nozzle. In particular, the maximum terminal velocity v_{gas} of the molecules (mass m_{gas}) is given by

$$v_{gas} = \sqrt{\frac{2k_B\gamma \cdot T_s}{m_{gas}(\gamma - 1)}} \tag{1.2}$$

where γ is the heat capacity ratio, T_s the stagnation temperature before the expansion and k_B the Boltzmann constant. The presence in the beam of heavy species - such as nanoparticles - generally introduces severe complications in the analysis; the problem can be treated when the species are diluted at very low relative concentration in a carrier gas. In this case the thermodynamic properties of the expansion can be assumed to be not affected by the presence of the seeding particles [12] that are accelerated up to a size-dependent terminal velocity by the collisions with the carrier gas [34]. The effect on cluster velocity of the finite num-

ber of collisions occurring before transition to collision-less free molecular regime is usually called "velocity slip" and can be effectively modeled through a dynamic shape factor in the free molecular Epstein regime [13], i.e. taking into account the size dependence of cluster inertia and collisional cross-section, determining the collision rate with carrier gas molecules. An expression for this model was formulated by Wrenger and Meiwes-Broer [54] under the limiting assumptions of central and elastic collisions between clusters considered as hard spheres. A more general expression will be derived from the single postulate momentum conservation.

It is convenient to describe collisions in a reference frame moving with velocity v_{gas} equal to the average carrier gas velocity and where the carrier gas is thus essentially at rest. In this frame the velocity $\tilde{v}$ of a particle with mass m is changed by one central elastic collision with the carrier gas (mass m_{gas}) to

$$\tilde{v}' = \tilde{v} \cdot \left(\frac{m - m_{gas}}{m + m_{gas}} \right) \tag{1.3}$$

This directly yields the expression (1.4) for the particle velocity in the laboratory reference frame after k collisions, as provided by Wrenger and Meiwes-Broer,

$$v_k(m) = v_{gas} \cdot \left[1 - \left(\frac{m - m_{gas}}{m + m_{gas}} \right)^k \right] \tag{1.4}$$

For any kind of collision, in the reference frame traveling with the gas, we can write the conservation of momentum along the direction of carrier gas motion as

$$m\tilde{v} = m_{gas}\tilde{v}'_{gas} + m\tilde{v}' \tag{1.5}$$

As the aim is the evaluation of the average effect of multiple collisions, it's possible to only take into account the effect of collisions on the momentum projection along the motion direction of the carrier gas; as a matter of fact, under axial symmetry conditions, the mean momentum transfer along directions perpendicular to the axis is zero. So in general

$$\tilde{v}'_{gas} = 2\alpha\tilde{v} \qquad \text{with } \alpha_{min} \leq \alpha < 1 \tag{1.6}$$

where α accounts for the actual momentum transfer occurred in the collision. The limit of maximum momentum transfer, corresponding to the case of a centered

elastic collision with $m \gg m_{gas}$, is indeed accounted for by $2\tilde{v}$ while α_{min}, which is zero in the case of hard-sphere collisions, can assume in the most general case also negative values, taking for example into account the possible gas adsorption and desorption processes with diffused emission over the whole solid angle [13]. Under this parametrization momentum conservation means

$$\tilde{v}' = \tilde{v}\frac{m - 2\alpha m_{gas}}{m} \tag{1.7}$$

which can be rewritten as

$$\tilde{v}' = \tilde{v} \cdot \left(\frac{m - m_{gas}}{m + m_{gas}}\right)^{\log\left(\frac{m-2\alpha m_{gas}}{m}\right)/\log\left(\frac{m-m_{gas}}{m+m_{gas}}\right)} \simeq \tilde{v}\left(\frac{m - m_{gas}}{m + m_{gas}}\right)^{\alpha} \tag{1.8}$$

where the approximation holds if $m \gg m_{gas}$.

In the laboratory frame, after k collisions the average particle velocity is thus

$$\langle v_k(m)\rangle \simeq v_{gas} \cdot \left[1 - \left(\frac{m - m_{gas}}{m + m_{gas}}\right)^{\langle\alpha\rangle\, k}\right] \tag{1.9}$$

The general expression of the particle velocity evolution after collision with the carrier gas molecules is thus the same as for the simple central elastic collision model with the total number of collisions scaled by an effectiveness parameter $\langle\alpha\rangle$ with $0 < \langle\alpha\rangle < 1$. The actual value of $\langle\alpha\rangle$ depends on the nature of gas-particle interaction [30] and can in general be affected by particle morphology [33], taking into account the balance of diffused versus elastic scattering [13].

For given expansion conditions, the number of collisions can be assumed to scale with the geometric cross section σ of the particle (the projection of the particle geometry onto a plane perpendicular to the direction of carrier gas motion) [33], so that the velocity of clusters of mass m, which undergo $k\langle\alpha\rangle = \beta \cdot \sigma$ effective collisions in the forward direction along the jet expansion, can be modeled by

$$v(m;\sigma) = v_{gas} \cdot \left[1 - \left(\frac{m - m_{gas}}{m + m_{gas}}\right)^{\beta\,\sigma}\right] \tag{1.10}$$

This expression puts in explicit form the fact that clusters seeded in a supersonic expansion are accelerated along the jet axis by the collisions with the expanding

gas molecules. The number of forward "kicks" is determined by the particle collisional cross-section and the effect of each is related to the particle mass and to an additional scaling parameter characteristic of the scattering process. Therefore, an accurate measurement of the velocity-to-mass relation characterizing a set of clusters can bring information on the morphology on the scale of the collisional cross-section of the carrier gas molecules. The explicit form for cluster morphology description enters into the model through the scaling law between σ and m.

By defining the fractal dimension characterizing a set of aggregates as the exponent describing the scaling of objects' size S against a characteristic linear dimension $R(S \propto R^D)$, a relation can be obtained between the fractal dimension D for clusters volume in 3D and fractal dimension D^* for the corresponding projected area in 2D. In the case of infinite self similar objects, this relation is simply $D^* = \min(2, D)$ [33], while the case of real fractal-like objects has been discussed in detail by Nelson et al. [36] who derived the general expression relating D and D^* in dependence on an observation scale parameter X (defined in reduced units relative to object linear dimension) that accounts for the finite resolution of the observation method, or for the lower boundary to the scale of the fractal-like physical object imposed by finite primary particle size of the aggregates.

For a physical fractal-like object consisting of an aggregate formed by a number of homogeneous primary particles we have $m \propto R^D$ and $\sigma \propto R^{D^*}$ because of the cross section for the gas-particle collision being proportional to the aggregate's projection area. We can thus write

$$\sigma \propto m^{D^*/D} = m^{\xi} \tag{1.11}$$

where ξ is defined as D^*/D. A given $\xi \leq 1$ generally corresponds to two possible distinct solutions for the fractal dimension D, one in the range $2 \leq D \leq 3$ given by $D = 2/\xi$ and the other one in the range $1 \leq D < 2$ that can be determined using the expression given by Nelson et al. [36] if an estimate for the observation scale is available. In the process of probing cluster geometry through atomic collisions, the observation scale is in the order of the collision diameter of the carrier gas ($\sim 0.27nm$ in the case of He_{28}). The assignment of a fractal character to clusters and nanoparticles is also generally limited by an inner scale imposed by the size of the primary particles forming the aggregate (which can be larger than the atomic

scale in the presence of hierarchical aggregation of compact primary particles into fractal-like super-aggregates). According to Nelson et al. this finite component size does not affect the apparent dimension D^* as long as it is considerably smaller than the aggregate size [36].

The proposed method for the characterization of the σ to m scaling behavior provides access to a quantitative determination of the fractal dimension of the aggregates, restricting indecision to two distinct solutions which generally correspond to distinct physical situations very far from each other that can therefore be sorted out on the basis of very limited previous knowledge of the system under study. The most peculiar aspect of this method is that it provides a fractal dimension parameter associated to a cluster population, and not to a single object. Sampling from a set of many particles of different sizes is individuated indeed as a most effective route for mapping the system under study at different length-scales using a single probe with fixed scale – the colliding atoms.

1.2.2 Near edge X-ray absorption fine structure spectroscopy

X-ray absorption spectra are characterized by absorption steps, called edges, that happen when the photon energy becomes equal to the binding energy of a core state; core levels of each element have specific binding energies and so the identification of these absorption edges makes possible the determination of the chemical composition of the sample. Moreover just before these edges many fine spectral features are present. These features are the target of Near edge X-ray Absorption Fine Structure (NEXAFS) spectroscopy (for a review see [47, 9]).

The pre-edge absorption peaks appear when the photon energy becomes resonant to a transition from a core-level to a still bounded excited state. The study of these features can give information on the local environment of the probed atom and on the structure of unoccupied molecular orbitals.

1.2.3 Photo-electron spectroscopy

Photo-electron spectroscopy studies the composition of a sample by exposing it to X-rays of known and fixed energy and by measuring the kinetic energy of the emitted electrons. The difference in energy between the photon and the electron is

the binding energy of ionized core-level.

As in XAS, core-levels are sensitive to the local environment of the probed atom, and so the line-shape of the emitted electrons carry information about chemical bonding and coordination, permitting for example in clusters to distinguish between surface and bulk atoms.

1.2.4 Photo-fragmentation in intense photon beams

Photo-fragmentation, or photo-dissociation when dealing with molecules, is a powerful technique to investigate the structural properties of matter. In fact, from the way a system fragments, valuable information can be inferred about its structure and the bonds that hold it together.

The comprehension of the fragmentation process happens in two steps: the first is the process with which excess energy is deposited into the system, and the second one is the way the system follow to relax this excess energies.

In the following are reported the general means of absorption of finite systems exposed to intense laser beams and the mechanism with which this system can fragment, with a major focus on metallic clusters.

Energy absorption mechanisms

In general ionization mechanisms can be divided into two main categories: photon-dominated and field-dominated. In the first case electron emission (or excitation) is mainly due to the absorption of one or multiple photons, while in the other, the process is dominated by the very intense electric field that strongly modifies the energy levels of the system under consideration, promoting processes such as electron tunneling (the two processes are schematically depicted for an atomic potential in figure 1.2a).

The prevalence of one of the process over the other can be conveniently described by the Keldysh adiabaticity parameter [23]

$$\gamma = \sqrt{\frac{E_{IP}}{2U_p}} \tag{1.12}$$

where E_{IP} is the ionization potential while U_p is the ponderomotive potential, that is the quiver energy of the electron oscillating in the laser field, expressed by

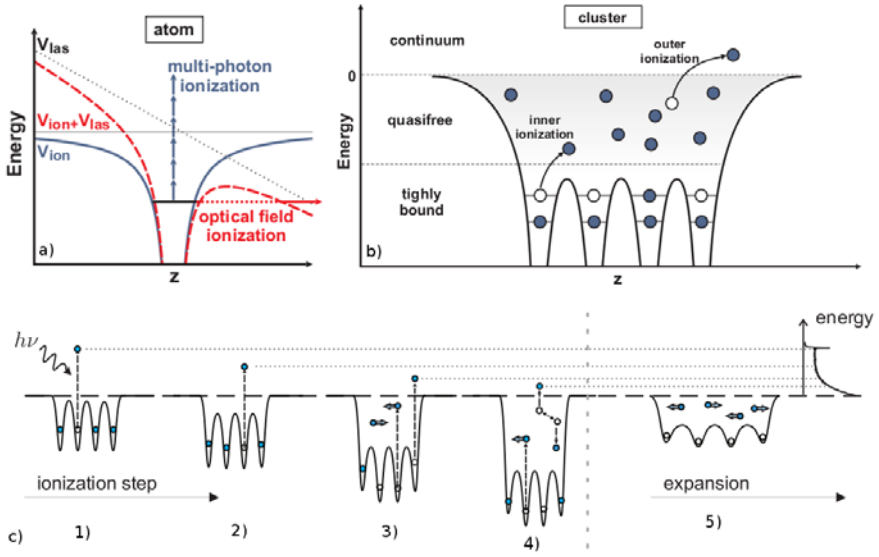

Figure 1.2: Schematic view of ionization mechanisms in atoms, molecules and clusters. (Reproduced from [14])

$$U_p = \frac{e^2 \left|\mathscr{E}_0\right|^2}{4 m_e \omega_{las}^2} \tag{1.13}$$

where $\mathscr{E}_0$ is the electric field amplitude, ω_{las} the laser frequency and e and m_e the charge and mass of the electron.

On the atomic level mainly two processes are possible, which are easily distinguishable form the γ parameter and are schematically depicted in figure 1.2a. When $\gamma \gg 1$, the quiver energy of the electron in the optical field is small and the predominant ionization process is multi-photon ionization (MPI). Otherwise when $\gamma \lesssim 1$ the dominating ionization mechanism is optical field ionization (OFI): in this case the laser field can be seen as a quasi-stationary electric field that, if sufficiently strong, can permit electrons to tunnel through the potential barrier into the continuum.

In a cluster the situation is of course more complex because also the electronic structure of the cluster itself plays a role in the determination of the prevailing ionization process. A very convenient way for the description of the charging dynamics of a complex system is the distinction between inner and outer ionization, as introduced by Last and Jortner [28]. As schematized in figure 1.2b, electrons in a cluster can be divided into free, quasi-free and tightly bound electrons. Therefore

inner ionization refers to the excitation of a tightly bound electron to a conduction band, while outer ionization refers to the final excitation of the electron to the continuum.

If we consider infrared and visible wavelengths, typical of table-top lasers, we can schematize the ionization dynamic as initiated at first by OFI that promotes inner ionization of the clusters and buildup of a transient nano-plasma; the efficient coupling of the plasma to the laser radiation leads to an extremely strong energy absorption, mainly driven by inverse bremsstrahlung (IBS) [14].

Moving to wavelengths in the VUV range, the inner ionization dynamics is initiated by multi-photon ionization, leading also in this case to the formation of a nanoplasma, which is then heated mainly by IBS and the outer ionization process is dominated by evaporation of thermal electrons. The explosion of the cluster is dominated by hydrodynamic forces inside the plasma [1, 2].

If we further increase the photon energy in the XUV range, sequential direct ionization is the dominating process of cluster ionization until frustration occurs because of the increasing coulomb potential. Cluster heating proceeds by inner ionization, then a charge redistribution mechanism leads to the stabilization of the cluster by the coulomb explosion of the outer shells of the cluster, while the core plasma undergo recombination and hydrodynamic expansion [2, 19].

Finally considering soft x-rays, the energy absorption mechanism is multi-step ionization and the cluster expansion dynamics moves towards a pure coulomb explosion [2].

Fragmentation mechanisms

Fragmentation channels of large multi-charged clusters are found to depend on many factors, like the charge distribution and the range of the interaction between constituents atoms.

The fragmentation processes can be classified into two categories: fission-like processes and Coulomb explosion processes. In the liquid drop model (LDM), generally employed to describe metal clusters, the distinction between the two regimes is generally expressed by the fissibility parameter χ, that is

$$\chi = \frac{E_{\text{coulomb}}}{2E_{\text{surface}}} \tag{1.14}$$

where E_{coulomb} expresses the repulsive forces while E_{surface} expresses the cohesive forces.

Generally for a fissibility factor $\chi < 1$, that for low charge state indicate long range interaction in the cluster (like covalent bonding), fission of the cluster into few large fragments is preferred, while for a fission parameter $\chi > 1$, that is indicative of short range interactions (like Van der Waals bonding), Coulomb explosion in more probable [29].

A recent work showed that also charge redistribution in the cluster is important in deciding the fragmentation process; by molecular dynamic calculations it is found that a surface distribution of charge favors coulomb explosion while a more uniform distribution favors instead fission of the clusters [8].

Chapter 2

Supersonic Beam Apparatus for gas-phase cluster characterization

Seeded molecular beams are a very powerful technique for the characterization of molecular species and atomic clusters in the gas-phase. The Molecular Beam Laboratory (LGM) of the Department of Physics of the Università degli Studi di Milano has a long standing experience in the production and manipulation of seeded supersonic clusters beams; in particular it developed a novel type of pulsed cluster source, the Pulsed Micro-plasma Cluster Source (PMCS), which is the source used in the experiments described in this thesis. The source, which is described in detail in the next section, is a pulsed vaporization Inert Gas Condensation (IGC) type of source, based on a aerodynamically confined plasma sputtering. Aerodynamic focusing techniques derived from the aerosol science are employed before the supersonic expansion in vacuum to achieve a high intensity cluster beam, suitable for gas-phase spectroscopic characterization; moreover the pulsed operation of the source gives access, within each pulse, to different populations of clusters that have experienced different residence times in the source and so had different thermal history.

As discussed before, core level spectroscopy techniques employing synchrotron

radiation (SR) are very powerful tools to investigate the properties of nano-scale objects. The following sections describe how the PMCS source was coupled to SR-based characterization apparatuses to perform measurements of free clusters with X-Ray Absorption Spectroscopy (XAS), X-Ray Photo-electron Spectroscopy (XPS) and photo-fragmentation.

The first section describes the PMCS source and the experimental setup developed for XAS, that was coupled to the Gas-Phase beamline [4] of the Elettra synchrotron radiation laboratory (Trieste, Italy) in order to perform NEXAFS experiments on free carbon clusters (see chapter 3).

In the second section a detailed description of the apparatus developed for time-resolved X-Ray Photo-electron Spectroscopy (XPS) on free clusters is then given; the apparatus was coupled to the I411 beamline [7] of the Max Lab synchrotron radiation facility (Lund, Sweden) to perform experiments on free lead clusters (see chapter 6).

Finally the last section describes in detail the apparatus developed to preform photo-fragmentation experiments on titanium clusters, employing the high intensity pulses produced by the SCSS EUV FEL [45] at the Spring8 synchrotron radiation laboratory in Japan (see chapter 5).

2.1 Setup for time-resolved XAS of free clusters

Journal of Electron Spectroscopy and Related Phenomena 166–167 (2008) 28–37

Contents lists available at ScienceDirect

Journal of Electron Spectroscopy and Related Phenomena

journal homepage: www.elsevier.com/locate/elspec

CESyRa: A versatile setup for core-level absorption experiments on free metallic clusters using synchrotron radiation

P. Piseri[a,*], T. Mazza[a], G. Bongiorno[a], M. Devetta[a], M. Coreno[b], P. Milani[a]

[a] Dipartimento di Fisica and CIMAINA, Università degli Studi di Milano, Via Celoria 16, I-20133 Milano, Italy
[b] CNR-IMIP, Area della Ricerca di Roma I, Via Salaria Km 29.3, I-00016 Roma, Italy

ARTICLE INFO

Article history:
Available online 18 May 2008

Keywords:
X-ray absorption spectroscopy
Photo-ionization
Transition metal clusters
Cluster beams
Aerodynamic lenses

ABSTRACT

The possibility to apply synchrotron radiation-based spectroscopic techniques, and in particular X-ray absorption spectroscopy (XAS), to isolated nanoparticles is expected to bring important insight into the electronic properties, the structural arrangement, and the chemical character of finite size systems. A precise knowledge of such properties has special relevance for a bottom-up approach to the description of nanostructured systems of technological interest. Element specificity, chemical sensitivity and local character are most significant qualities demanded from the characterization tools in this regards. The extremely low density of free particles samples is the main issue limiting the development of such techniques and only very recently first experimental results on systems of strong technological relevance like transition metal nanoparticles.

In this paper we describe an experimental setup for core-level absorption investigations on free metal clusters. The most critical issues for experiment feasibility are discussed and the adopted methodology is described in detail. Results from the application of this approach to core-shell photo-ionization studies on free Ti clusters are presented as a case study.

1. Introduction

The tuning of the electronic, optical and magnetic properties of nanoparticles by controlling their dimensions [1–3], as the first step towards the building of complex systems of many interacting nano-objects, is one of the most fascinating challenges of nanotechnology. Although this bottom-up approach is currently subject of an enormous attention in view of a wide range of applications, the investigation and the understanding of the fundamental properties of individual nano-systems free from perturbations is still in its infancy. Clusters are highly reactive and the interaction with solid or liquid matrices affects their properties [4,5]; moreover deposited clusters may suffer from fragmentation upon landing, or aggregation, coalescence, chemical contamination, or structure distortions, and from a large uncertainty in size determination [4,6].

Isolated clusters, i.e. aggregates consisting of up to tens of thousands of atoms, can be produced in the gas phase and, in particular, in molecular beams where their mass and thermodynamic state can be precisely defined [7,8]. The molecular beam approach allows real-time particle observation in at well defined time after formation or after induced transformations; it thus provides access to the mechanism of cluster growth, to the investigation of reactive and metastable species, to the fine-tuning of complex systems (e.g. particle-adsorbate systems) [9,10]. The characterization of clusters in the gas phase is nevertheless very difficult since the high degree of dilution makes the use of conventional spectroscopic techniques, and especially those based on electron or photon scattering and absorption, a formidable challenge [7]. The existing strong experimental difficulties and technical limitations cause the presence of a wide gap between applications of nanostructured materials and their fundamental understanding.

Recently different groups have demonstrated that the local electronic structure, electronic density of states, and correlation effects in isolated metal clusters produced in the gas phase can be studied by core-level spectroscopy [11,12] and, in particular, by X-ray absorption spectroscopy (XAS) using synchrotron radiation. This achievement has been possible by the coupling of high-brilliance, synchrotron radiation beamlines with high-intensity cluster sources.

Here we present and describe an experimental setup for the investigation of free metallic clusters by synchrotron radiation photo-ionization; the cluster experiment with synchrotron radiation (CESyRa) experimental design is based on the concept of coupling an apparatus for the production of intense supersonic metal cluster beams with a high flux third generation light source synchrotron beamline. The experimental work presented here was

* Corresponding author. Tel.: +39 02 503 17357; fax: +39 02 503 17482.
E-mail address: paolo.piseri@fisica.unimi.it (P. Piseri).

0368-2048/$ – see front matter © 2008 Elsevier B.V. All rights reserved.
doi:10.1016/j.elspec.2008.05.003

performed at the Gas Phase photoemission beam line at the Elettra synchrotron radiation facility, Trieste, Italy [13,14].

The paper is organized as follows: the experimental section gives an overview of the apparatus, with special focus on the concepts driving its design and on the enabling character of the implemented techniques. A separate section is dedicated to the possible data analysis approaches offered by the setup and to the discussion of their relevance within the characteristics and possibilities opened by the adopted nanoparticle synthesis route. The results section is included as an exemplification of the described techniques ad as an introduction to the results obtained applying the presented methodology to the study of free Ti clusters.

2. Experimental setup

2.1. Supersonic beam apparatus

The supersonic cluster beam apparatus is schematically outlined in Fig. 1: it consists of five differentially pumped vacuum chambers providing the required ultra high vacuum (UHV) conditions at the photon-cluster interaction point despite the high gas load typical of supersonic cluster source operation.

The first chamber is the expansion chamber of the molecular beam, it is evacuated by a 2000 l/s turbomolecular pump backed by a dry pumping stage boosted by a 120 l/min roots pump; the chamber is equipped with two sets of two-axis linear motion feed throughs allowing cluster beam alignment. The two sets act respectively on the molecular beam nozzle (for free-jet steering) and on the skimmer support (for nozzle-skimmer relative alignment). An electro-formed 2 mm diameter skimmer at 40 mm distance from the nozzle provides the selection of the central part of the free jet in order to guarantee stable high vacuum conditions in the following chamber, thus producing a suitably low background pressure for the molecular beam. The cluster source, whose design allows installation outside the vacuum vessel (see next section), is connected to the expansion chamber through an ISO100 port and evacuated through the source nozzle. A built-in system for differential pumping of the source body provides the preservation of high vacuum base-pressure conditions inside the cluster source.

The second chamber hosts a small cell, aligned with the molecular beam axis and connected to a mass flow control gas inlet. The cluster beam travels across the cell and possibly interacts with gas species at controlled pressure. Plates for electrostatic deflection of ionized species produced by the cluster source are also installed in the chamber in order to wipe them off the cluster beam. A narrow capillary aligned with the gas cell connects the second chamber to the next one, producing a two orders of magnitude pressure drop and ensuring the conditions for the operation of channel electron multipliers installed in the third differential vacuum chamber as beam diagnostics tools. The two detectors work in a pulse counting mode and can measure the cationic and anionic ion flux produced by the source. When performing this measurement the deflecting plates in the gas cell are grounded.

In the fourth chamber, photons from the synchrotron beam-line cross the cluster beam within the acceleration region of a single stage time of flight mass spectrometer (TOF/MS), oriented per-

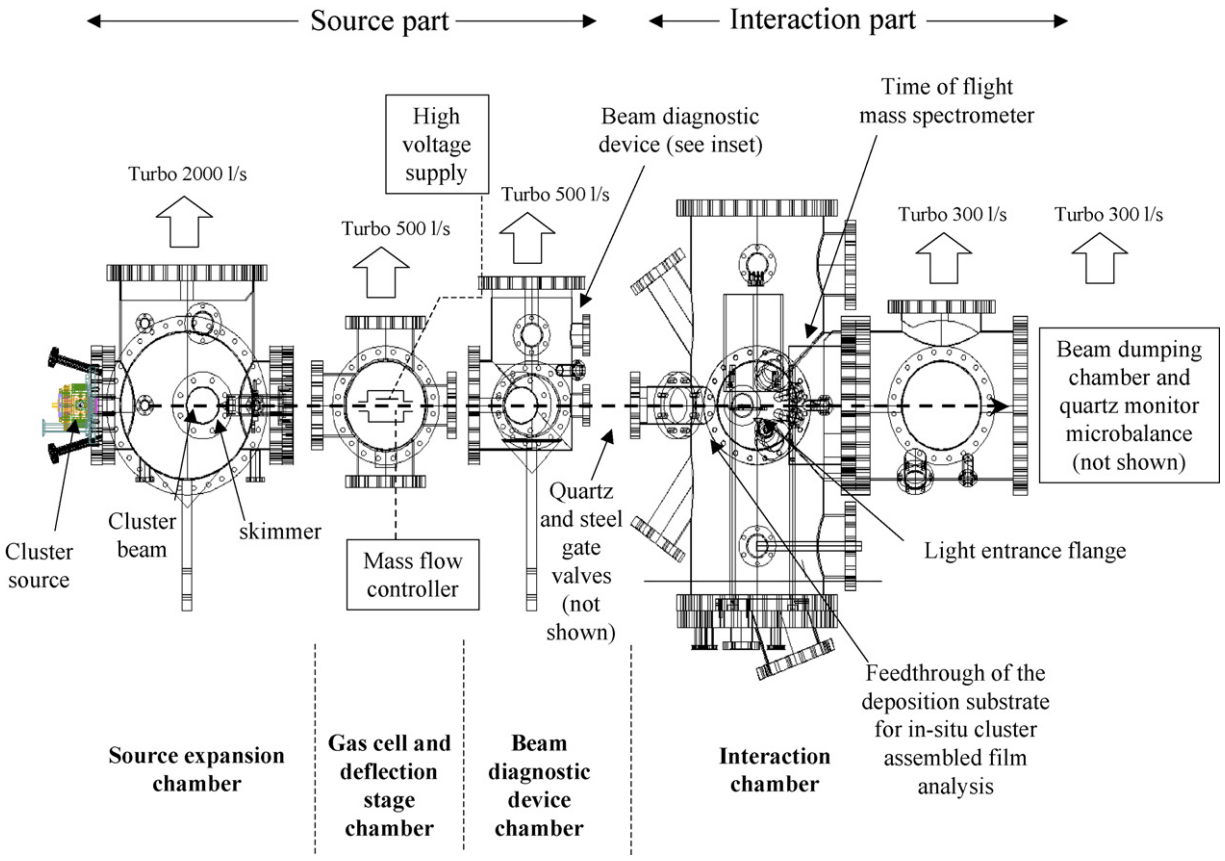

Fig. 1. Schematic representation of the experimental apparatus. From the left to the right, the sketch represents the cluster source faced on the expansion chamber, the gas cell chamber, the beam-diagnostic chamber, the interaction chamber and the beam-dumping chamber (see text). A gate valve separates the cluster beam generation section (first three chambers) from the interaction part where, at 1.5 m from their origin, the clusters cross the photon beam inside in the acceleration stage of a time of flight mass spectrometer. The cluster flux is measured by a quartz-crystal microbalance head on which clusters impact. The intensity of the photon beam from the synchrotron beam-line is monitored by a silicon photodiode.

pendicularly to the cluster and photon beams. The photon beam intensity is monitored by a photodiode intersecting the beam after the interaction region. The chamber is separated from the previous one by a transparent gate valve to allow optical alignment of the apparatus while preserving UHV conditions in the interaction region. The base pressure during the experiments is typically of 5×10^{-9} mbar. A copper bar, electrically insulated from the apparatus and held by a three-axis movement stage, lies on the plane of the beams and can be placed at the interaction point, simultaneously facing both the cluster and photon beams with an inclination of 45°. The drain current, produced by X-ray photoemission from the surface of cluster-assembled films deposited on the bar, can be measured to get in situ X-ray absorption spectra of deposited clusters. The measurement can be performed during deposition. The temperature of the bar can be varied in the range of 100–450 K by means of electric heating and liquid nitrogen flow. A comparison has been recently performed between XAS spectra from deposited and free Ti clusters using this setup [10].

After the interaction chamber, the cluster beam enters a last chamber for beam dumping; here the particles impact and get deposited on an oscillating quartz crystal microbalance providing a real time direct measurement of the overall cluster beam mass flux from the source. The dumping of the beam in a separate chamber ensures an optimum suppression of background signal produced by metastable helium coming from the cluster source.

The apparatus described above has a 1.20 m × 3.50 m footprint and all the instrumentation needed for source operation and data acquisition finds place in two 19 in. racks. The whole experimental equipment can be transported in a medium size van, assuring the versatile character of the apparatus, that can be interfaced to light sources with suitable photon beam characteristics.

2.2. Cluster source

A fundamental requisite for the feasibility of core-shell absorption experiments on free clusters is the availability of a suitable cluster density; this is obtained, in our setup, by using a pulsed microplasma cluster source (PMCS) [15,16], combined with an aerodynamic lens system [17,18] (Fig. 2). The PMCS consists of an insulating body made of Shapal-M® machinable ceramics in which a small cavity hosts a rod of the material from which clusters are formed. A pulsed solenoid valve (Parker Series 9) periodically injects gas from a high-pressure reservoir into the cavity, forming a strong jet directed against the target rod: a small region characterized by high density of the gas is formed at the cathode surface thus creating the conditions for electric breakdown in this specific position inside the cavity. A high voltage pulse (with negative polarity in the range 500–1500 V) from a high current power supply (typically limited by a 1 Ω series resistor) is applied for a few tens of microseconds to the target rod, producing a very intense discharge that vaporizes the rod (the cathode) through ion bombardment. The current loop is closed by the presence, inside the cavity but out of sight from the ablation region, of an anode held at ground potential. To maintain constant operation conditions for the source over long periods of time, the cathode rod is continuously rotated by means of an external motor and a homogeneous consumption of the rod along its lateral surface is produced. Few days of continuous operation without maintenance are typically obtained at conditions used for the experiments presented here.

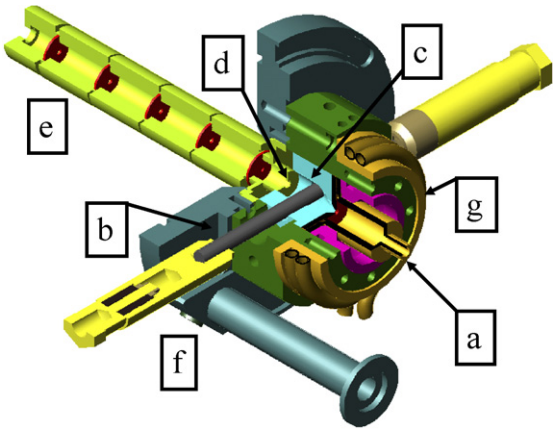

Fig. 2. Detail of the PMCS (sectioned). (a) Pulsed solenoid valve for gas injection; (b) rotating cathode; (c) cluster condensation cavity drilled in the ceramic body of the source; (d) gas discharge outlet; (e) aerodynamic lens system; (f) ISO100 flange with built in differential vacuum system; (g) water-cooling system.

The strong confinement of target ablation in a high-pressure region yields an extremely rapid quenching of the ablated species favouring a very effective cluster nucleation close to the cathode surface. The strong pressure gradient produced at gas injection confines the ablation region out of the source cavity walls thus avoiding contamination of the clusters by chemical species ablated from the source body. Under typical operating conditions, the main source of cluster contamination is the carrier gas injected in the source; high purity bottles with <1 ppm impurity concentration are used. The chemical composition of clusters can be eventually modified by mixing reactive gases with inert process gas at controlled partial pressures [10]. To meet the severe conditions imposed by the synthesis of highly reactive species like Ti nanoparticles, a MicroTorr® sorption cartridge (Saes-Getters) was used during the experiment providing He with less than 1 ppb impurities to the gas loader.

The most critical parameter for pulse-to-pulse reproducibility of cluster nucleation conditions is the stability of gas injection and, in particular, the repeatability of the gas pulse rise-time on a time scale of ~10 μs. To meet this requirement, a careful control of pulsed valve temperature is needed, as thermal drift, even in a moderate temperature range, produces significant changes in the response of fast solenoid valves. Temperature control in the PMCS is achieved by a careful selection of high thermal transport materials and a suitably robust heat exchange water-cooling system (Fig. 2).

After formation, clusters are extracted from the PMCS by the drifting action of the injected gas, acting as a carrier for the suspended particles; this process occurs on a much longer time-scale than the nucleation step, and residence time of the gas–cluster mixture in the source cavity extends to several milliseconds after target vaporization. The PMCS can be considered as a time modulated inert gas condensation (IGC) [19,20] particle source where clusters undergo a number of processes like: further growth steps; diffusion to the walls of source cavity; inertial separation effects in the gas flow. All these steps have a strong influence on the structure and the density of particles available for investigation. These aspects, though deeply characterized in the case of aerosol sources and applications, have only marginally been considered in the study of clusters in supersonic beams [21].

2.3. Aerodynamic focusing

The source nozzle used for this work is an aerodynamic lens system concentrating the clusters in the central part of the free jet originating the supersonic beam. The focusing assembly consists of a series of thin plates mounted in a cylindrical barrel [17,22]. Each plate (aerodynamic lens) has a central orifice, and the assembly terminates in an exit nozzle where the sonic plane of the final supersonic expansion is located. By passing through the lens system, the aerosol flow undergoes a series of contractions and then re-expansions where inertial separation occurs. Small enough par-

ticles closely follow the gas streamlines; exceedingly large particles, after radial acceleration towards the axis on the converging-flow side of the lens, are projected across the centreline and then, too loosely coupled to the gas flow, impact on the sidewall. Particles with intermediate size are brought closer to the centreline after each lens owing to the fact that drag is more effective on the converging-flow side of each lens than on the diverging one. The parameter of choice to describe inertial separation of particles in a flow-field is Stokes number (St), which represents the ratio between drag and inertial forces acting on the particle, as observed in a reference frame moving with the flow; optimal focusing conditions are produced by aerodynamic lenses for St ∼ 1.

In PMCS, at each gas pulse injection, the pressure inside the source rapidly rises up to roughly 100 mbar (within typically less than 1 ms). After this stage, where also vaporization and nucleation take place, the gaseous content of the source cavity is discharged through the nozzle with a characteristic time of the discharge in the range of few tens of milliseconds. During this time, the density and temperature of the carrier gas strongly evolve, exploring a wide range of Stokes numbers, for each particle size in the population of the produced clusters. As this "automatic" scan of the aerodynamic focusing system is performed simultaneously with particle growth inside the source, the combination of two main parameters: pressure at electric discharge time (actually controlled through electric discharge delay after start of gas injection), and total amount of gas injected (through valve opening time duration), can be used to obtain optimum source intensity for chosen size and thermal history of the produced particles. As an example, Fig. 3 displays the pulse profile corresponding to three different working parameters of the PMCS for the production of metallic Ti clusters (parameters are listed in Table 1). The corresponding time of flight spectra from a selected part of the cluster beam pulse are also shown in Fig. 3.

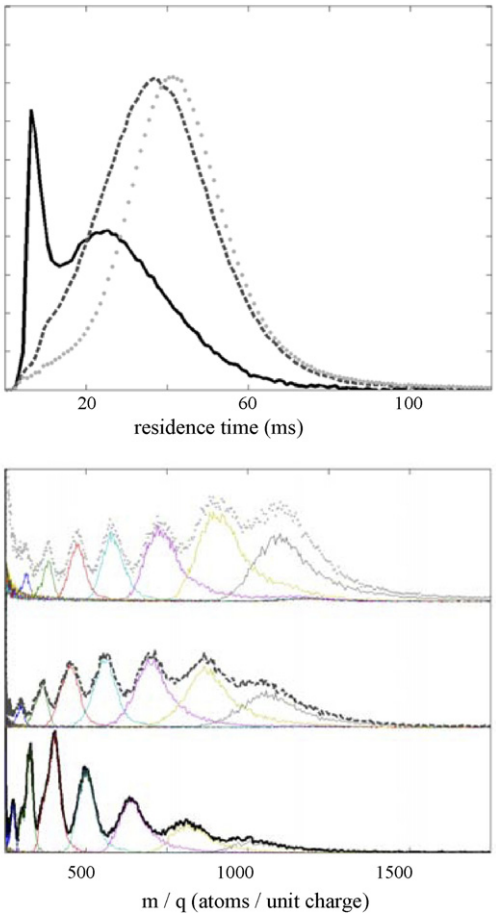

Fig. 3. Upper panel: cluster beam intensity profile as obtained from electron yield, for the three different sets of PMCS working conditions listed in Table 1 (black full line: setup #1; dark grey broken line: setup #2; light grey dotted line: setup #3). Lower panel: the corresponding mass spectra (setup #1 to setup #3 for spectra from bottom to top. Line styles are the same as used for upper panel). Spectra are relative to the residence time window between 20 and 30 ms. The modulation that can be observed in the spectra is due to un-homogeneous detection efficiency over the accessible mass range; this is an intrinsic limitation of the adopted ion detection scheme, which is described in the text.

2.4. Pick-up cell

In the second chamber the beam passes through a 10 cm × 5 cm × 5 cm cell in which molecular species can be dosed. The cell is connected to a mass flow control device by means of a 1/8 in. steel tube and is traversed by the cluster beam entering and exiting on opposite sides along longer dimension through two aligned 4 mm ∅, 20 mm long capillaries. A secondary housing, with aligned inlet and outlet thin plate orifices, directs part of the effusing gas exiting the cell to the turbo-pump throat, thus improving differential vacuum between the gas cell and the hosting vessel. The partial pressure inside the cell can be set up to a maximum of 5×10^{-2} Torr, resulting in a 0–10 Langmuir exposure range, with typical transit time for the flying nanoparticles in the range of about 100–200 μs, depending on their velocity that varies along each cluster pulse (see below).

The effect of cluster exposure to molecular hydrogen and water on the electronic structure have been analysed by total electron yield NEXAFS spectroscopy on Ti and TiO_x clusters [10]. In the present work the influence of molecular hydrogen exposure on metallic clusters is discussed within the frame of the conceptual tools for data acquisition and handling developed and presented in the following section.

2.5. Time of flight mass spectrometer

Time of flight (TOF) technique is probably the only viable choice to study core-shell photo-ionization of free clusters by ion yield, since the low density of the sample makes the achievement of the highest collection efficiency mandatory. Seeded supersonic molecular beams of clusters exhibit high kinetic energy for cluster motion along the beam axis (∼0.8 eV/atom in the case of Ti seeded in He at room temperature); this introduces severe constraints to the TOF spectrometer design. Ion extraction perpendicular to the molecular beam axis significantly improves mass resolution [23], but strong electric fields are needed to steer the ions towards the detector; ion trajectory is anyway dependent on its mass

Table 1
Working parameters of the PMCS corresponding to the different pulse profiles and TOF spectra reported in Fig. 3

	Pulsed valve T_{on} (μs)	$P_{exp.\ chamber}$ (mbar)	Discharge delay (μs)	Discharge duration (μs)	Average deposition rate (nm/min)
Setup # 1	260	8.5×10^{-5}	600	40	5
Setup # 2	290	1.2×10^{-4}	620	40	10
Setup # 3	330	2.2×10^{-4}	750	60	30

The results for metallic titanium clusters presented in the following refer to working parameters from set #1.

and short instruments with large area detectors are demanded in order to obtain wide mass range sensitivity. The addition of position sensitivity to the detector can provide useful additional information on particle momentum, which provides insight into cluster thermal properties inherited from the carrier gas stagnation temperature, and into fragmentation processes occurring after photo-excitation. A robust and economical solution for this goal is the use of a channel electron multiplier array as the ion detector. A major drawback of this choice is the price paid in terms of mass resolution, as the geometrical characteristics of these detectors do not allow a precise determination of the flight length. Additional limitations of this approach are the poor spatial resolution and the presence of a strong un-homogeneity in detector sensitivity over the acceptance area. We chose this scheme for our setup and designed a compact single acceleration stage instrument optimized for detection efficiency sacrificing resolution. A single stage rather than common Wiley-Mc Laren scheme was adopted for simplicity and to access stronger electric field after recognizing in the detector geometry the principal term limiting resolution.

A schematic representation of the TOF spectrometer hosted in the interaction chamber is shown in Fig. 4. The VUV-cluster beam intersection is placed between the two grids (32 mm ∅ and 55 mm ∅, respectively for the lower and upper grid) of the 22 mm long acceleration stage (at 17.5 mm from the upper grid); a stainless steel tube (internal diameter 104 mm) screens the 187 mm long field free region. Ions and electrons from photo ionization are detected

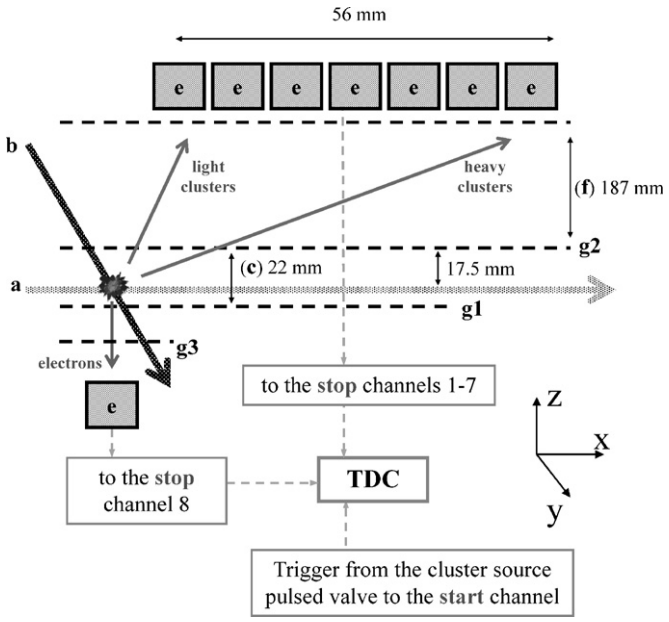

Fig. 4. Schematic representation of the time of flight mass spectrometer equipped with a position sensitive ion detection array. The clusters in the molecular beam (a) travel along the *x*-axis, and are ionised by the photon beam (b) aligned parallel to the *y*-axis and crossing the molecular beam at 90° inside a 22 mm long electrostatic acceleration stage (c). The electric field is produced between a lower grid (g1; 32 mm ∅) and an upper grid (g2; 55 mm ∅). Electrons and ionised clusters are accelerated along the z-axis and are collected by different detectors: a channel electron multiplier for the electrons (d) and an array of seven channel electron multipliers for the ions (e). Additional grid (g3) screens the electron detector for optional partial electron yield operation. For a given molecular beam velocity, each ion detector accepts a separate time-of-flight window centred at a characteristic value determined by the field free stage (f) length (187 mm) and the accelerating field potential. The signals from each detector are fed to the stop channels of the time to digital converter (TDC). The TDC start is triggered by a logic synchronizing signal from pulsed valve opening at cluster source.

by the channel electron multipliers positioned on the negative and positive side of the acceleration stage; additional grids screen the electron detector for optional partial electron yield operation mode through electron energy filtering. A linear array of seven 7 mm long and 18 mm wide channel electron multipliers, evenly spaced along the molecular beam direction (8 mm inter-centre distance), is used for ion detection, obtaining an approximately 17 mm × 42 mm sensitive area. The array is mounted on a rigid frame that can be moved along the beam direction with a 55 mm travel in order to possibly shift the mass transmission window to desired range, given the cluster beam velocity and ion extraction field. Numerical simulations [24] predict a resolution of $m/\Delta m = 80$ for this geometry assuming a 5 mm uncertainty in the flight length due to the conical shape of ion detectors sensitive area, and 5 kV as the applied bias potentials.

2.6. Data acquisition electronics

Pulsed nature of PMCS allows the investigation of clusters that experienced a wide spread of different residence times and thermal history, and thus different growth conditions. This makes very interesting to introduce the possibility to discriminate events according to the different parts of each cluster beam pulse. Logic gating of the acquisition electronics is a possible route, but lacks in terms of the high detection efficiency commitment imposed by sample diluteness. To catch the full timing information relative to each event, without reduction in counting efficiency, a large dynamic range time to digital conversion (TDC) system with multiple channels and multi-hit capability has been set up. The system is based on a TDC chip from Acam GmbH (8 channels, resolution better than 100ps, <5 ns dead time) and implemented using the ATMD-GPX PCI board test system from the same manufacturer [25]. The board is installed in a dedicated computer running on Linux OS and managed by an *ad hoc* developed server application that can be controlled via the PC's Ethernet interface in a client/server architecture. The TDC is set in a self-retriggering mode and coupled to a software counter indexing retriggering cycles; the server application stores the timing information relative to any possibly occurred stop event, making complete use of the hosting PC resources. This system allows high-resolution acquisition of a very large number of stop hits, in an indefinite time range after a single start. System testing proved its effectiveness for average counting rates up to 300 KHz, well above the regime encountered in present experiment. The signals from each channel electron multiplier (one electrons detector + seven ions detectors) are fed to the eight TDC stop channels after discrimination (Ortec® CF8000, pulse rise time 1 ns, pulse width 10 ns) [26]. The TDC start is triggered by a logic signal synchronous to the cluster source pulsed-valve opening (Figs. 4 and 5).

A second identical TDC system is synchronously triggered and used to measure complementary information with pulse-to-pulse resolution; these are namely: the ion count signals from the beam diagnostics detectors in the third chamber; photon and cluster beam fluxes, after conversion of the photodiode and microbalance signals with volt-to-frequency converters (VFC); Ar ion counts from a gas-cell in the diagnostics chamber of the GasPhase beamline, for absolute photon flux determination. Each electron or ion detection event is recorded in the mass storage device of the PC, keeping track of the hit channel and of the cluster beam pulse count. Separate files are recorded containing the full information relative to 30 s accumulation time; each file corresponds to one row in a log file where information read from the beamline control system is stored (storage ring parameters, photon energy, undulator's gaps, etc.).

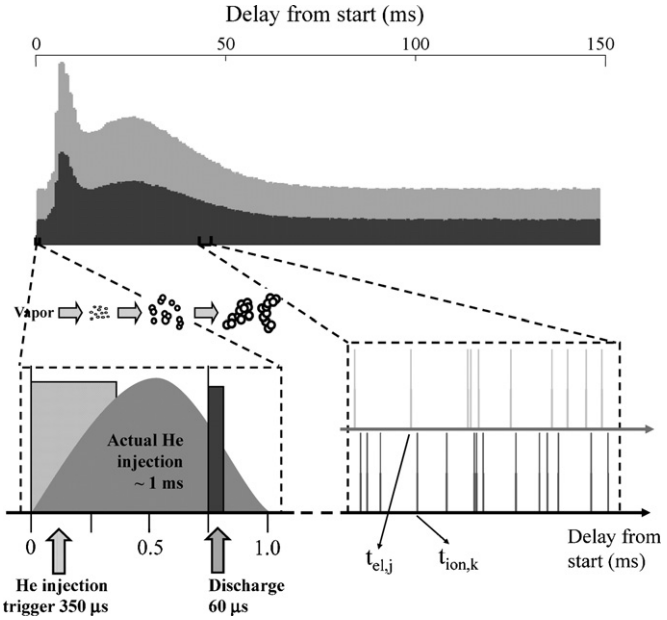

Fig. 5. Typical timing sequence for each working cycle in the experiment; clock is determined by the PMCS controller. A TTL signal synchronized with helium injection in the cluster source cavity starts the time counter of the TDC. Within few hundred microseconds, a high voltage discharge with controlled duration and delay is fired and cathode vaporization occurs; cluster nucleation starts immediately, followed by further growth steps (sketched with an evolution of cluster morphology for sake of exemplification). Due to their velocity (see Fig. 6), clusters travel from the source to the ionization point typically in less than 2 ms; the detection time for ions and electrons (extending up to 60 ms) is therefore mostly determined by particle residence time inside the source cavity. The count rate for electron and ion yields at fixed photon energy are presented at top of the figure and show the evolution of cluster density along each supersonic beam pulse. The two histograms are produced by binning the counts collected by the TDC stop channels over residence time. Profiles are represented with arbitrary intensities by the light grey (electrons; TDC stop channel 8) and the dark grey areas (ions; TDC stop channels 1–7); a baseline of electron and ion counts from the photo-ionization of background gas extends over the whole displayed time range. Data refer to set#1 of PMCS operation parameters. Absolute detection-times $(t_{el})_i$ and $(t_{ion})_i$ of electrons and ions allows the determination of time correlation spectra for the signals. In particular, the presence of bunches in the ion signal can be observed by analysing the *ex post* computed inter-arrival time spectrum. The bunching can be considered in the frame of a multiple cluster fragmentation picture. Electron–ion correlation giving time of flight spectra can be derived *ex post* as well by computing for each ion its delay from the last preceding electron $(t_{ion,k} - t_{el,j})$.

3. Data analysis

The approach to photo-ionization events detection, described in previous paragraph, makes intensive use of information storage and processing technology, thus allowing the application of a number of different analytical tools. These tools, as exemplified in the following, provide unprecedented valuable insight into the free particle properties and the photo-excitation process.

3.1. Signal correlation analysis

Signals obtained from the different detectors show correlation patterns whose most common example is the correlation between an electron and an ion produced in a single photo-ionization event. This is the classical photo-electron photo-ion coincidence (PEPICO) scheme where the spectrum of ion detection time lag after electron detection is obviously interpreted as a time of flight mass spectrum for the ions. This kind of information is obtained from our experimental data after *ex post* computing the detection time differences between each ion and last electron detected before it. This procedure has been applied, e.g. to produce the TOF spectra shown in Fig. 3. More complicated patterns are produced in PEPIPICO where two ions generated in a photo-ionization and fragmentation process are separately detected [27–29]. A single-event-reconstruction approach, though applicable in principle with the available information given by our setup, becomes increasingly complicate for higher number of correlated signals after each photo-absorption event. A more practicable approach is identified in the investigation of different orders of inter-detection time interval distributions for uniform kind of charged particles (electrons or ions).

Inter-detection intervals for consecutive (nearest) events from a uniform distribution of uncorrelated signals are exponentially distributed (this can be clearly observed, e.g. for the background of PEPICO TOF spectra), where the single parameter of the distribution (the exponential decay constant τ) is directly determined by the inverse of counting rate. The next order of inter-detection intervals is obtained by computing the time differences between second-nearest events; following orders (indexed by n) are accordingly defined computing the differences between nth-nearest events. Intervals are Erlang distributed where the n-Erlang distribution function is $f(t, \tau, n) = t^{n-1}e^{-t/\tau}/\tau^n(n-1)!$, with τ determined again by counting rate. A deviation of the inter-detection intervals distribution from the Erlang distribution indicates the presence of signal–signal correlation. Although a direct extraction of the correlation pattern from the intervals distribution is generally quite complicate, when the time scale of signal–signal correlation is significantly different from the inverse of average counting rate τ the intervals distribution can be easily decoupled at order n into a distribution generated by inter-detection intervals including one or more independent events (which is a superposition of different k-Erlang-like distributions with $k = \{1,2, \ldots, n\}$, and whose weights are determined by the correlation pattern), plus a distribution containing quantitative information about the correlation between $n+1$ consecutive signals (Fig. 8).

The results section of this work discusses photon-induced cluster fragmentation in terms of the ion–ion inter-detection interval distribution.

3.2. Cluster velocity measurement

As already mentioned above, spatially resolved ion detection provides access to momentum reconstruction. Clusters in the molecular beam travel along beam direction with a momentum component that is conserved after ionization and consequent acceleration in the perpendicular direction induced by the electric field of the spectrometer. This makes each detector of the channel electron multiplier array sensitive to a given beam velocity dependent window in the time of flight spectrum. The time of flight for each ion is obtained from electron–ion inter-detection time (PEPICO); detector positions relative to ionization point are known after apparatus geometry.

A well-defined velocity measurement can be obtained for each detector from the exact position of its centre and the mode of time of flight distribution recorded by the same detector; owing to the availability of complete timing information, residence-time resolved velocity measurements are performed. Fig. 6 shows the results obtained applying this procedure to data recorded in a 2 ms residence time window centred at 30 ms after gas injection. Different particle velocities are recorded from the different detectors in accord with a size dependent velocity slip; modelling of this dependence, which should include particle morphology parameters accounting for their aerodynamic properties, and extrapolation to carrier gas time of flight allow a determination of carrier gas velocity and thus, to a good approximation, of its stagnation temperature [10,30,31]. Due to the low-efficiency of vibrational-energy cooling of clusters in molecular beams expansions, the carrier gas

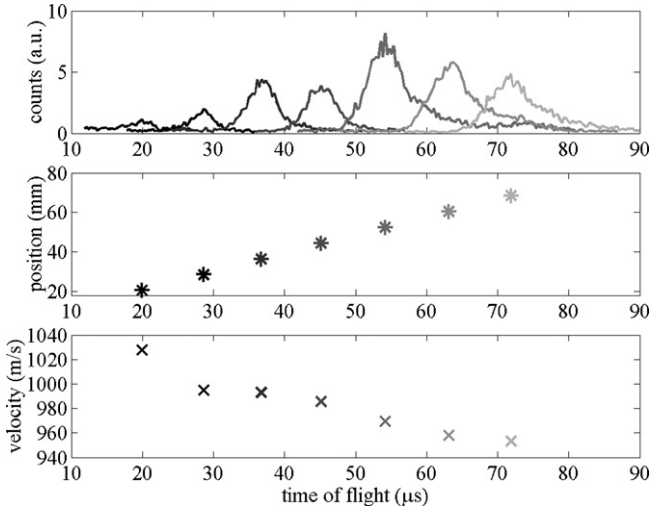

Fig. 6. This figure represents the conceptual scheme adopted for the velocity measurement protocol. In the top picture, a time of flight mass spectrum of titanium clusters is represented. Different grey tones identify signals from different detectors; darkest is detector #1, nearest to the ionization point; lightest is detector #7, most distant from the ionization position. Each detector accepts a different time of flight window. The scatter plot represented in the middle shows the correlation between the time of flight corresponding to the peak in the spectrum relative to each detector and the detector distance from the ionization point measured along the *x*-axis. The position/time-of-flight ratio gives the cluster velocity represented in the bottom figure.

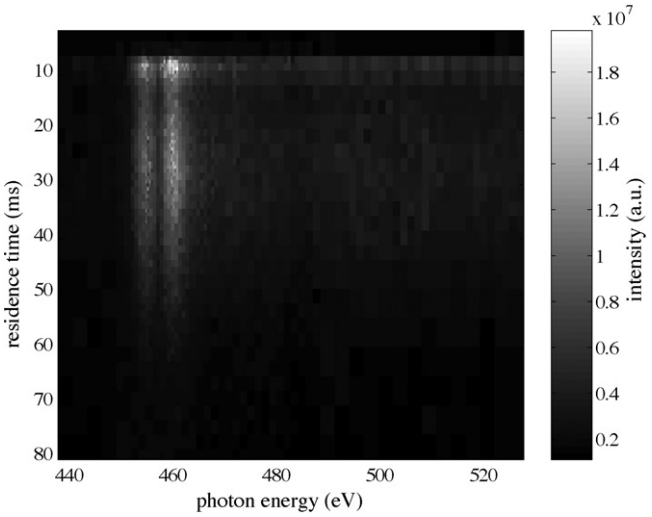

Fig. 7. Colour scale synoptic representation of the PIY XAS spectra for the clusters along the beam pulse. Horizontal sections provide residence time resolved NEXAFS spectra, vertical sections give cluster pulse profiles recorded at a given photon energy. Residence time and photon energy binning is chosen in such a way that each bin contains approximately 200 counts; bin intensity is proportional to counts number scaled by the beam fluxes and bin size.

stagnation temperature can be considered as a reliable estimate for cluster temperature associated to internal degrees of freedom. As expected, due to adiabatic cooling of the expanding gas inside the cluster source, different residence times give different results for the velocity measurement; the corresponding stagnation temperature is in the range 70–100 K for most of the collected signal [10,31].

3.3. Photo-ionization spectra measurement

Electron and ion yield spectra can be obtained from the photon energy dependence of the counting rate on respective channels (after normalization for photon and cluster beam fluxes). Detailed timing information allows the resolution of the spectra into a series with consecutive residence time intervals, and thus introduces the possibility to detect any possible evolution of spectral features with cluster growth and thermal history (Fig. 7). Acquisition during the time period after each cluster beam pulse allows precise background subtraction [10].

The evolution with residence time of NEXAFS spectra can be obtained from properly scaled electron counting rate at different delays from the valve opening [10], giving the possibility to follow the development with the growth conditions of the structural and surface properties of the nanoparticles.

Time of flight resolved ion yield spectra can be extracted from the data after a PEPICO correlation analysis of the events [12]. A determination of true photo-ionization spectra for specific particle size is though a most challenging issue as a precise knowledge of both the charge state of the ions and the possible fragmentation events occurred is essential.

Inner shell photoionization is known to produce ions in high charge states and, due to the broad range of relaxation pathways involving Auger cascades, Coster-Kronig, double Auger and shake off processes, a broad distribution of different charge states is typically encountered [32]; although most systematic data available in literature refer to rare gas atoms, metal atoms show the same behaviour with an even larger average charge state possibly induced by reduced slow electrons recapture in the metals during post collision interactions [33]. Photoion spectroscopy has proven to provide unique information on the de-excitation pathways of atomic vapours [34]; yet, in clusters, the addition of fragmentation issues makes the interpretation of mass spectrometric data exceedingly complicated even at mass resolutions high enough to allow unambiguous determination of charge states. In this frame, the possibility of exerting a control on the mass distribution of the particles through independent parameters like residence time or aerodynamic focusing conditions turns up as a viable approach, in alternative to size selection of clusters ions, for the challenging issue of size-resolved NEXAFS spectroscopy on free particles.

4. Results and discussion

Among the different possibilities opened by the CESyRa setup, we discuss, for sake of exemplification, the results that can be obtained from ion–ion inter-detection interval distributions.

From the inset of Fig. 8 it appears evident that the inverse of counting rate from uniformly distributed signals (i.e. uncorrelated ion counting events producing the exponential distribution shaded in green for 1st-order inter-detection intervals) is over two orders of magnitude smaller than the characteristic time interval between correlated ion counts. Correlated ion count events until over 4th-order inter-detection interval are a significant fraction of total counts and can be clearly distinguished from Erlang-like distributed signal, generated from the combination with isolated ion count events. The presence of a correlation pattern between consecutive ion detection events must be interpreted as an indication that fragmentation processes producing multiple charged fragments occur after a single photo-absorption event. Time-correlated ions are produced (as fragments) after a single photon absorption event; fragments are then detected with a mutual delay depending on their respective measured time of flight. The inter-arrival time distribution of correlated ions should therefore contain information about the size distribution of children clusters produced by fragmentation though a knowledge of the fragments charge state is necessary to perform this analysis. Even if an estimate of the average

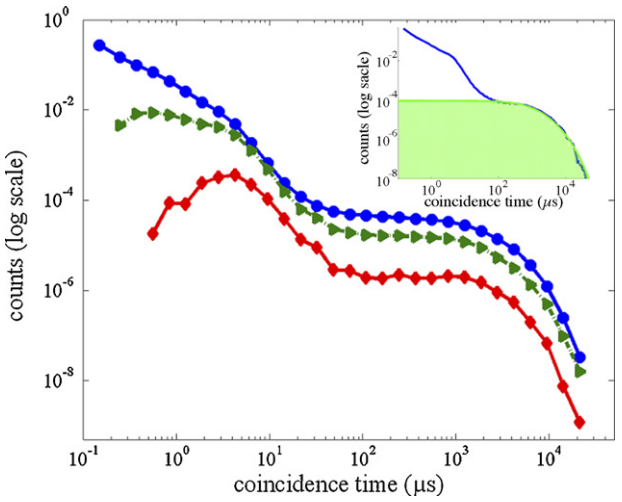

Fig. 8. *n*-Order ion–ion inter-arrival time spectra from titanium clusters ionised with synchrotron light in the energy range 450–530 eV. The spectra are obtained by *ex post* computing differences between the detection time of an ion and of the *n*th following one. 1st-order (circles, blue continuous line), 2nd-order (triangles, green dash-dotted line) and 4th-order (diamonds, red continuous line) spectra are represented in a log-log scale. The inset shows the coincidence spectrum for $n = 1$; here the contribution from independent uncorrelated events is represented by the coloured area. The inter-arrival times between independent signals are Erlang distributed (the *n*-Erlang distribution reduces to the exponential distribution in the $n = 1$ case). The counting rate of independent events is of the order of millisecond, so their contribution can be easily decoupled from the distribution containing quantitative information about the correlation between $n + 1$ consecutive signals. The amount of correlated events is given with good approximation by the number of counts n_c lying below a given threshold (set at 20 μs); in the analysis presented here and in Figs. 9–11, the corresponding number obtained off-beam (discriminated by residence time) is used for background subtraction. (For interpretation of the references to color in this figure legend, the reader is referred to the web version of the article.)

initial charge state can be extracted from a comparison of electron and ion signals, a thorough discussion of the photo-fragmentation process is beyond the scope of present paper; we thus limit the following discussion to an analysis of the number of yielded fragments per photoabsorption event. The detailed description of all different aspects involved in Ti clusters photo-fragmentation including a discussion of electron–ion and electron–electron correlations will be subject of a separate publication which is under preparation.

The observed fragmentation pattern is very surprising in the framework of common understanding of metallic clusters. The stability and fragmentation dynamics of clusters after photoionization is a major issue in cluster physics and has been discussed in many experimental and theoretical publications [35]. Stability against fragmentation has been discussed for simple metal clusters in the frame of indirect dissociation decays, driven by the coupling of the photon induced electronic excitation with the vibrational degrees of freedom; this model leads to statistical evaporation of neutral monomers and/or neutral dimers on a time scale in the range of 10^{-9} to 10^{-6} s [36,37]. For multiply charged clusters, Coulomb repulsion-driven fission starts competing with the evaporation channel for cluster fragmentation. This process has been investigated for multiply charged sodium clusters in the frame of the liquid drop model [38]. In this frame, dissociation of refractory, early transition elements and their compounds is strongly disadvantaged in competition to other indirect decay channels, such as thermally induced electron emission. As a matter of fact, fragmentation in refractory systems like tungsten [39,40], niobium [41] or titanium [42] is commonly neglected in the discussion of photoionization processes involving clusters of these materials.

Our observations call for a different picture than the droplet model to describe cluster structure. Significant insight into the free particle properties can be gathered from a quantitative analysis which, owing to our data acquisition scheme, can be performed with energy and residence time resolution; results are shown in Fig. 9 where the fraction of correlated events is displayed in colour scale for different orders. Non-uniform selection of the bin edges for both energy and residence time is performed in order to keep an approximately uniform signal-to-noise ratio across the map (about 2000 events/bin).

The maps evidence a fragmentation yield up to at least five charged fragments after a single photo-absorption event. It is noteworthy that the fragmentation yield is nearly uniformly distributed respect to photon energy across the Ti–L edge and the continuum region from 440 eV up to 530 eV. This can be appreciated also by comparing the correlation maps with the intensity map reported for sake of comparison in the same figure with the same photon energy and residence time binning. On the other side, the yield shows an increasing trend with cluster residence time for all correlation orders; this trend is more evident from the plots of Fig. 10, where the integral data for the whole energy range above the L-edge are displayed.

The observed photon-energy- and residence-time-dependent fraction of *n*-order correlated ion detection events lays the ground for a complex structural model of titanium nanoparticles formed by the PMCS; the Ti clusters, rather than compact spheroidal particles, are more likely super-aggregates of weakly bound primary clusters. The same model was already proposed about 20 years ago by Cole and Liu [43] in the attempt of explaining the metastable decay of niobium clusters. In their work clusters were produced by a synthesis route showing many similarities with our technique.

Besides providing an appropriate structural model for the interpretation of the observed fragmentation pattern for clusters with high cohesive energy, this hypothesis is also strongly supported by the residence time dependence of the fragmentation yield (i.e. the relative number of temporarily correlated ion detection events; see Fig. 10). A most relevant aspect of this study is actually identified in the possibility to investigate clusters with different thermal histories. In particular, clusters staying longer in the agglomeration chamber have a larger probability to undergo to low temperature coagulation events, resulting in softer agglomerates being more likely to undergo strong fragmentation processes after interaction with VUV light. The specific character of PMCS, namely the fact that different thermodynamic conditions are swept along each cycle, reveals the critical relationship between cluster structural stability and growth conditions; this was also a major claim in the work by Cole and Liu, which remained unconfirmed to date [43].

As demonstrated for aerosol particles by tandem DMA setup [44,45], post-growth thermal treatments can be applied to significantly affect the structure of agglomerate particles; exothermic chemical reactions and molecular sorption processes are additional routes to promote particle sintering or coalescence if sufficient heat is released. Our experimental setup allows particle exposure to reactive species and has been used to investigate the gas phase formation of Ti hydride particles after molecular hydrogen pick-up by Ti clusters in the molecular beam. Electron yield X-ray absorption spectroscopy has been successfully employed to investigate the influence of hydrogenation on the electronic properties of the clusters, and the sensitivity of absorption spectroscopy to the local structure revealed a lattice ordering effect induced by hydrogen chemisorption [10]. When Ti nanoparticles consist of loosely bound aggregates of primary metallic particles, thermal annealing following the strong hydrogen sorption enthalpy (−124 kJ/mol at 300 K for bulk titanium) can produce dramatic consequences on their structure. Information on this process can be obtained from

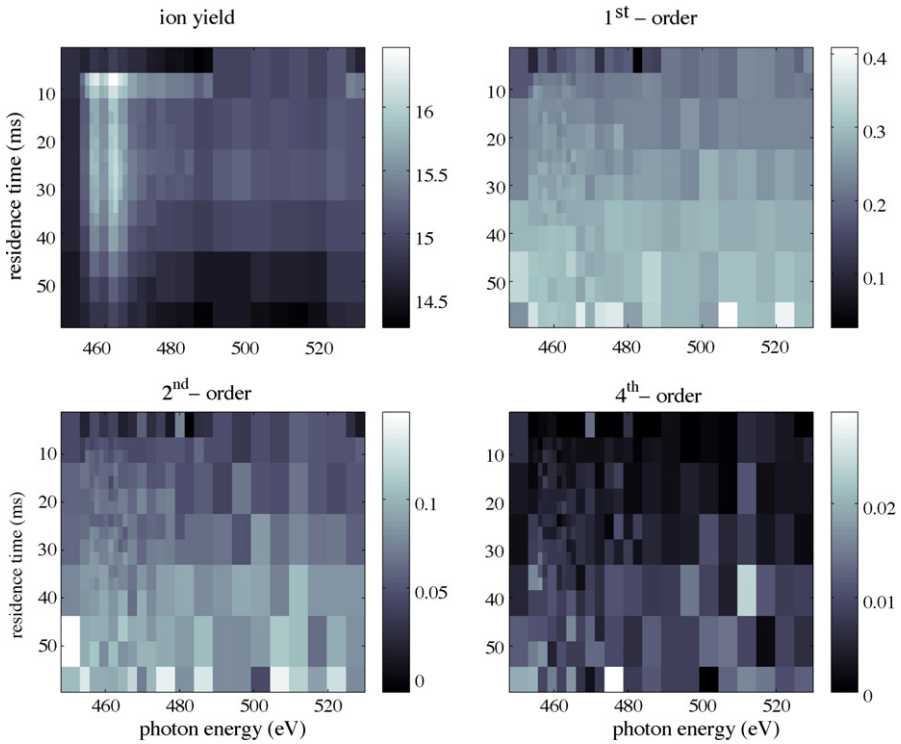

Fig. 9. Colour scale representation of the photon energy and residence time dependence of clusters fragmentation yield as derived from *n*-order correlation analysis. Non-uniform binning is chosen for energy and residence time in order to keep uniform statistical significance over the maps (about 2000 events/bin). The up-left map reproduces in a logarithmic scale the same information plotted in Fig. 7 but with same binning as the three other maps shown here; these represent the fraction of *n*-order ($n = 1, 2, 4$) correlated events. Normalization is performed above the background-subtracted total number of ion counts.

a comparison of the fragmentation yield prior and after hydrogen exposure.

Fig. 11 compares the residence time dependence of the relative number of 1st-order correlated ion signals for Ti and Ti/H_2 clusters. Exposure to hydrogen determines a general decrease of the fraction of particles undergoing fragmentation, still preserving a residence time evolution of the fragmentation yield. We interpret this observation as an effect of the exothermic sorption of H_2 on the particle structure; sintering or coalescence between primary particles forming super-cluster aggregates in the molecular beam is promoted by the heat release, so critically influencing the aptitude of the aggregates to undergo fragmentation.

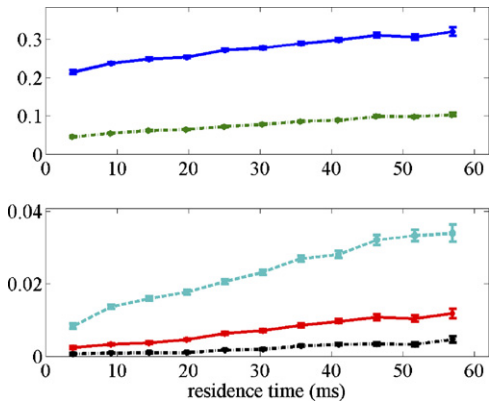

Fig. 10. Residence time dependence of the number of *n*-order correlated events fraction from clusters photo-ionization events. The picture represents from top to bottom 1st- to 5th-order correlated events fraction. The plots refer to data averaged over the 450–530 eV photon energy window.

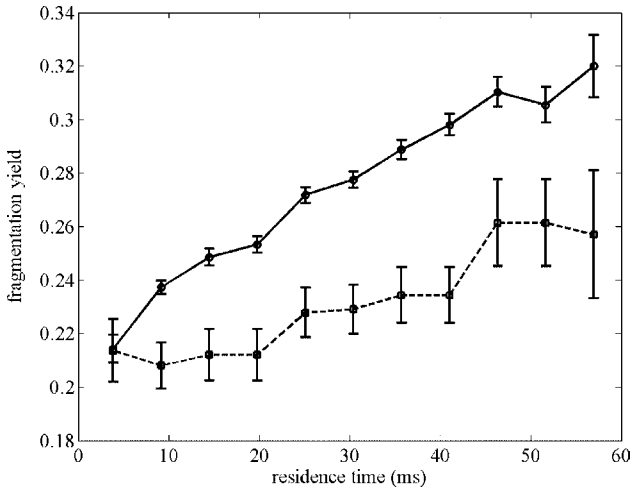

Fig. 11. Cluster residence time dependence of 1st-order correlated events fraction for clusters photo-ionization events with (dashed grey line) and without (full black line) exposure of the free titanium clusters to molecular hydrogen in the pick-up cell.

5. Conclusions

The pursuit of a viable approach to the core-level spectroscopy characterization of free metal clusters has proven to represent an extraordinary challenge. This is because it meets at the same time technological efforts for the realization of a synthesis route guaranteeing high density and stability production of nanoparticles with selected size and structural properties, and the very complex phenomenology of the interaction between VUV radiation and finite systems, a complexity which increases enormously as

soon the probed system departs from simple molecules. We have approached this challenging task by coupling a high flux third generation synchrotron light source with an apparatus for the production of intense supersonic metal cluster beams ensuring the required intensity and stability; a control on the properties of the probed systems has been obtained by exploiting the pulsed character of the cluster source, which provides a sweep over different particle structural properties along every repeated cycle.

In the present work, mainly devoted to the description of the experimental setup and protocol, we present selected applications and results which shed light on the complex structure of the probed metal nanoparticles.

A fragmentation pattern is observed for the first time in transition metal nano-systems interacting with VUV radiation and a correlation of the fragmentation behaviour with the source conditions under which the particles are formed, so as with in-flight treatments inducing structural modifications, is established. A model is proposed for the Ti particles as super-aggregates of weakly bound primary clusters. This picture readily explains the reported experimental results, and introduces an interesting change of perspective within the study of clusters in supersonic beams, underlining aspects that have long been underrated in this field.

Further insight in the complex character of free transition metal nano-systems and of their interaction with VUV radiation is expected to come from a quantitative analysis of the ion inter-detection time distributions, and from the analysis of other correlation patterns (electron–electron, electron–ion); this analysis is in progress and will be dealt with in a forthcoming publication.

Acknowledgments

We acknowledge continuous support at Elettra from the technical electronic service of CNR-INFM, Laboratorio Nazionale TASC (Trieste, Italy), and from our colleagues of the EUFOS group of Sincrotrone Trieste ScpA. M. Amati, M. de Simone and L. Ravagnan are gratefully acknowledged for collaboration to experimental activity during beam-time shifts. GB, PM, PP and TM acknowledge financial support from Fondazione CARIPLO under contract 20060660.

References

[1] J. Bansmann, S.H. Baker, C. Binns, J.A. Blackman, J.-P. Bucher, J. Dorantes-Dávila, V. Dupuis, L. Favre, D. Kechrakos, A. Kleibert, K.-H. Meiwes-Broer, G.M. Pastor, A. Perez, O. Toulemonde, K.N. Trohidou, J. Tuaillon, Y. Xie, Surf. Sci. Rep. 56 (2005) 189.
[2] B. von Issendorf, O. Cheshnovsky, Annu. Rev. Phys. Chem. 56 (2005) 549.
[3] T.P. Martin (Ed.), Large Clusters of Atoms and Molecules NATO Science Series E: Applied Sciences, vol. 313, Kluwer, Dordrecht, 1996.
[4] J. Rockenberger, F. Nolting, J. Lüning, J. Hu, A.P. Alivisatos, J. Chem. Phys. 116 (2002) 6322.
[5] M.G. Mason, Phys. Rev. B 27 (1983) 748.
[6] P. Milani, S. Iannotta, Cluster Beam Synthesis of Nanostructured Materials, Springer, Berlin, 1999.
[7] E. Ruehl, Int. J. Mass Spectrom. 229 (2003) 117.
[8] S.N. Khanna, A.W. Castleman, Quantum Phenomena in Clusters and Nanostructures, Springer, Berlin, 2003.
[9] H.K. Kammler, G. Beaucage, D.J. Kohls, N. Agashe, J. Ilavsky, J. Appl. Phys. 97 (2005) 054309.
[10] T. Mazza, P. Piseri, G. Bongiorno, L. Ravagnan, M. Amati, M. Devetta, C. Lenardi, M. Coreno, M. de Simone, P. Milani, Proceedings of the VUV-XV Conference, Berlin, Germany, 29 July–August 3, 2007, Appl. Phys. A 92 (2008) 463–471.
[11] M. Tchaplyguine, S. Peredkov, A. Rosso, J. Schulz, G. Öhrwall, M. Lundwall, T. Rander, A. Lindblad, H. Bergersen, W. Pokapanich, S. Svensson, S.L. Sorensen, N. Mårtensson, O. Björneholm, Eur. Phys. J. D 45 (2007) 295.
[12] P. Piseri, T. Mazza, G. Bongiorno, C. Lenardi, L. Ravagnan, F. Della Foglia, F. DiFonzo, M. Coreno, M. DeSimone, K.C. Prince, P. Milani, New J. Phys. 8 (2006) 136.
[13] R. Karnbach, M. Joppien, J. Stapelfeldt, J. Woermer, T. Möller, Rev. Sci. Instrum. 64 (1993) 2838.
[14] R.R. Blyth, R. Delaunay, M. Zitnik, J. Krempasky, R. Krempaska, J. Slezak, K.C. Prince, R. Richter, M. Vondracek, R. Camilloni, L. Avaldi, M. Coreno, G. Stefani, C. Furlani, M. de Simone, S. Stranges, M.-Y. Adam, J. Electron Spectrosc. Relat. Phenom. 101/103 (1999) 959.
[15] E. Barborini, P. Piseri, P. Milani, J. Phys. D: Appl. Phys. 32 (1999) L105.
[16] H.V. Tafreshi, P. Piseri, G. Benedek, P. Milani, J. Nanosci. Nanotechnol. 6 (2006) 1140.
[17] P. Liu, P.J. Ziemann, D.B. Kittelson, P.H. McMurry, Aerosol Sci. Technol. 22 (1995) 293.
[18] P. Piseri, A. Podestà, E. Barborini, P. Milani, Rev. Sci. Instrum. 72 (2001) 2261.
[19] W. Koch, S.K. Friedlander, J. Colloid Interface Sci. 140 (1990) 419.
[20] R.C. Flagan, M.M. Lunden, Mater. Sci. Eng. A 204 (1995) 113.
[21] P. Piseri, H.V. Tafreshi, P. Milani, Curr. Opin. Solid State Mater. Sci. 8 (2004) 195.
[22] F. Di Fonzo, A. Gidwani, M.H. Fan, D. Neumann, D.I. Iordanoglow, J.V.R. Heberlein, P.H. McMurry, S.L. Girshirk, N. Tymiak, W.W. Gerberich, N.P. Rao, Appl. Phys. Lett. 77 (2000) 910.
[23] W.A. de Heer, P. Milani, Rev. Sci. Instrum. 62 (1991) 670.
[24] Simulations have been run using a set of codes developed in Matlab® by the authors. Codes are available on request.
[25] http://www.acam.de/fileadmin/Download/pdf/English/DB_AMGPX_e.pdf.
[26] http://www.ortec-online.com/electronics/disc/cf8000.htm.
[27] M. Stankiewicz, P.A. Hatherly, L.J. Frasinski, K. Codling, D.M.P. Holland, J. Phys. B: Atom. Mol. Opt. Phys. 22 (1989) 21.
[28] K. Ueda, J.H.D. Eland, J. Phys. B: Atom. Mol. Opt. Phys. 38 (2005) S839.
[29] N. Saito, Y. Muramatsu, H. Chiba, K. Ueda, K. Kubozuka, I. Koyano, K. Okada, O. Jagutzki, A. Czasch, T. Weber, M. Hattass, H. Schmidt-Böcking, R. Moshammer, M. Lavollée, U. Becker, J. Electron Spectrosc. Relat. Phenom. 141 (2004) 183.
[30] Bu. Wrenger, K.H. Meiwes-Broer, Rev. Sci. Instrum. 68 (1997) 2027.
[31] T. Mazza, Ph.D. Thesis, Università degli Studi di Milano (2007).
[32] A.M. El-Shemi, Y.A. Lotfy, Eur. Phys. J. D 32 (2005) 277.
[33] M.P. Hertlein, H. Adaniya, K. Cole, B. Feinberg, J. Maddi, M.H. Prior, R. Schriel, A. Belkacem, Phys. Rev. A 71 (022702) (2005).
[34] B. Sonntag, P. Zimmermann, Rep. Prog. Phys. 55 (911) (1992).
[35] See e.g. Proceedings of the Fifth International Meeting on Small Particles and Inorganic Clusters, Z. Phys. D 19/20, 1991.
[36] C. Bréchignac, Ph. Cahuzac, J. Leygnier, J. Weiner, J. Chem. Phys. 90 (1989) 1492.
[37] M.L. Alexander, M.A. Johnson, N.E. Levinger, W.C. Lineberger, Phys. Rev. Lett. 57 (1986) 976.
[38] W.A. Saunders, Phys. Rev. A 46 (1992) 7028.
[39] B. Baguenard, J.C. Pinaré, C. Bordas, M. Broyer, Phys. Rev. A 63 (2001) 023204.
[40] H. Weidele, D. Kreisle, E. Recknagel, St. Becker, H.-J. Kluge, M. Lindinger, L. Schweikhard, C. Walther, J. Ziegler, J. Chem. Phys. 110 (1999) 8754.
[41] A. Amrein, R. Simpson, P. Hackett, J. Chem. Phys. 95 (1991) 1781.
[42] A. Herlert, K. Hansen, L. Schweikhard, M. Vogel, Hyperfine Interact. 127 (2000) 529.
[43] S.K. Cole, K. Liu, J. Chem. Phys. 89 (1988) 780.
[44] M.H. Magnusson, K. Deppert, J.-O. Malm, J.-O. Bovin, L. Samuelson, J. Nanopart. Res. 1 (1999) 243.
[45] S. Tsyganov, J. Kästner, B. Rellinghaus, T. Kauffeldt, F. Westerhoff, D. Wolf, Phys. Rev. B 75 (2007) 045421.

2.2 Setup for time-resolved photo-electron spectroscopy of free clusters

The target of the experiment was to investigate the morphology of metal clusters with photo-electron spectroscopy. The experiments were performed in collaboration with the universities of Uppsala (Sweden), Oulu and Turku (Finland) at the I411 beamline [7] of the Max Lab synchrotron radiation facility (Lund, Sweden). Results of the experiments are described in chapter 6.

The apparatus is schematically shown in figure 2.1 and is composed by four differentially pumped vacuum chambers. The first two are the cluster source expansion chamber and a differential vacuum stage; these are the same two chambers used in the XAS apparatus and described in the previous section. The third chamber of the apparatus hosts the electron spectrometer and was developed by the Finnish partners of the collaboration from the universities of Oulu and Turku. The chamber is evacuated by two 300 $^{l}/_{s}$ turbo-molecular pumps granting the required vacuum level of about $5 \cdot 10^{-8}$ $mbar$ during source operation. The support of the chamber was designed to permit its tilt by an arbitrary angle and was employed to put the axis of the electron analyzer at the magic angle of 55° with respect to the polarization axis of the synchrotron radiation. This has lead to the need of the cluster beam being tilted by 35°, which created some complication in the design and mounting of the molecular beam apparatus support (see figure 2.2). Finally the last chamber is a cluster beam dump that prevents the beam to diffuse back to the interaction region and is equipped with a quartz crystal micro-balance to monitor the cluster beam intensity.

The main issue in photo-electron spectroscopy on low density samples is of course the expected low count rate. This problem can be overcome following two ways: by increasing the ionization rate and by increasing the efficiency of the electron spectrometer.

The first way of course implies the increase of the photon flux. In this respect for our first experiments we choose to investigate the level 5d of lead, using 55 eV photon energy because this level has very high cross-section and the maximum flux of the undulator of the I411 beamline is around that photon energy. Despite the low technological interest of lead clusters, this is a perfect system to test the

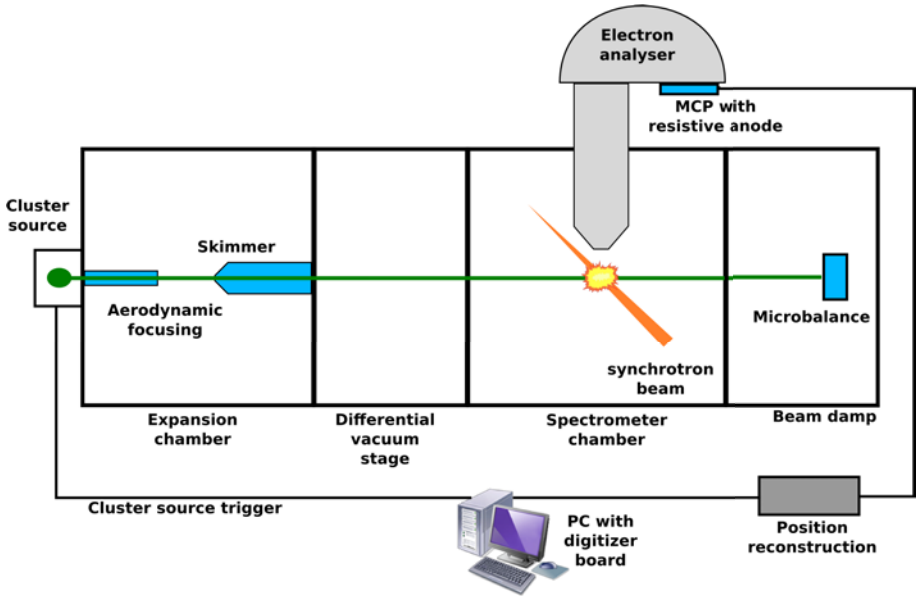

Figure 2.1: Schematic of the apparatus for XPS on free clusters.

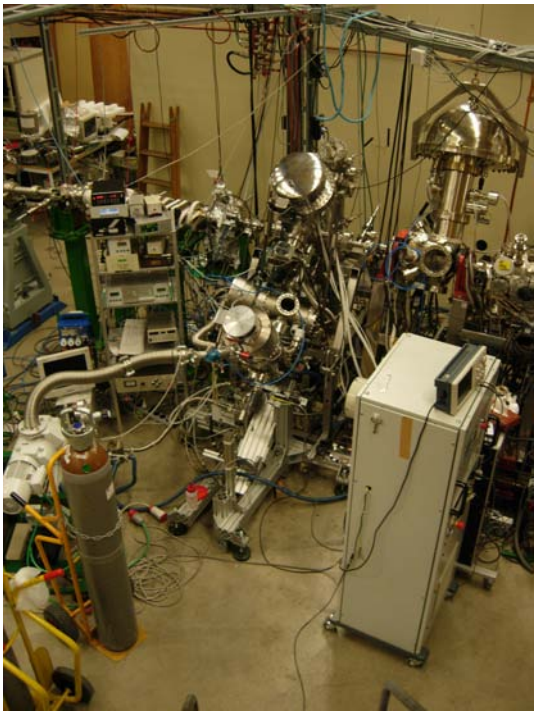

Figure 2.2: The apparatus mounted at the I411 beamline of the Max II storage ring.

apparatus, but also a good sample to study the effect of particle morphology on photo-electron spectra.

The second way for signal improvement is the maximization of the detection efficiency. The employed hemispherical electron analyzer was a modified Scienta SES-100 with a retardation lens system and with the original CCD camera behind the MCP stack replaced by a position sensitive resistive anode (Quantar Model 3394A) [20]. This detector allows to have time resolution of detected electrons; it features though a lower maximum count-rate, which is not a major problem in gas-phase measurements where count rate is quite low due to the dilution of the sample. To further increase collection efficiency, we operated the electron analyzer in a fixed energy window mode.

In our experiment the acquisition was done exploiting the ability of the decoding electronics of the detector (Quantar Model 2401B) to produce an analog signal synchronous with the electron detection event with its amplitude proportional to the hit position on the detector and so proportional to the energy of the electron. These pulses were recorded by a high speed digitizer board (Signatec PDA1000) triggered by the cluster source and then processed by a custom software giving as an output the energy of the recorded electron along with its detection time after the trigger. This scheme allowed to recover a good estimate of the residence time inside the source for the cluster emitting each electron.

The chosen energy resolution was the result of a trade-off between PES spectra resolution and count rate. Considering that the system under analysis is mainly amorphous, a quite relevant broadening of features in the spectra is expected, and so monochromator slits were set up for a photon energy resolution of 70 meV, while the analyzer was configured with a pass energy of 50 eV and entrance slits of 0.8 mm, leading to an overall resolution of 220 meV.

2.3 Setup for photo-fragmentation of free clusters

The target of the experiment was to explore the interaction of complex metal clusters with high intensity EUV radiation. The expected non-linear ionization process was investigated by means of ion spectroscopy. The measurements were performed in November 2009 in collaboration with two Japanese research groups from the

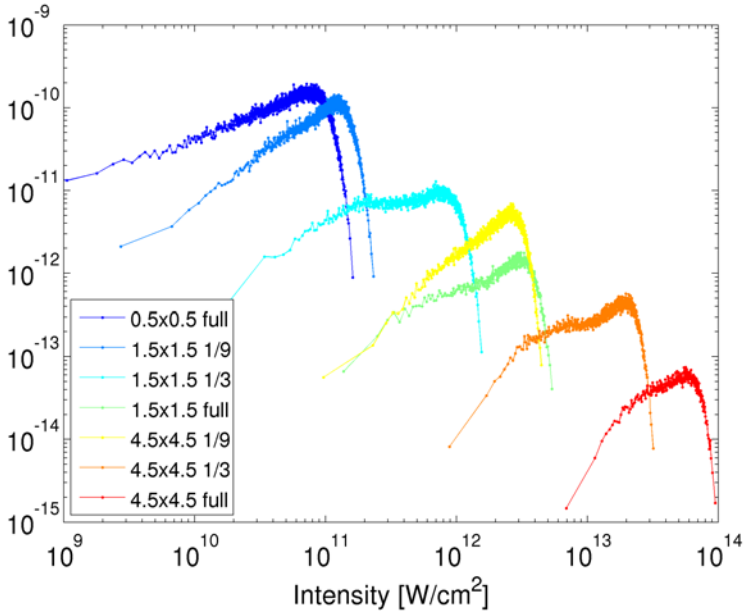

Figure 2.3: Distribution of the intensity of the FEL beam, measured pulse-by-pulse. Two overlapping intensity ranges have been investigated to be able to compare the measurements and verify beam alignment (see text).

universities of Tōhōku and Kyōto. The results are described in detail in chapter 5.

The radiation source used for the experiments was the SCSS EUV FEL test facility of the Spring8 synchrotron radiation laboratory in Japan. This is a free electron laser (FEL) source, based on self-amplified spontaneous emission (SASE), producing radiation with wavelength adjustable between 51 nm ($\sim$24 eV) and 61 nm ($\sim$20 eV), with peak pulse energy of 30 μJ [45]. The pulse duration has been recently estimated from auto-correlation measurement as 30 fs. To regulate the FEL intensity, the user facility included a set of beam cutting slits and a gas cell that can be filled with Ar to damp the beam. To solve the problem of power fluctuations intrinsic in the SASE process (on the order of 10% for this source), a power meter was implemented to get intensity information pulse-by-pulse. A grazing incidence spherical mirror with 1 m focal length and 70% reflectivity, giving a minimum focal spot of $\sim$25 μm FWHM, was employed to focus the beam at the interaction point. The repetition rate used in our experiment was the maximum possible for the facility and was 20 Hz.

Due to diffraction effects, changing the beam size by the slits will change the

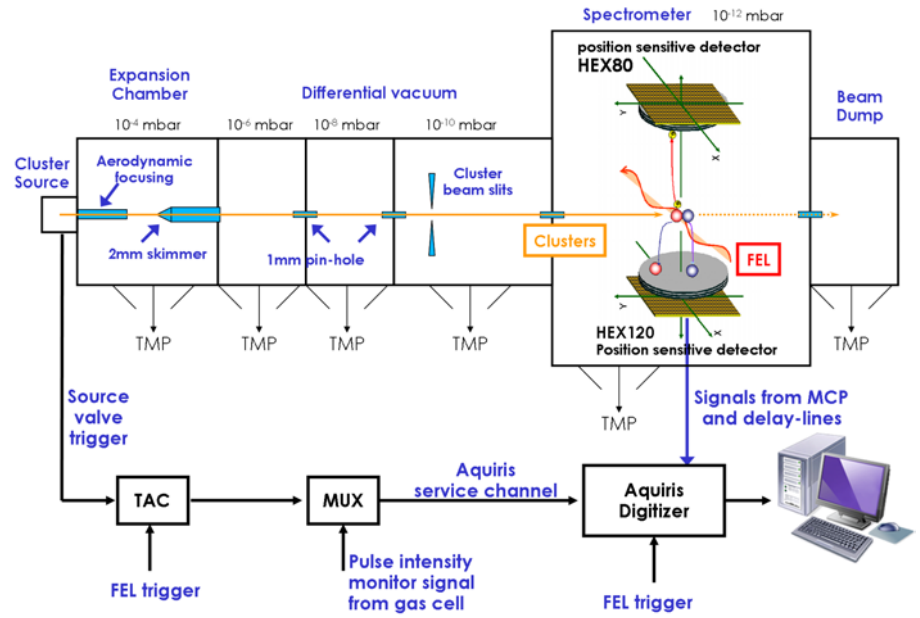

Figure 2.4: Schematic of the apparatus for photo-fragmentation experiments with FEL radiation.

focus size. By a careful calibration of the damp gas cell, it was possible to perform measurements with the same photon density in the interaction region, but with different focus size. In figure 2.3 the ranges of intensity investigated in the experiments are reported. The values refer to the peak power in the FEL beam focus point. The measurements at different focus size (i.e. different ionization volume) but comparable intensity have been employed to verify that cluster and photon beams did effectively overlap during the experiment. The mass spectra of large titanium fragments have been compared at two distinct intensities and different focusing conditions and have been found to match perfectly. Moreover the ratio between the spectra was found to be exactly the ratio between the two interaction volumes, demonstrating that the FEL focus is in fact totally inside the cluster beam (see figure 2.6). This has proven to be a very important check for the interpretation of the experimental data presented in chapter 5.

In the design of this experiment many issues have been faced and solved. First of all, a big problem was coming from the ionization of background gases, that in the available wavelength range have huge cross-sections. A high ionization rate is thus achieved also in the unfocused FEL beam, leading to an interaction volume

for background that is much larger than that for clusters. Then the necessity to detect the many ions with large transverse momentum generated in a fragmentation process, retaining also information about their momentum coming from the molecular beam expansion. And, last but not least, the need for a suitable synchronization mechanism between the FEL and the cluster source to obtain residence time information of the probed clusters.

The apparatus we developed is schematically depicted in 2.4 and is composed by five differentially pumped vacuum chambers. The first two are the expansion chamber of the cluster source and the first differential vacuum stage; these are the same ones used in the XAS apparatus previously described (see section 2.1). The second chamber is connected by a 1 mm diaphragm to two additional differential vacuum stages, also interconnected by another 1 mm diaphragm. The last one also implements two perpendicular sets of beam cutting slits to finely tune the cluster beam dimension and position in the interaction region. Then we have the spectrometer chamber, connected with a 5 mm capillary and finally the dump chamber for the cluster beam. The number of differential vacuum stages and the small diaphragms were necessary to reduce the base pressure from the cluster beam expansion chamber, typically of the order of $\sim 10^{-4}\ mbar$, to the level required in the interaction region to limit the signal from the background, that is of the order of $\sim 10^{-12}\ mbar$.

The spectrometer chamber was developed by our colleagues from Tōhōku University. It is evacuated by a 500 $^{l}/_{s}$ turbo-molecular pump that is backed by another 70 $^{l}/_{s}$ turbo-molecular pump to reach the vacuum levels required by the experiment and holds a vertically mounted time-of-flight (TOF) spectrometer, that is composed by a single acceleration stage, a short drift tube of 70 mm and a large area MCP detector (120 mm in diameter) equipped by a three layers position sensitive delay line anode (RoentDek model HEX120 [22]). The molecular beam and the photon beam cross at 45^{o} in the horizontal plane inside the chamber.

The data acquisition system is one of the most innovative parts of the apparatus. Because of the strong interaction of the FEL radiation with the clusters, leading to an expected high count rate, along with the high contribution of background signal, the requirements on data acquisition in terms mainly of dead-time are huge. In fact a mean number of 100 events per pulse are expected at the highest flux. The core

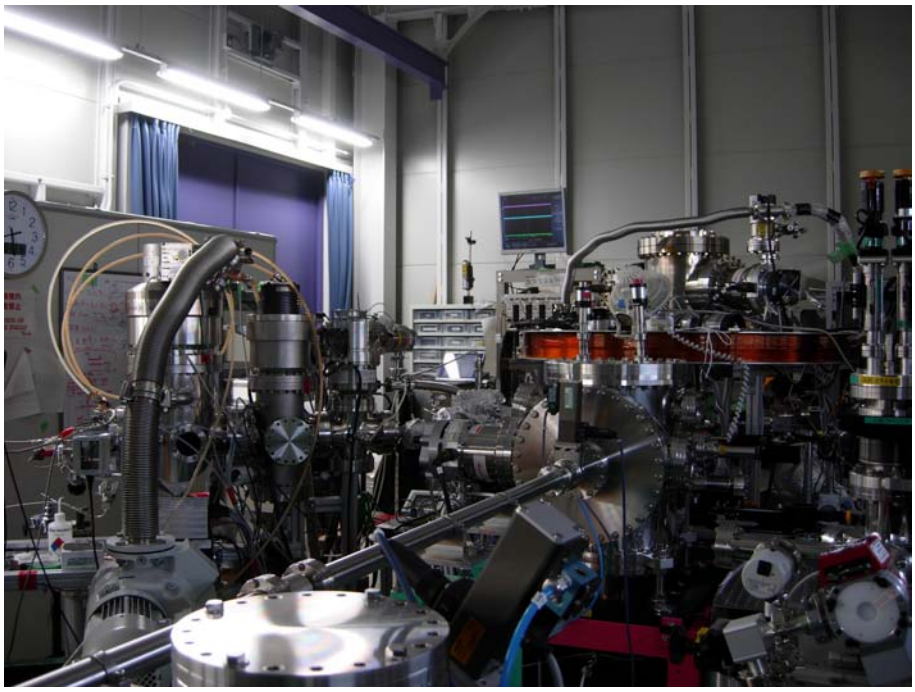

Figure 2.5: The apparatus mounted in the experimental hall of the SCSS EUV FEL at Spring8, Japan.

of the data acquisition system is a fast digitizer (2x Acqiris DC282, 1 GHz sampling rate, 10 bit resolution, 8 channels in total) that acquire for each pulse the six signals coming from the delay line and the signal coming from the back contact of the MCP. All these signals are saved on a PC and then analyzed offline with an ad-hoc developed software reproducing a constant-fraction discriminator (CFD) that has the ability to recover also partially overlapped pulses, thus circumventing the dead-time limitation of hardware CFDs [35]. The last channel available in the digitizer was employed as a service channel to record the pulse energy signal coming from the beamline gas-cell, in order to have pulse-by-pulse the FEL intensity, and the residence time information, as discussed in the next paragraph.

The precise determination of the residence time is fundamental to characterize the evolution of the clusters morphology along the source pulse. During the experiment, the FEL repetition rate was the maximum allowed, i.e. 20 Hz, that means a sampling of the cluster pulse with a period of 50 ms. Of course a shorter sampling period below 1 ms was necessary and a way to sweep the delay between the cluster pulse and the FEL had to be found. In principle it was possible to use a

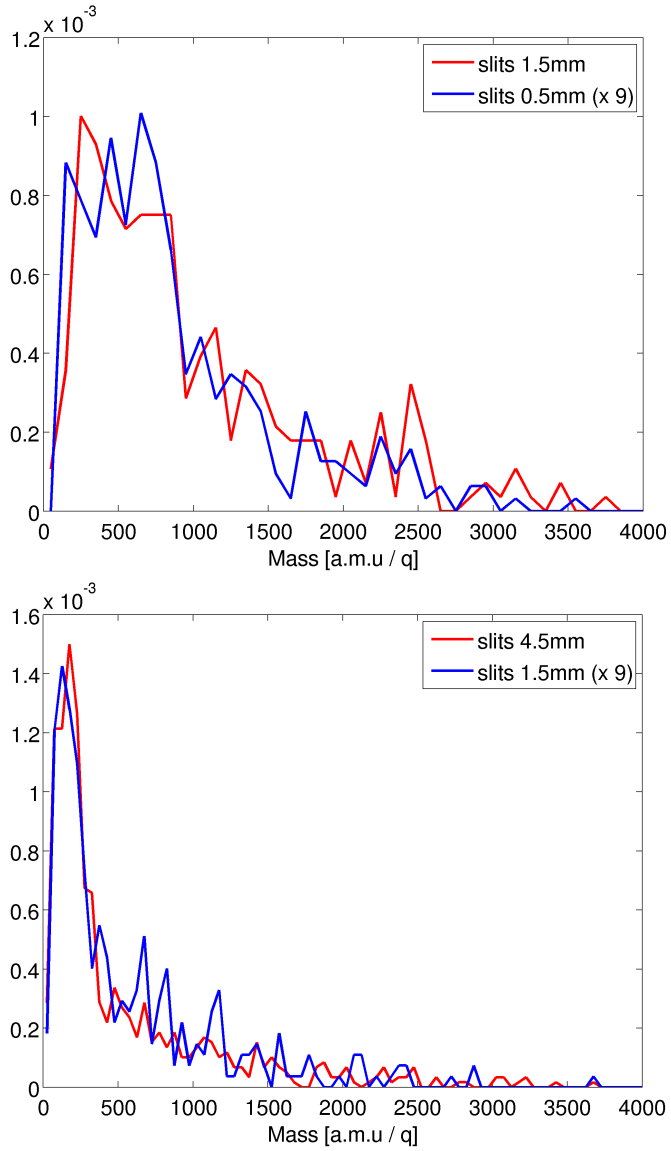

Figure 2.6: Check of the FEL focus alignment with the cluster beam by the comparison of mass spectra taken with the same FEL power density, but different interaction volumes due to different slits configurations. The ratio between the spectra is exactly the expected ratio between the interaction volumes, that is 9. The comparison is done for two different configuration: (a) slits at 0.5 *mm* and at 1.5 *mm* with gas attenuation (photon flux $1.5 - 2.0 \cdot 10^{15}$ ph/cm^2) and (b) slits 1.5 *mm* and 4.5 *mm* with gas attenuation (photon flux $2.0 - 2.5 \cdot 10^{16}$ ph/cm^2).

programmable delay generator to precisely control the trigger of the cluster source with respect to the FEL. But the problem of associating a precise delay pulse-by-pulse would have remained unsolved. The adopted solution was to keep the two sources not synchronized, introducing a small mismatch between the two repetition frequencies, in order to continuously scan the cluster pulse with the FEL. The cluster source was thus triggered by a precision pulse generator (Stanford Research DG535) at 9.95 Hz.

To recover the residence time information we have developed an ad-hoc time-to-amplitude converter (TAC) with a time range extensible up to several hundreds of milliseconds. For each FEL trigger the TAC generates a pulse with amplitude proportional to the delay from the cluster source trigger. These pulses are then recorded by the service channel of the digitizer so to have the residence time information recorded pulse-by-pulse.

Part II

Results and discussion

Chapter 3

sp-rich carbon clusters

Carbon-based materials play a major role in today's science and technology. Thanks to the ability to bond with three different hybridizations, carbon is a very versatile element, which can for example crystallize in the form of diamond or graphite, two materials that expose very different properties. Moreover the recent discovery of new exotic forms of carbon, as are fullerenes and nanotubes, greatly increased the interest in carbon for nanotechnology applications. But besides crystalline forms, carbon can form many varieties of amorphous materials in which hybridizations are mixed in different proportions, leading to a wide range of properties.

Although sp^2-sp^3 amorphous carbons have been widely studied and characterized [15], *sp* hybridization was almost completely missing, except that in small molecules, mainly because of difficulties in its synthesis (for a review see [40]). Nonetheless the interest in the production of nanostructured films with coexisting *sp* and sp^2 hybridization is very high, since *sp* carbon can effectively form nanowires, classified either as cumulenes (virtually conducting, characterized by double C-C bonds) or polyynes (large-gap insulators with alternating single and triple bonds). However, despite several theoretical studies devoted to *sp* carbon nanowires [26, 27, 53, 10], the experimental study of these systems is still at the beginning.

When dealing with carbon clusters, the *sp* chains structure are predicted to be the most stable structures up to some tens of atoms, while larger clusters are predicted to have sp^2 cage-like structures, like fullerenes. However, molecular dy-

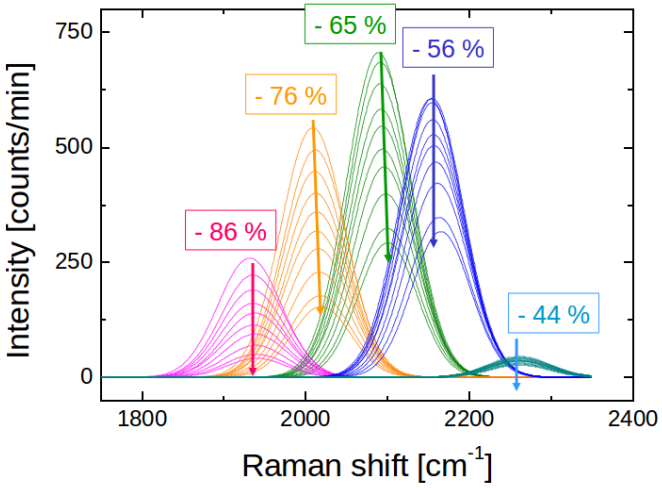

Figure 3.1: The evolution of the C-band modes identified by the real-time monitoring of the decay of the *sp* carbon chains when exposed to low pressure helium.

namic simulation of the aggregation of carbon vapors at low temperature have shown that large sp^2 structures embedding a significant fraction of *sp* hybridization can be metastable [5, 56]. These particular aggregation conditions are that characteristic of the PMCS (for the source description see section 2.1).

In this context, it has been demonstrated that it is possible to stabilize *sp* carbon chains in pure carbon solid by the low energy deposition of metastable carbon clusters produced by a PMCS [42].

3.1 *In-situ* Raman spectroscopy of carbon

The different structures formed by carbon are characterized by different vibrational modes, and so each form of carbon is characterized by a peculiar Raman spectrum. For example, the two crystalline structures of carbon, graphite and diamond, are characterized by two specific vibrational modes, respectively at 1581 cm^{-1} and 1331 cm^{-1}. Even if Raman spectra of mixed sp^2-sp^3 systems are not composed by just a simple combination of these peaks, a great effort has been done in the past to correlate the Raman spectra to specific carbon structures [15].

In particular the Raman spectrum of amorphous carbon films is composed by three main features: the G peak, that is located around $1500 - 1600$ cm^{-1} and

is characteristic of the C-C stretching modes of graphite, the D peak which arise around $1350-1450\ cm^{-1}$ from the presence of disorder and defects in the sp^2 matrix and the C peak around $2000-2200\ cm^{-1}$ that is characteristic of *sp* carbon.

The C peak relative to *sp* carbon has been mainly identified in molecules and was almost missing from pure amorphous carbon. The main reason was demonstrated to be the low stability of *sp* structure when exposed to atmospheric gases and most of the past studies on amorphous carbon were done *ex-situ*.

By depositing carbon clusters produced by the PMCS in UHV and by characterizing the assembled film *in-situ*, it was possible to identify a strong C band in the Raman spectrum [42].

At the beginning, in the C band composition two main contribution were identified: a peak a lower energy assigned to cumulenes and another one at higher energy assigned to polyynes.

In recent measurements, the slow decay of the *sp* species when the film is exposed to low pressure helium gas was measured by real-time Raman spectrometry (one complete Raman spectrum acquired every minute for up to many days of exposure) and many contributions were identified because of their different stability (see figure 3.1).

3.2 Stabilization of *sp* carbon chains in an sp^2 matrix

Therefore the contributions to the Raman C-band from *sp* species cannot be assigned simply to polyynes and cumulenes, but a more varied range of structures is present in the the cluster-assembled film.

In particular, it is important to identify the influence of the chain termination by the sp^2 matrix. For these reason, DFT (density functional theory) calculations have been carried out, investigating the stability of different chain topologies terminated by sp^2 and sp^3 structures. The results of these investigations are reported in the following reprint of a published article.

Effect of Axial Torsion on sp Carbon Atomic Wires

Luca Ravagnan,[1,2] Nicola Manini,[1,3] Eugenio Cinquanta,[1,2,*] Giovanni Onida,[1,3,†] Davide Sangalli,[1,3] Carlo Motta,[1,3] Michele Devetta,[1,2] Andrea Bordoni,[1,2] Paolo Piseri,[1,2] and Paolo Milani[1,2,‡]

[1]*Dipartimento di Fisica, Università degli Studi di Milano, Via Celoria 16, 20133 Milano, Italy*
[2]*CIMAINA, Via Celoria 16, 20133 Milano, Italy*
[3]*European Theoretical Spectroscopy Facility, Via Celoria 16, 20133 Milano, Italy*

(Received 9 February 2009; published 17 June 2009)

Ab initio calculations within density functional theory combined with experimental Raman spectra on cluster beam deposited pure carbon films provide a consistent picture of sp carbon chains stabilized by sp^3 or sp^2 terminations, the latter being sensitive to torsional strain. This unexplored effect promises many exciting applications since it allows one to modify the conductive states near the Fermi level and to switch on and off the on chain π electron magnetism.

DOI: 10.1103/PhysRevLett.102.245502 PACS numbers: 61.48.De, 31.15.A−, 36.20.Ng, 81.07.−b

Postsilicon electronics has seen the recent opening of entirely new perspectives along the way of carbon-based devices. By proper nanoscale design, entirely carbon-made transistors have been realized [1]. Future applications have been devised, including bionanotechnology ones such as devices for fast DNA reading [2]. Even considering only well-demonstrated applications, the potential of carbon-based electronics is undoubtedly enormous, as testified by the realization of nonvolatile memories based on two-terminal atomic-scale switches [3] and bistable graphitic memories [4]. Specifically, these structural memory effects have been explained by the formation of carbon chains made by a few aligned sp-hybridized atoms bridging a nanometric gap [3].

In this context, the production of pure-carbon nanostructured films with coexisting sp and sp^2 hybridization [5,6] opens the exciting possibility to tailor complex carbon-based nanostructures with linear chains made of sp-hybridized C atoms connecting graphitic nano-objects. However, despite several theoretical studies devoted to sp-carbon nanowires [7–10] classified either as cumulenes (virtually conducting, characterized by double C-C bonds) or polyynes (large-gap insulators with alternating single and triple bonds), the implications associated with the nanoscale geometrical manipulation of hybrid $sp + sp^2$ carbon systems are still largely unexplored.

In this Letter we show that sp nanowires can be stabilized effectively by termination on graphitic nanofragments, and that in the resulting structures the $\simeq$1 nm-long linear atomic chains can be torsionally stiff, due to the broken axial symmetry with staggered π bonds. This stiffness is rich in consequences. We explore here how the structural, vibrational, and electronic properties of such chains are affected by the nature and *geometry* of the termination. In particular, we show that sp^2 bonding to graphitic fragments and graphene nanoribbons (NRs) produces remarkably stable structures, with cumulene-type chains displaying a non-negligible bond-length alternation (BLA), so that the traditional categories of polyynes (alternating single-triple bonds, yielding a large BLA) and cumulenes (double bonds, negligible BLA) appear too simplistic for the description of these systems. Torsional deformations are found to affect the BLA, electronic gap, stretching vibrational frequencies, and spin magnetization of the chains.

We study these effects in realistic nanostructures, including carbon chains bound to graphitic fragments. We perform all calculations within density-functional theory in the local spin density approximation, using a plane-wave basis as implemented in the ESPRESSO [11] suite [12].

Figure 1 displays a few of the studied systems involving either sp^2 or sp^3 bonding of a sp nanowire with an sp^2-type fragment. The chosen end-capping nanostructures include planar graphitic fragments and closed-cage clusters (here, C_{20}, the most curved fullerene). These

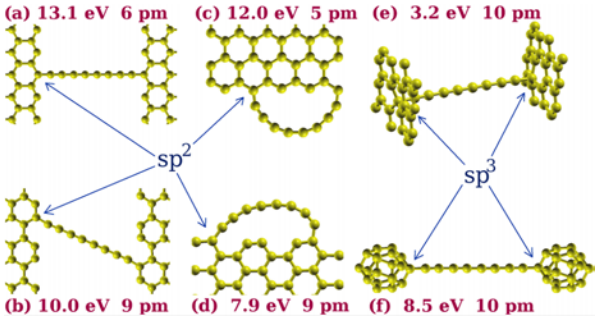

FIG. 1 (color online). A few representative structures involving an 8 atom sp bonded carbon chain terminated on sp^2 carbon fragments [(a e) NRs, (f) C_{20}]. Either edge termination [(a d) sp^2 like] or termination on an internal atom of the fragment [(e f) sp^3 like] is possible. Binding energies (with respect to the uncapped straight chain plus fully relaxed sp^2 fragments) and BLA (expressed in picometers) are reported.

structures are intended to represent typical interfaces present in the nanostructured films produced by cluster-beam deposition [14].

The nature of the terminal bonding turns out to be crucial in determining the structure and electronic properties of the wire. An sp^2-kind termination produces remarkably stable cumulene-type structures (between 7.9 and 13 eV for the formation of the two new bonds), characterized by a BLA between 5 and 9 pm [15]. The computed binding energy should be compared with the energy per bond of 2.1 eV that we obtain for a lateral attachment of the same chain to the ribbon edge, and with the formation energy of graphene edges [13,16]; moreover, it is much larger than the reported binding energies of carbon chains inside nanotubes [17]. Figure 1 also shows that the mere value of the BLA does not allow one to distinguish between carbon chains which would be traditionally classified as cumulenic (a–d) or polyynic (e–f) according to their terminations.

For the sake of comparison we also consider standard cumulenes and polyynes, in the form of isolated carbon chains stabilized by hydrogen terminations. Polyynes C_nH_2 have been synthesized up to a considerable length ($n = 20$) [18,19] in liquid and solid matrices, and also with different stabilizing end groups. Their electronic and vibrational properties as isolated species have been characterized extensively, mainly by electronic and Raman spectroscopy [19,20]. On the other hand, cumulenes $C_{n+2}H_4$ can be seen as C_n sp chains terminated by CH_2 groups, yielding all double C = C bonds. Cumulenes are more elusive and less well characterized than polyynes, due to their fragility. Recently, short cumulenic chains have been synthesized in their basic forms, butatriene and hexapentaene [21]. Cumulenic chains are often produced in conjunction with more complex terminations than simple CH_2 units, including CPh_2, i.e., 1,1 diphenyl ethyl (DPE) groups [22], which we also simulate.

As one could infer from elementary valence bond or tight-binding considerations, depending on the number n of carbons being even/odd, sp^2-terminated cumulenes assume a D_{2h} (planar) or a D_{2d} (staggered) ground-state geometry, respectively, due to the alternating orientation of the π bonds along the chain [21]. Similarly, chains bonded to sp^2 structures are affected by the relative orientation of their terminations. Indeed, a memory of the orientation of the bonds of the terminating sp^2 carbon propagates along the sp-hybridized chain, so that even-n chains tend to relax to a configuration where the termination sp^2 planes coincide, while odd-n chains tend to keep their terminations at a twist angle $\theta = 90°$. As a consequence, despite their purely one-dimensional nature, sp^2-terminated carbon chains display a nonvanishing torsional stiffness, no matter if they are straight or bent as in Figs. 1(c) and 1(d). In contrast, ideally polyynic chains (i.e., those terminated at a sp^3 site, with a pure single-triple bond alternation) are almost completely free to rotate around their axis, but suffer from an obvious frustration when the number of atoms is odd since the long-short bond alternation must swap at their middle [23]. Importantly, in nanostructured cluster-assembled carbon characterized by a complex three-dimensional arrangement of graphitic fragments and sp chains [5,6], a large number of the chains binding to sp^2 structures are not free to relax their terminations to the preferred angular geometry, and must hence be expected to be, in general, strained torsionally.

Since the simulation of carbon-only structures such as graphene NR bridged by chains allows us to investigate a few relative angular arrangements only, we extend our study also to chains with simpler saturating ligands, namely, CH_2 and DPE. The latter turns out to reproduce better the behavior of a large (potentially semi-infinite) graphitic fragment, which, at variance with CH_2, shares with the chain only a fraction of its unsaturated p_z electron, which is partly delocalized over an extended aromatic sp^2 structure.

Figure 2 summarizes the influence of different end groups on the BLA and, for sp^2 termination, the torsional strain energy and the Kohn-Sham electronic gap of even-n chains as a function of θ. Interestingly, largely strained chains undergo a magnetic instability, turning spin polarized. The reason is the quasidegeneracy of two π-bonding or -antibonding electronic levels near the Fermi energy illustrated by the closing of the gap [Fig. 2(b)]. Remarkably, in even-numbered chains of all considered lengths, no matter if CH_2 or DPE terminated, the switching to a spin-polarized configuration takes place at the same twist angle $\theta_s \simeq 79°$, highlighted in Fig. 2 [24]. This θ_s

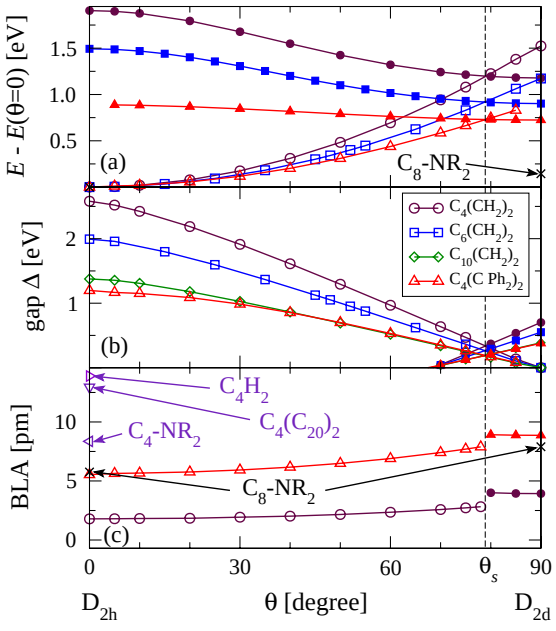

FIG. 2 (color online). Total torsional energy (a), Kohn Sham electronic gap (b), and bond length alternation (c) as a function of the twist angle θ for representative even numbered sp carbon chains with different terminations. Open (filled) symbols refer to the low (high)spin electronic configurations.

invariance implies that the energy gap Δ and the exchange splitting of the electrons near the Fermi level scale in the same way.

Calculations show that the BLA of the sp^2-terminated chains varies substantially with the nature of the termination itself [10]. The length of the extremal bond (i.e., the one connecting the last sp carbon with sp^2/sp^3-hybridized ligand), which correlates with the BLA, is minimal in the case of a simple CH_2 termination, but increases substantially in DPE-terminated chains, assumes even larger values in NR-terminated wires, and is maximum for polyynic-type terminations [see Figs. 1 and 2(c)]. The torsional barrier is consistently smaller for NR terminations, as indicated by the cross at $\theta = 90°$ in Fig. 2(a).

In the light of the above results, chain-termination details are expected to influence the vibrational properties as well. The latter offer an invaluable opportunity to check if the considered structures are representative of those present in nanostructured cluster-assembled films, for which Raman spectra are the main experimental evidence of the presence of linear carbon chains. Indeed, in previous works some of us showed that the Raman fingerprint of carbyne chains in sp-sp^2 carbon is characterized by a broad feature, with 2 components C1 and C2 peaked at 1980 and 2100 cm $^{-1}$, respectively [5,6]. Traditionally these features were attributed generically to cumulenes (C1) and polyynes (C2). We hence calculate the phonon frequencies and eigenvectors of the structures exemplified in Figs. 1(a) and 1(f), plus CH_2- and DPE-terminated carbynes of several lengths, using standard density-functional perturbation theory [11,25]. As a benchmark, our theoretical C-C stretching modes of polyynes C_nH_2 ($n = 8$–12) match the experimental frequencies [20] to within 40 cm $^{-1}$.

Besides several bending and long-wavelength stretching modes, whose low frequency falls in the same range as the vibrations of graphitic and diamondlike carbon material, short linear carbon chains display a few characteristic Raman-active stretching modes in the range $1800 \div 2300$ cm $^{-1}$. One mode, sometimes named the α mode in the literature [20], shows a displacement pattern localized near the chain center, and usually bears the strongest Raman intensity [20]. Since the displacements at the chain ends are less than 10% of those of the central atoms, the frequency of the α mode is almost unaffected by the mass of the termination (e.g., calculations for C_6H_4 and C_8H_4 with 1000-times increased hydrogen mass give frequency shifts of less than 1 cm $^{-1}$).

The stretching frequencies of sp chains turn out to be influenced by (i) the type of termination (sp^3 vs sp^2), (ii) the chain length, with even or odd alternating effects, and (iii) for sp^2 termination, the relative orientation of the termination themselves, with effects of torsional strain. The calculated frequencies of the high-energy Raman-active modes display a clear distinction between sp^2- and sp^3-terminated chains, as shown in Fig. 3. Only even-numbered chains are reported, since odd chains lack α modes, and have in general much smaller Raman cross sections [26].

Figure 3(c) displays the *in situ* Raman spectrum of an sp-sp^2 nanostructured-carbon film [5] in the carbyne region, measured using the 488 nm line of an Ar^+ laser and acquired with very high signal-to-noise ratio. The spectrum of the as-deposited material is compared to that obtained after exposure of the film to He in order to promote sp chain decay [27]. Clearly, a description in terms of two peaks only cannot account for the complex structure and decay observed. In particular, the C_p component at the highest frequency (peaked at 2260 cm $^{-1}$) can be attributed uniquely to short polyynic chains, as it is higher than any cumulenic α mode [see Fig. 3(a)], while the other components can be related both to polyynes and cumulenes of different length. As illustrated in Fig. 3(c), after He exposal, individual components have different evolutions

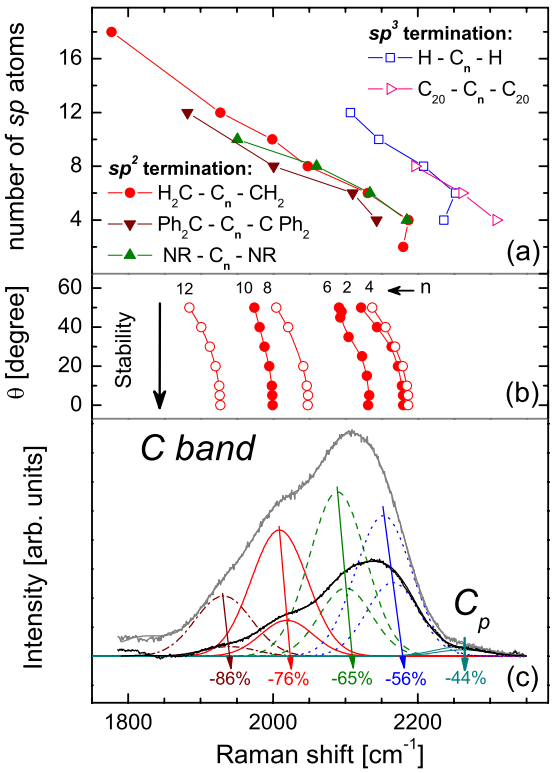

FIG. 3 (color online). (a) The computed frequency of the Raman α mode (horizontal scale) for carbon chains of different lengths n (vertical scale) and with different terminations. (b) The softening of this mode for CH_2 terminated chains as a function of the twist angle θ (vertical scale). (c) The experimental Raman spectra of pristine cluster assembled sp sp^2 film (top grey line) and of the same material after 2 days exposure to He, 100 Torr (black line). The underlying Gaussians report the empirical analysis of both spectra, resulting in 5 components at frequencies separated by approximately 80 cm $^{-1}$. The individual compo nents display different decays, besides becoming narrower and undergoing a $\sim$10 cm $^{-1}$ blueshift.

during the C band decay, and in particular, the peaks at lower energy, corresponding to longer chains, decay faster than the higher-energy ones (i.e., shorter chains). Furthermore, the C_p peak does not shift during the decay or change its width, while all lower peaks are blueshifted by $\sim 10\ \mathrm{cm}^{-1}$ and narrowed by $\sim 7\ \mathrm{cm}^{-1}$. Indeed calculations, summarized in Fig. 3(b), show that the high-frequency stretching modes of torsionally strained CH_2-terminated chains are affected quite strongly by the twist angle, with a redshift up to $\sim 100\ \mathrm{cm}^{-1}$. However, since chains with smaller torsional barrier (such as those bound to DPE and nanoribbons) show smaller redshifts, this effect evaluated for CH_2-terminated chains should be considered as an upper limit for realistic pure-carbon nanostructures.

The observed blueshift of the peaks accompanying the decay can then be explained if each peak is related to a particular family of cumulenes, having all the same length but different strain: the more strained chains, having softer Raman modes, decay faster than the others, resulting in a net blueshift and narrowing of the peak. A faster decay of torsionally strained vibrationally redshifted cumulene-type chains is indeed to be expected due to their higher total energy [Fig. 2(a)]. On the contrary, no torsional strain applies to polyynes, and this is why the C_p peak does not shift.

In summary, we performed *ab initio* total-energy and phonon calculations on a selected range of model structures sampling significantly the infinite variety of three-dimensional arrangements of linear carbon chains bridging graphitic fragments in different hybridization states. Theoretical results suggest that sp-carbon chains are stabilized, in particular, by bonding to the edges of graphitic nanofragments, and allow us to interpret the nontrivial features and decay of experimental Raman spectra of cluster-beam deposited pure-carbon films. Moreover, the data for sp^2-terminated chains point towards a rich phenomenology driven by even/odd alternation effects and by the effects of torsional strain. The latter modifies the electronic states near the Fermi level, suggesting the possibility to control the nanowire conductance [23], optical properties, and spin magnetization, purely by twisting its sp^2 termination, e.g., by coupling terminating graphene sheets with micromachined torsional actuators [28]. Linear carbon chains bridging graphene nanogaps, recently proposed as an explanation of the conductance switching in two-terminal graphene devices [3,4], could hence acquire an important role in future carbon-based electronics.

We acknowledge support by the Italian MIUR through PRIN-2006025747 and by the European Union through the ETSF-I3 project (Grant Agreement No. 211956/ETSF User Projects No. 62 and No. 124).

Note added in proof.—TEM images of chains similar to those depicted in Figs.1(a) and 1(c) have been recently reported in Ref. [29].

*Present address: Materials Science Department, University of Milan Bicocca, Via Cozzi 53, 20125 Milano, Italy
†giovanni.onida@mi.infn.it
‡pmilani@mi.infn.it

[1] Y. M. Lin *et al.*, Nano Lett. **9**, 422 (2009).
[2] H. W. Ch. Postma, arXiv:0810.3035.
[3] B. Standley *et al.*, Nano Lett. **8**, 3345 (2008).
[4] Y. Li, A. Sinitskii, and J. M. Tour, Nature Mater. **7**, 966 (2008).
[5] L. Ravagnan *et al.*, Phys. Rev. Lett. **89**, 285506 (2002).
[6] L. Ravagnan *et al.*, Phys. Rev. Lett. **98**, 216103 (2007).
[7] N. D. Lang and Ph. Avouris, Phys. Rev. Lett. **81**, 3515 (1998); Phys. Rev. Lett. **84**, 358 (2000).
[8] Z. Qian *et al.*, Phys. Rev. B **78**, 113301 (2008).
[9] Ž. Crljen and G. Baranović, Phys. Rev. Lett. **98**, 116801 (2007).
[10] M. Weimer *et al.*, Chem. Phys. **309**, 77 (2005).
[11] P. Giannozzi *et al.*, http://www.quantum espresso.org.
[12] We use the C.pz rrkjus.UPF ultrasoft pseudopotential from Ref. [11] with a wave function or charge cutoff of 30/240 Ry, and relax all atomic positions until the largest residual force is $<2 \times 10^{-4}\ \mathrm{Ry}/a_0$ (8 pN). In the case of periodic graphene NRs, we adopt supercells with three hexagonal units along the periodic direction and at least 7 Å of vacuum separating periodic images in the two other directions, optimizing the lattice constant until the stress tensor drops below $2 \times 10^{-5}\ \mathrm{Ry}/a_0^3$. We sample the Brillouin zone with at least 13 k points in each periodic direction and only $k = 0$ in nonperiodic directions. Numerical details are similar to those validated and used, e.g., in Ref. [13].
[13] T. Wassmann *et al.*, Phys. Rev. Lett. **101**, 096402 (2008).
[14] M. P. Bogana and L. Colombo, Appl. Phys. A **86**, 275 (2007).
[15] The BLA measures the degree of dimerization and, excluding the terminal bonds, can be defined as $\frac{1}{2}[\sum_{j=1}^{n_e}(d_{2j-1} + d_{n-(2j-1)})/n_e - \sum_{j=1}^{n_o}(d_{2j} + d_{n-2j})/n_o]$, with $d_i = |\vec{r}_i - \vec{r}_{i+1}|$, $n_e = (n+2)/4$, and $n_o = n/4$ (integer part).
[16] S. Okada, Phys. Rev. B **77**, 041408 (2008).
[17] Y. Liu *et al.*, Phys. Rev. B **68**, 125413 (2003).
[18] S. Eisler *et al.*, J. Am. Chem. Soc. **127**, 2666 (2005).
[19] T. Pino *et al.*, J. Chem. Phys. **114**, 2208 (2001).
[20] H. Tabata *et al.*, Carbon **44**, 3168 (2006).
[21] X. Gu, R. I. Kaiser, and A. M. Mebel, Chem. Phys. Chem. **9**, 350 (2008).
[22] S. Hino *et al.*, Chem. Phys. Lett. **372**, 59 (2003).
[23] K. H. Khoo *et al.*, Nano Lett. **8**, 2900 (2008).
[24] Odd numbered chains show a reversed behavior, with high spin states near the energetically unfavorable planar geometry $\theta \simeq 0°$.
[25] All phonon calculations start by fully relaxing all degrees of freedom except, in the case of torsionally strained $C_n(CH_2)_2$ systems, the angular coordinates of the H atoms around the molecular axis.
[26] For the simplest structures (CH_2 terminated chains) we also compute Raman intensities.
[27] C. S. Casari *et al.*, Phys. Rev. B **69**, 075422 (2004).
[28] J. A. Yeh *et al.*, J. Microelectromech. Syst. **8**, 456 (1999).
[29] C. Jin *et al.*, Phys. Rev. Lett. **102**, 205501 (2009).

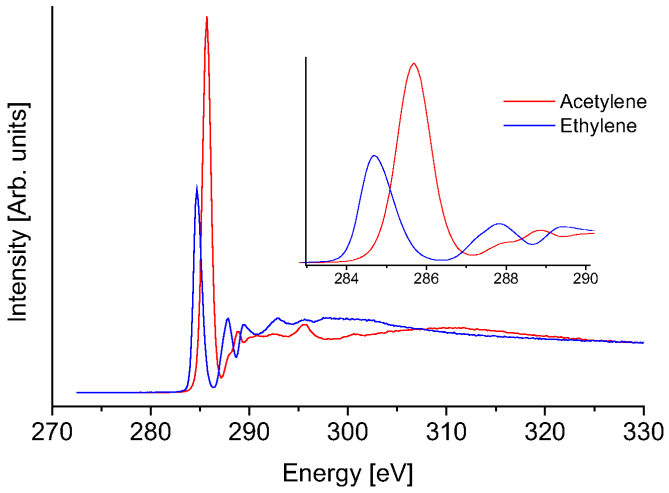

Figure 3.2: EELS spectra of ethylene and acetylene (reproduced from [18]).

3.3 NEXAFS spectroscopy of deposited carbon films

With Raman spectroscopy it was possible to demonstrate the presence of linear carbon chains with *sp* hybridization and to study their stability, but unfortunately the determination of the relative abundance of the different hybridizations is very difficult because Raman cross-sections are not well determined. Moreover the superposition of contributions from vibrational modes of different topologies make this determination even more difficult. It is thus needed an experimental technique with high bond specificity and with well known cross-sections: such technique is Near Edge X-Ray Absorption Fine Structure (NEXAFS) spectroscopy (see section 1.2.2).

Because of the local character of NEXAFS spectroscopy, the spectrum of a complex molecule is assumed to be simply determined by the weighted sum of the spectra of its bi-atomic components. This "building block" approach (BBA) substantially claims that a bond, regardless of being contained in a simple or complex molecule, has always the same NEXAFS spectrum.

Thus the carbon **K** edge (*1s* core level excitation) spectrum of a mixed sp–sp^2 carbon film is expected to show two peaks for the two different π^* resonances, that can be interpreted as the weighted superposition of the spectra of pure sp and sp^2 system. The simplest molecules with this two hybridizations isolated are ethylene for sp^2 and acetylene for sp, which have π^* resonances respectively at $284.7eV$ and

285.9eV (see figure 3.2) [18].

This simple picture holds together only with the assumption that the molecular orbitals are independent from each other. In the case of carbon, being the energy difference between the resonances only 1.2eV, it is likely that some local conjugation occurs. Moreover the amorphous nature of the investigated material imply the presence of bond distortions that can cause slight modifications of resonance energies. As the result of all these phenomena, it is expected that the *sp* and sp^2 resonances will be characterized by broadened and partly overlapping peaks. Then the problem of how to distinguish between the two resonances arises.

However previous studies have shown that the decay of *sp* carbon species can be induced, besides the exposure to gases, also thermally, by heating the sample [41]. It is possible to identify the *sp* contribution to the NEXAFS spectrum by analyzing a sample as-deposited *in-situ*, and after inducing the decay of the chains by a thermal treatment. The difference between the two spectra should clearly show the decay process.

This was done by our group at the Gas-Phase beamline of the Elettra synchrotron radiation laboratory (Trieste). We deposited in-situ a carbon film on a copper substrate that was cooled to 180K. After recording the NEXAFS spectrum, we heated the substrate up to 350K, inducing the decay of the *sp*-chains. Comparing the two spectra, reported in figure 3.3, it was possible to clearly identify the decay of the *sp* species, converted to sp^2 and so to evaluate the content of *sp* hybridization of our deposited nanostructured carbon films [40, 41].

3.4 NEXAFS spectroscopy of carbon clusters in the gas-phase

NEXAFS spectroscopy has proven to be a powerful technique to characterize the abundance of different carbon hybridization in cluster assembled nanostructured films. But during the deposition process, even in a low kinetic energy regime, clusters suffer from structural rearrangement and coalescence, leading to a reduction of the *sp* content. Clusters in the gas-phase are thus expected to show an higher content of *sp* hybridization, being more metastable structures. Moreover the operation principle of the PMCS source (see section 2.1) leads to the production in a

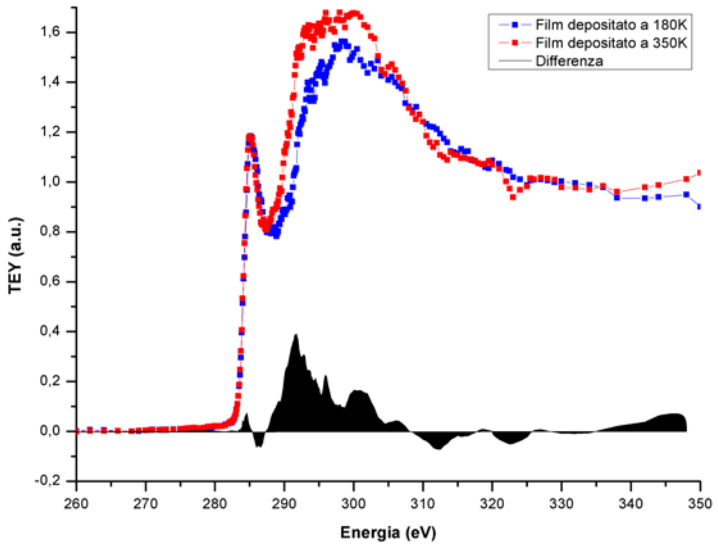

(a) Comparison of two NEXAFS spectra, one of the clusters deposited at 180K, the other one of the deposited film heated up to 350K, inducing sp chains decay.

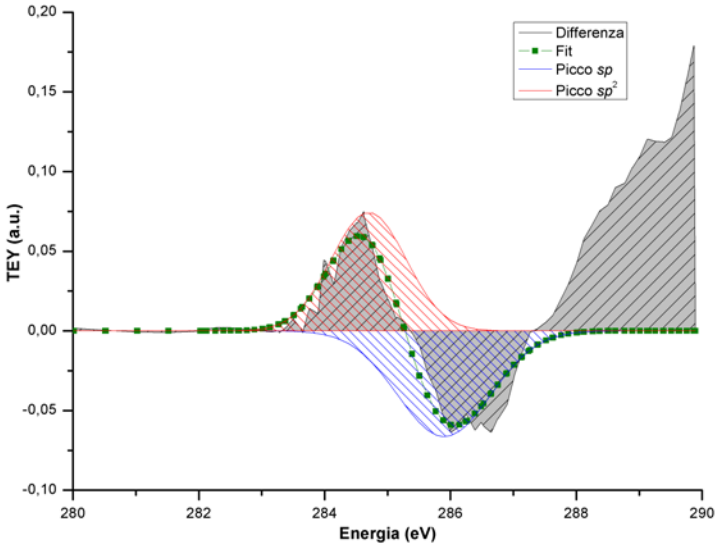

(b) Detail of the spectra difference in the π^* region. It's crearly visible the decrease in the *sp* content that become sp^2.

Figure 3.3: NEXAFS spectra of cluster-assembled nanostructured carbon films.

single pulse of clusters with different residence time in the source and so subject to different aggregation regimes and thermal history.

The following reprint presents the results of the experiment of time-resolved NEXAFS spectroscopy in the gas-phase we performed on carbon clusters produced by the PMCS at the Gas-Phase beamline of the Elettra synchrotron radiation laboratory in Trieste.

L. Ravagnan, T. Mazza, G. Bongiorno, M. Devetta, M. Amati, P. Milani, P. Piseri, M. Coreno, C. Lenardi, F. Evangelista and P. Rudolf, *sp hybridization in free carbon nanoparticles –presence and stability observed by Near Edge X-ray Absorption Fine Structure spectroscopy*, accepted, ChemComm (2010). Reproduced by permission of The Royal Society of Chemistry (RSC).

ARTICLE TYPE www.rsc.org/xxxxxx | XXXXXXXX

sp hybridization in free carbon nanoparticles -presence and stability observed by Near Edge X-ray Absorption Fine Structure spectroscopy

Luca Ravagnan[a], Tommaso Mazza[a], Gero Bongiorno[a], Michele Devetta[a], Matteo Amati[a], Paolo Milani[a], Paolo Piseri[a,*], Marcello Coreno[b], Cristina Lenardi[a], Fabrizio Evangelista[c], and Petra Rudolf[c]

Received (in XXX, XXX) Xth XXXXXXXXX 200X, Accepted Xth XXXXXXXXX 200X
First published on the web Xth XXXXXXXXX 200X
DOI: 10.1039/b000000x

The presence and stability of *sp* hybridized atoms in free carbon nanoparticles was investigated by NEXAFS spectroscopy. The experiments show that a predominant fraction of carbon atoms is found in linear *sp*-chains and that conversion into sp^2 structures proceeds already at low temperature and in the gas phase.

Since their discovery, fullerenes have become the paradigm of carbon nanoparticles (NPs). These highly symmetric, even-numbered carbon aggregates with mixed sp^2 and sp^3 hybridization were first identified experimentally by mass spectrometry of free carbon clusters formed in a plasma,[1] and predicted theoretically to be the energetically most stable structures for cluster with more than 20 carbon atoms.[2]

High yield production of fullerenes from a carbon plasma is obtained only in cluster sources where the aggregate condensation occurs at temperatures above 1000 K.[1,3] At lower temperatures the fullerene yield is low and ill defined carbon NPs that build up the so-called 'carbon soot' are favoured.[3] Fullerene production therefore represents the end point of the carbon NPs aggregation process, the 'fullerene road', which nevertheless is not necessarily reached. Several theoretical models of the fullerene formation steps predict the existence of intermediate highly disordered pre-fullerenic NPs (PFNPs).[4,5] These simulations indicate that PFNPs can consist not only of sp^2 and sp^3 hybridized carbons but also have a significant amount of *sp* hybridization and be remarkably stable.[4,5] The development of the experimental production and characterization of PFNPs represents a very challenging critical step on the route to complex carbon structures.[6]

The presence of *sp* hybridization in solid state carbon has been considered for a long time as very unlikely if not impossible.[7] Although free carbon NPs with less than 20 atoms have *sp*-based structures as most stable configuration (*sp* carbon chains, *sp*CCs),[2] they react exothermically to form sp^2 structures when deposited[8] due to the dangling bonds at the extremities of the isolated *sp*CCs.

Despite the long lasting scepticism about stable *sp*CCs in the solid phase, the feasibility of producing *sp*-rich solid carbon was demonstrated few years ago by some of us by depositing, at room temperature (RT) and in high vacuum, pure carbon NPs produced by a Pulsed Microplasma Cluster Source (PMCS).[9,10] In this source carbon atoms aggregate at a remarkably lower temperature than in standard fullerene sources.[4] The mass distribution of the produced NPs ranges between 10^2 and 10^3 atoms,[11] and thus fullerenes should be the most stable configuration;[2] however, *in situ* Raman spectra of deposited films of these NPs clearly identified the presence of a relevant fraction of *sp* bonds.[9] This *sp* component decays very slowly in high vacuum at RT, while it is rapidly depleted when the film is exposed to oxygen or moderately heated.[11] If the substrate is kept at 150 K during deposition, a remarkable increase in *sp* hybridized atoms is observed.[12] The NPs produced by the PMCS must therefore be PFNPs with high *sp*CCs content and the *sp* chains metastable. In PFNPs the *sp* chains are embedded in a disordered sp^2 structure and their reactive extremities are terminated by bonding to sp^2 (or sp^3) carbon atoms[5] which produces a stabilization of the *sp*CCs,[13] comparable to that achieved by terminating them with bulky endgroups[15] or with graphene[14].

While the spectroscopic study of free PFNPs is essential for a better understanding of the intermediate steps of carbon NP formation, to date *sp* chains have been characterized only in the solid state and not as free NPs prior to deposition.

Here we present the first gas phase characterization performed by Near Edge X-Ray Absorption Fine Structure spectroscopy (NEXAFS) of the bonding structure of *sp*-rich PFNPs produced by a PMCS.

In NEXAFS a core electron is excited to an unoccupied molecular orbital and the resulting core hole filled through fluorescent decay or an Auger process.[16] For carbon the latter is preponderant and by collecting the emitted electrons one obtains a peak in the spectrum each time the exciting photon energy matches the difference between the core level and an empty σ^* or π^* orbital. NEXAFS is thus capable of identifying the chemical bonds present and, via a building block approach, quantify their abundance.[16] In particular, in the C K-edge NEXAFS spectra of C_2H_2 and C_2H_4, the simplest organic molecules with *sp* and sp^2 bonds, resonances occur at 285.9 eV for excitation into $\pi^*_{C\equiv C}$ and at 284.7 eV for $\pi^*_{C=C}$.[16,17], Similarly, distinct resonances (at ~286 eV for *sp* and ~284.5 eV for sp^2) have been identified in more complex sp-sp^2 systems.[18] For pure carbon systems only recently few authors claimed the identification of distinct resonances for *sp* and sp^2 hybridizations.[19,20] Although this might be surprising given the numerous NEXAFS studies in the past, the reason becomes clear when considering that experiments were usually performed *ex situ*, thus exposing the samples to air before characterization. Since the *sp* species are destroyed by oxygen,[9] their identification by NEXAFS was possible only recently on NP films produced *in situ* in a UHV characterization facility,[19] or transported in vacuum to it.[20]

To characterize NPs in the gas phase by NEXAFS we

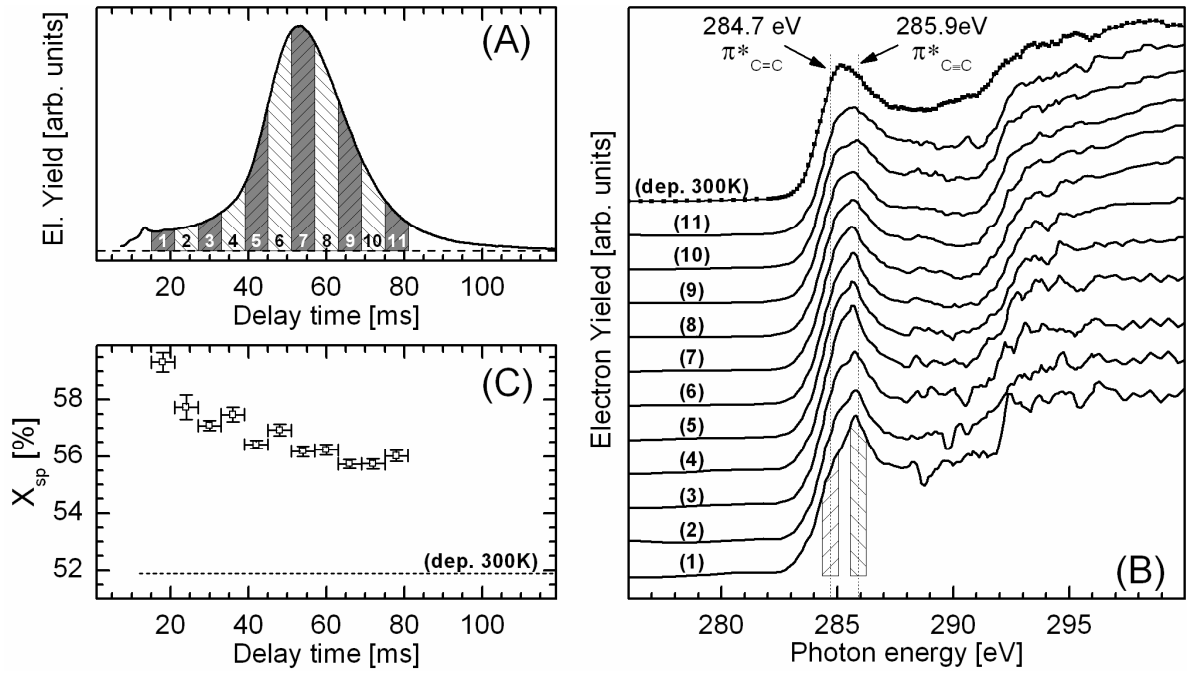

Fig. 1 (A) Electron yield measured for free carbon NPs as a function of the delay time between the PMCS discharge and the electron detection (i.e. the NP residence time in the source). (B) NEXAFS spectra of the free NPs acquired in the 11 delay time windows shaded in panel (A), compared to the ***in situ*** NEXAFS spectrum of the NP assembled film deposited at RT (dep. 300K). The acetylene and ethylene π* resonances are indicated as dotted lines.[16,17] (C) Evolution of X_{sp} (see definition in text) with the delay time; the value of X_{sp} for the deposited film is indicated as a dashed line.

developed a dedicated apparatus, consisting of three differentially pumped UHV chambers [22], and directly interfaced with the Gas Phase Beamline of the Elettra synchrotron in Trieste, Italy.[21] The first chamber hosts the PMCS where the NPs are produced via the aggregation of carbon atoms ablated from a graphite rod through He ion sputtering by a plasma plume.[10] After aggregation, the mixture of NPs and He expands through a focusing nozzle in the vacuum chamber, forming a highly collimated molecular beam.[10] Since the nozzle's conductance is low, ~ 100 ms are required after each of the source's working cycles for emptying completely the source cavity. During that time, the NPs in the cavity can interact, aggregate and structurally rearrange at a temperature as low as ~100 K.[4] As a result the NP size and structure evolve with residence time in the source. After exiting from the cavity, their further evolution is quenched by the collisionless and cool environment of the molecular beam.[10] The central part of the NP beam enters the second chamber through a skimmer. Here the ionic component of the beam is deflected by an electrostatic field, while neutral NPs reach the interaction chamber through a small diaphragm, where they cross the soft x-ray beam coming from the beamline. Differential pumping of the three chambers and the high collimation of the NP beam ensure a pressure in the 10^{-9} mbar range in the interaction chamber. The emitted electrons are collected by a channeltron connected to counting/timing electronics;[22] the detector signal is fed into a time-to-digital converter triggered by the PMCS discharge, so that electron counts can be resolved as a function of detection time within each source pulse. Time resolved NEXAFS spectra are obtained by ***a posteriori*** binning the data and by normalizing the electron yield to the x-ray flux and to the NP flux.[22]

Figure 1A shows the electron yield measured at different delay times after the electrical discharge producing carbon vaporization in the PMCS (shading is used to highlight the time windows applied for time resolved data shown in figures 1B and 1C). The delay time is the residence time of the NPs in the cavity plus a small interval due to the time of flight from the source to the interaction region (~1 ms, with a little spread for different parts of the NP beam pulse).

Figure 1B presents the NEXAFS spectra for each of the eleven delay time intervals marked in Fig. 1A. A total electron yield NEXAFS spectrum of the film obtained by depositing the NPs at 300 K on a copper substrate is also shown for comparison. A clear evolution can be observed: the spectra of the first NPs exiting from the source are sharply peaked at ~285.7 eV, an energy consistent with the acetylene-type $\pi^*_{C\equiv C}$ resonance at 285.9 eV (marked by a dotted line in the figure).[17] Thus the first NPs exiting the source are characterized by a predominantly ***sp*** bond structure. To the best of our knowledge this is the first NEXAFS spectrum of a pure carbon system displaying a sharp π* peak indicative of ***sp*** hybridization.

As the delay time increases (going from spectrum 1 to 11 in Fig. 1B), the peak at 285.7 eV progressively decreases, though remaining the predominant feature at the π* edge of the spectrum, while a shoulder at ~284.7 eV (i.e. $\pi^*_{C=C}$) grows. Finally, in the spectrum of the deposited film, the acetylene-type $\pi^*_{C\equiv C}$ peak is not any longer the predominant feature and the $\pi^*_{C=C}$ peak shows a similar intensity.

Fig. 1C shows the evolution of the fraction of NEXAFS signal related to ***sp***-bonds as a function of delay time (***i.e.*** NP residence time inside the source). This fraction is calculated as $X_{sp}=100xA[\pi^*_{C\equiv C}]/A[\pi^*_{C=C}+\pi^*_{C-C}]$, where $A[\pi^*_{C\equiv C}]$ and $A[\pi^*_{C=C}]$ are integral intensities from the spectra in Fig. 1B in two 0.6 eV wide energy windows centred at 284.7 eV and 285.9 eV, respectively (shaded regions in Fig. 1B). Ordinate error bars account for the variation of intensities when varying

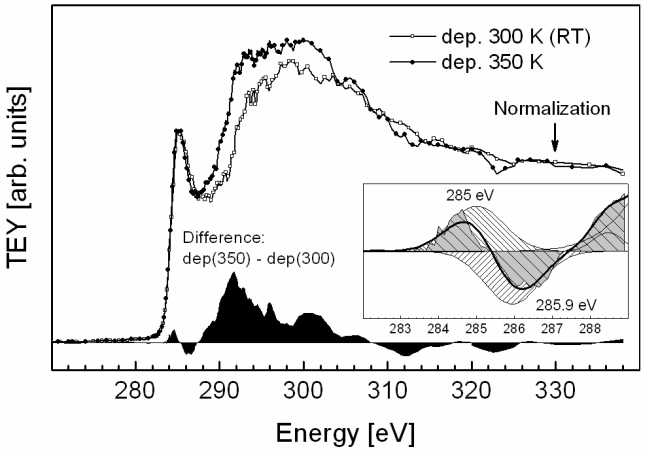

Fig. 2 Total electron yield NEXAFS spectra (normalized to the post edge region as indicated by the arrow) of NP assembled films deposited at RT (dep. 300K) and at 350 K (dep. 350K). The difference spectrum is indicated in black, and its Gaussian fit is shown in the inset.

the integration interval from 0.1 to 1 eV width, while the abscissa error-bars relate to the width of the delay time intervals. Although this definition of X_{sp} is only qualitative, it avoids the high arbitrariness involved in spectra fitting, especially concerning the choice of the fitting curve for the post edge region.[20,23] As can be clearly seen in Fig. 1C, the amount of *sp* bonds present in the NPs decreases monotonously with increasing residence time, remaining nevertheless much higher than the amount of *sp* detected on the NP assembled film deposited at RT (dashed line in Fig. 1C). This indicates that during all phases of the NP formation in the PMCS, the aggregates are composed of a major fraction of *sp*CCs, in good agreement with the theoretical prediction for the low temperature aggregation process of carbon.[3,5] The chains are metastable and evolve progressively towards sp^2 structures during residence time in the source; nevertheless a relevant fraction of the *sp*CCs is able to survive even after NP deposition at RT, confirming that the end-capping of the chains by bonding to sp^2 groups afford a remarkable stability to carbon atomic wire structures.[13]

To further follow the decay process of *sp*CCs, we deposited the NP also on the copper substrate kept at 350 K (see refs. [11,12]). Figure 2 shows the NEXAFS spectra, normalized to the post edge region, from the film deposited at room temperature and at 350 K, as well as the difference between these two spectra. Substrate heating causes a substantial change in both the π* and the σ* regions of the spectrum: as evident from the difference, the change in the π* region is related to the decay of the $\pi^*_{C\equiv C}$ band at 285.9 eV and the corresponding increase of the $\pi^*_{C=C}$ band at 285 eV.

In conclusion, we demonstrated the *sp* hybridization of free carbon NPs by NEXAFS and followed the evolution of their structure on a millisecond time scale under low temperature conditions in an inert atmosphere. Our results show that free carbon NPs can have a complex structure with varying relative amounts of *sp* and sp^2 *bonds*. This has very important consequences for a wide variety of fields where carbon NPs play a role such as astrochemistry and environmental sciences.

Measurements were supported by the "Access to Research Infrastructure" action of the EU Human Potential Program.

Notes and references

[a] *CIMAINA, Università degli Studi di Milano,Via Celoria 16, I-20133 Milano, Italy.*
[b] *CNR-IMIP, Montelibretti (Rome) and Gas Phase Beamline ELETTRA, Area Science Park, I-34149 Trieste, Italy*
[c] *Zernike Institute for Advanced Materials, University of Groningen, Nijenborgh 4, 9747AG Groningen, The Netherlands*
* corresponding address: paolo.piseri@fisica.unimi.it

1 R.E. Smalley, *Acc. Chem. Res.*, 1992, **25**, 98.
2 R.O. Jones, *J. Chem. Phys.*, 1999, **10**, 5189.
3 T. Wakabayashi, D. Kasuya, H. Shiromaru, S. Suzuki, K. Kikuchi, Y. Achiba, *Z. Phys. D*, 1997, **40**, 414.
4 Y. Yamaguchi, L. Colombo, P. Piseri, L. Ravagnan and P. Milani, *Phys. Rev. B*, 2007, **76**, 134119.
5 G. Zheng, Z. Wang, S. Irle and K. Morokuma, *J. Nanosci. Nanotechnol.*, 2007, **7**, 1662.
6 G. Benedek, H. Vahedi Tafreshi, E. Barborini, P. Piseri, P. Milani, C. Ducati, J. Robertson, *Diam. Relat. Mat.*, 2003, **12**, 768.
7 R.B. Heinmann, in *Carbyne and Carbynoid Structures*, ed. R.B. Heimann, S.E. Evsyukov, and L. Kavan, Kluwer Accademic press, Dordrecht, 1999, pp. 7–15.
8 T. Wakabayashi, A.-L. Ong, D. Strelnikov and W. Krätschmer, *J. Phys. Chem. B*, 2004, **108**, 3686.
9 L. Ravagnan, F. Siviero, C. Lenardi, P. Piseri, E. Barborini, P. Milani, C. S. Casari, A. Li Bassi and C. E. Bottani, *Phys. Rev. Lett.*, 2002, **89**, 285506.
10 K. Wegner, P. Piseri, H. Vahedi Tafreshi and P. Milani, *J. Phys. D: Appl. Phys.*, 2006, **39**, R439.
11 C.S. Casari, A. Li Bassi, L. Ravagnan, F. Siviero, C. Lenardi, P. Piseri, G. Bongiorno, C.E. Bottani and P. Milani, *Phys. Rev. B*, 2004, **69**, 75422.
12 L. Ravagnan, P. Piseri, M. Bruzzi, S. Miglio, G. Bongiorno, A. Baserga, C. S. Casari, A. Li Bassi, C. Lenardi, Y. Yamaguchi, T. Wakabayashi, C. E. Bottani and P. Milani, *Phys. Rev. Lett.*, 2007, **98**, 216103.
13 L. Ravagnan, N. Manini, E. Cinquanta, G. Onida, D. Sangalli, C. Motta, M. Devetta, A. Bordoni, P. Piseri and P. Milani, *Phys. Rev. Lett.*, 2009, **102**, 245502.
14 C. Jin, H. Lan, L. Peng, K. Suenaga and S. Iijima, *Phys. Rev. Lett.*, 2009, **102**, 205501.
15 W.A. Chalifoux and R.R. Tykwinski, *C. R. Chimie*, 2009, **12**, 341; S. Kim, *Angew. Chem. Int. Ed.*, 2009, **48**, 7740.
16 J. Stöhr. *NEXAFS spectroscopy*, Springer, New York, 1992.
17 A.P. Hitchcock and D.C. Mancini DC, *J. Electron. Spectrosc.*, 1977, **10**, 749.
18 F. Matsui, H. W. Yeom, I. Matsuda and T. Ohta, *Phys. Rev. B*, 2000, **62**, 5036; A. Fujimori, M. Ishitsuka, H. Nakahara, E. Ito, M. Hara, K. Kanai, Y. Ouchi and K. Seki, *J. Phys. Chem. B*, 2004, **108**, 13153.
19 L. Ravagnan, G. Bongiorno, D. Bandiera, E. Salis, P. Piseri, P. Milani, C. Lenardi, M. Coreno, M. de Simone and K.C. Prince, *Carbon*, 2006, **44**, 1518.
20 J. Diaz, O. R. Monteiro and Z. Hussain, *Phys. Rev. B*, 2007, **76**, 094201.
21 K.C. Prince, R.R. Blyth, R. Delaunay, M. Zitnik, J. Krempasky, J. Slezak, R. Camilloni, L. Avaldi, M. Coreno, G. Stefani, C. Furlani, M. de Simone and S. Stranges, *J. Synchrotron Rad.*, 1998, **5**, 565.
22 P. Piseri, T. Mazza, G. Bongiorno, M. Devetta, M. Coreno, P. Milani, *J. El. Spectr. Rel. Phen.*, 2008, **166-167**, 28.
23 I. Jiménez, R. Gago and J.M. Albella, *Diamond Relat. Mater.*, 2003, **12**, 110.

Chapter 4

Accessing the fractal dimension of free clusters

By employing the SBMA technique described in section 1.2.1, the fractal dimension of free Ti nanoparticles produced by a PMCS have been characterized.

The first experiments to validate the model have been carried out at the Gas-Phase beamline of Elettra synchrotron radiation facility with the apparatus described in section 2.1, also used for XAS on carbon clusters.

A more refined SBMA measurement was possible with the data acquired in the photo-fragmentation experiments performed at the SCSS EUV FEL in Japan (see chapter 5).

4.1 First results of SBMA in XAS experiments

XAS measurements were performed around the Ti 2p edge, in the photon energy range $450 - 470\ eV$. Core level excitation induces photo-fragmentation and formation of multiply charged fragments, complicating the analysis of the mass-to-velocity relationship. Nonetheless the employed apparatus gives access to single event reconstruction, allowing the unambiguous discrimination of correlated and independent ion detection events and the consequent identification of the contribution of unfragmented clusters to the time-of-flight (TOF) spectrum. Moreover a mean charge state value can be estimated by the total fraction of reconstructed

events (after an estimate of the electron detection efficiency) and compared to the results of the fitting procedure described hereafter.

TOF spectra from clusters selected in a given residence time window and collected by three different elements of the channel electron multiplier (CEM) array (see section 2.1) are shown in figure 4.1a; TOF spectra from other residence time windows and other CEM array elements present analogous features. TOF spectra are modeled as the sum of contributions from differently charged clusters which, after ionization, share similar mass-to-charge ratios and velocities. The TOF spectrum collected by each element of the CEM array has been analyzed by a fitting procedure resolving charge-dependent modes, which are described by Gaussian line-shapes accounting for cluster velocity distribution and, through their amplitude, for the ion detection efficiency of the detector. The fitting procedure identifies modes position and intensity with the following conditions:

1. the average charge state of measured clusters population must match the value obtained from detector efficiency considerations; this puts a constraint on the relative weight of the different charge state contributions for each CEM (see figure 4.1b);

2. for each charge state the intensities of the contributions to the mass spectrum collected by the different CEMs must be described by a single log-normal curve representing the cluster mass distribution (figure 4.1c); both the mode and the geometric standard deviation parameters are determined by the fitting procedure and the average mass of clusters increases with increasing residence time (inset of figure 4.1c).

Within the present description, each mode position identifies a data point in the mass-velocity diagram (figure 4.2); the analysis of the TOF spectra from different CEMs in the array and for different residence time values (t_{res}) provides a measurement of the velocity-to-mass relationship $v = v(m, t_{res})$ over a wide mass range ($\sim 300 - 600$ Ti atoms) and over a large residence time span (sufficient statistics to perform the described fitting procedure is available in the $15 - 40$ ms interval).

The $v = v(m, t_{res})$ data points can be fitted by least-squares with the model expressed by equation (1.10), after making explicit the σ dependence from m as

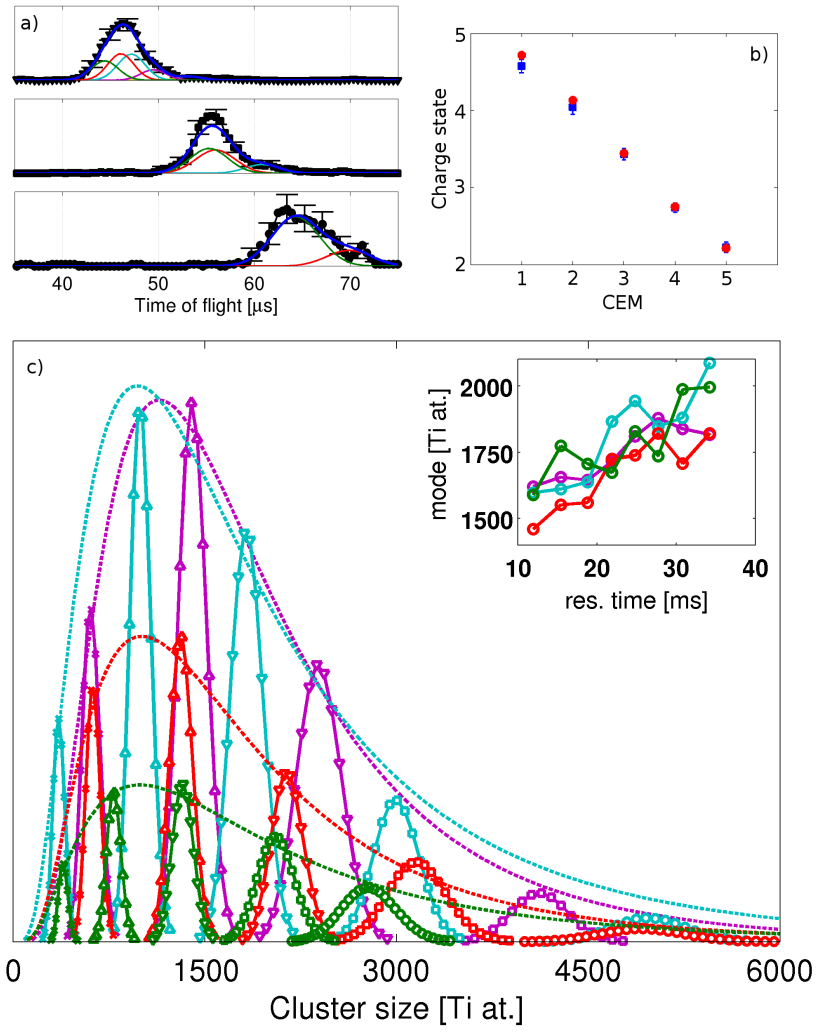

Figure 4.1: (a) Ti clusters time-of-flight distributions recorded by elements #3 (top), #4 (center) and #5 (bottom) of the channel electron multiplier (CEM) array, for clusters with residence time in the $17-20$ *ms* interval. For each spectrum is reported the fitting by superposition of Gaussian-shaped modes corresponding to different charge states (+2 in green, +3 in red, +4 in cyan, +5 in magenta and the sum in bold blue). (b) Comparison of the average charge state (red circles) of clusters detected by each CEM element from the weighted mean of the charge-dependent modes with the clusters population charge state (blue squares) determined from the evaluation of the overall fraction of reconstructed events [32]. (c) The contributions to the TOF spectra recorded in the $23-26$ *ms* residence time window by the different CEM elements (x for CEM#1, upward triangles for CEM#2, downward triangles for CEM#3, squares for CEM#4 and circles for CEM#5) from 2-fold, 3-fold, 4-fold, 5-fold charged clusters (colors as in a) are plotted here vs. cluster size. It is also reported the log-normal mass distribution obtained by fitting the values at peak maxima for each of these charge states contributions (broken line). The inset shows the residence time dependence for the best-fit log-normal mode.

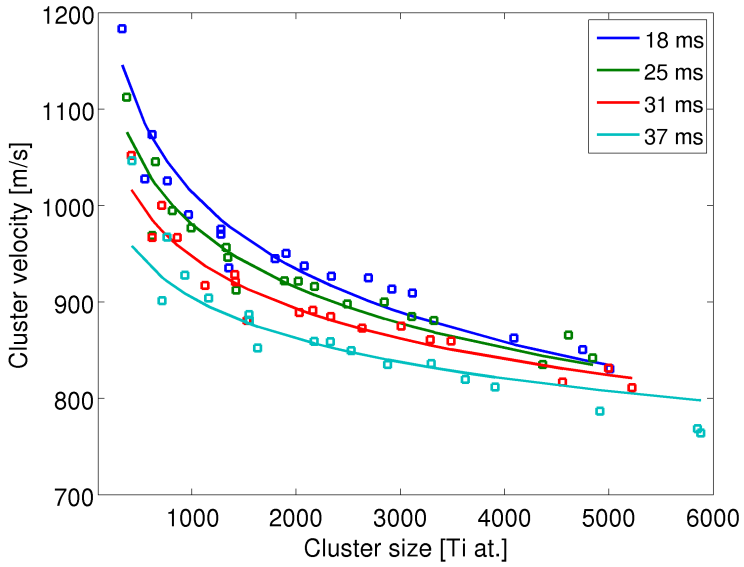

Figure 4.2: Mass-to-velocity relationship for titanium clusters from selected residence time windows. Each point is obtained by center values (time of flight and detector position) from a single mode with defined charge-state (and thus unambiguously determined mass from time of flight). Full lines represent the best fit to the experimental data with the model described in the text.

(by recalling equation (1.11))

$$\beta \cdot \sigma = \tilde{\beta} \cdot m^{D^*/D} = \tilde{\beta} \cdot m^{\xi} \tag{4.1}$$

This allows the mapping of the fractal dimension parameter describing the morphology of the particles populating different portions of the pulsed cluster beam.

A set of additional conditions between the model parameters is assumed in order to reduce the number of degrees of freedom and use the available experimental data in the most effective way:

1. a quadratic dependence of $\xi = D^*/D$ with residence time is assumed as a second order approximation of any existing trend in cluster fractal dimension:

$$\xi = \xi_0 + \xi_1 \cdot t_{res} + \xi_2 \cdot t_{res}^2 \tag{4.2}$$

2. The dependence on residence time of the carrier gas velocity is assumed to be [34]

$$v_{gas} = v_{gas,0} \cdot e^{-\frac{t_{res}}{2\tau}} \tag{4.3}$$

and the effective collision number pre-factor $\tilde{\beta}$ is described by the product of the density of gas flux J_{gas} (that is proportional to the to gas density n_{gas} times the gas velocity v_{gas} [31]) and the expansion's duration Δt (taken inversely proportional to v_{gas}):

$$\tilde{\beta} \propto J_{gas} \cdot \Delta t \propto \left(n_{gas} \cdot v_{gas}\right) \cdot v_{gas}^{-1} = n_{gas} \tag{4.4}$$

Assuming adiabatic conditions gas density scales as $T_s^{1/(\gamma-1)}$ (i.e. $T_s^{3/2}$ in case of helium) while gas velocity scales as $\sqrt{T_s}$ according to equation (1.2), giving the following expression of n_{gas}

$$n_{gas} \propto \cdot e^{-\frac{3t_{res}}{2\tau}} \tag{4.5}$$

finally leading to

$$\tilde{\beta} \propto T_s^{\frac{1}{\gamma-1}} \Longrightarrow \tilde{\beta} = \tilde{\beta}_0 \cdot e^{-\frac{3t_{res}}{2\tau}} \tag{4.6}$$

3. The average collision effectiveness $\langle\alpha\rangle$ is assumed fixed for all clusters under investigation and is included in pre-factor $\tilde{\beta}_0$.

4. The carrier gas stagnation temperature time constant τ is related to the gas release time constant τ_r (according to stagnation chamber volume and nozzle conductivity) by

$$\tau = \tau_r \cdot \frac{\gamma}{\gamma - 1} \tag{4.7}$$

The value is determined as 110 *ms* from an independent direct measurement (a residence time-resolved partial ion yield measurement on molecular oxygen seeded in the supersonic He beam).

With ξ_0, ξ_1, ξ_2, $v_{gas,0}$ and $\tilde{\beta}_0$ as free parameters, the least square fitting procedure

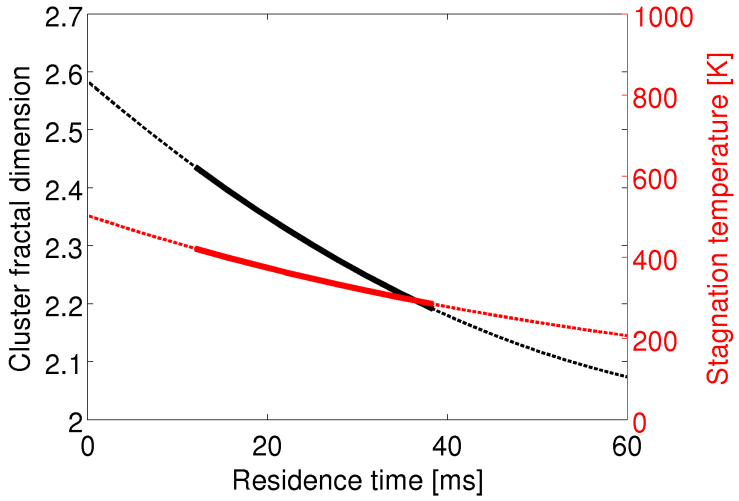

Figure 4.3: Residence time evolution of cluster fractal dimension (black) and carrier gas stagnation temperature (red) as determined by the least-square fitting procedure described in the text. The full lines represent the result in the investigated residence time range, whereas dotted lines show extrapolation according to the assumed empirical model for expansion evolution.

shows an increasing trend for the D^*/D ratio with increasing residence time of Ti clusters (from ∼0.8 to ∼0.9 in the range $15-40$ ms).

A numerical solution of expression for D^*-D given by Nelson et al. [36] is consistent with the observed ξ values only if the observation scale r_{obs} is greater than ∼1.1 nm; this result holds for any decay rate of the cut-off function used in the description of density correlation. The value of the observation scale r_{obs} is determined from the normalized observation scale X of Nelson et al. as $r_{obs} = X \cdot r_{cluster}$ (iteration of the numerical solution is needed because cluster size $r_{cluster}$, determined from the observed m values, scales with the obtained fractal dimension). This should be interpreted as a lower limit to the inner scale of the fractal-like physical object imposed by finite primary particle size of the aggregates. Based on the comparison between the mass of a primary particle of this size, and the observed cluster mass, this solution would then imply a typical number of primary particles per cluster not greater than ~ 4, a situation which is not compatible with the observation of a fractal like scaling of σ versus m. Therefore the experimental result have to be interpreted assuming that $D > 2$ and this means that $D^* = 2$ and $D = 2/\xi$.

Therefore the observed increasing trend for ξ results in a decreasing trend for the fractal dimension of the Ti clusters with increasing residence time (from ~ 2.5 to ~ 2.2 in the range $15 - 40$ *ms*, see figure 4.3).

4.2 SBMA with FEL

After the first results, a refined experiment was set up at the SCSS EUV FEL facility with the apparatus described in section 2.3. The advantages of the new setup are the higher statistics available with an event-by-event mass-to-velocity information and the availability of a direct measurement of the gas expansion dynamic, that in the previous experiments was only modeled by an ideal adiabatic expansion.

The measurements were done using the FEL in low photon flux conditions, i.e. less than 10^{15} ph/cm^2, that is a regime in which the photon absorption rate increase almost linearly with the photon flux. Moreover, fragmentation processes are not dominant and are mainly fission-like, with effects on the m/q distribution similar to those of multiply ionized clusters. This is demonstrated in figure 4.4 that shows experimental m/q distributions at different, but relatively low photon fluxes.

The analysis is divided into four sections: the first deals with the estimate of the original mass distribution of the clusters, the second with the estimate of the charge state event-by-event, the third with the experimental estimate of carrier gas expansion parameters (i.e. density and velocity) and the last one presents the results for the fractal dimension of the clusters.

4.2.1 Estimate of the original mass distribution

The m/q distribution is modeled by the sum of different log-normal distributions, one for each charge state, weighted by the probability of that state. The original log-normal mass distribution, with parameters μ and σ is expressed by

$$f_{\mu,\sigma}(m) = \mathrm{logN}(m,\mu,\sigma) = \frac{1}{\sqrt{2\pi}\log(\sigma)\cdot m} e^{-(\log(m)-\log(\mu))^2/2\log^2(\sigma)} \tag{4.8}$$

The charge state of a cluster of mass m is described by a Poisson distribution with parameter

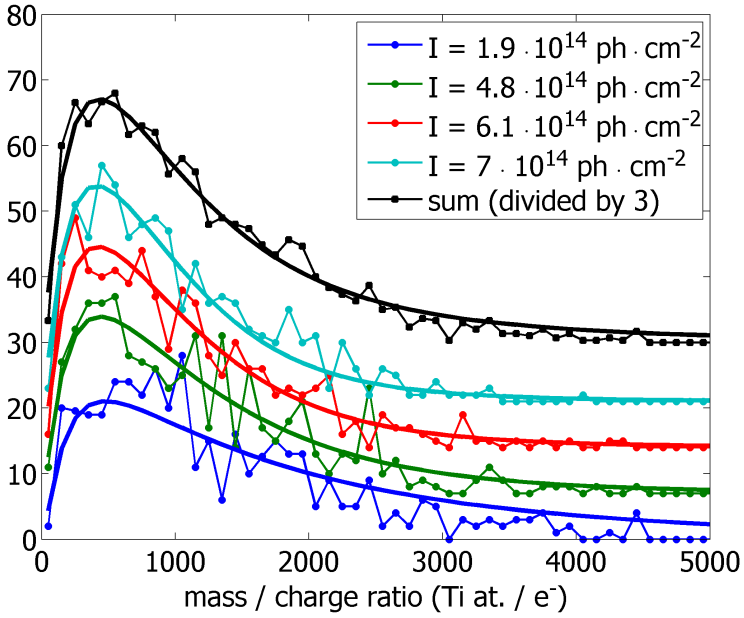

Figure 4.4: $^{m}/_{q}$ distribution of clusters with residence time $8-14$ *ms*. Different spectra (from bottom to top) refer to different increasing photon flux measurements. The spectra are fitted by the model distribution discussed in section 4.2.1.

$$\lambda = r \cdot m^{\beta} \tag{4.9}$$

where r is the ionization probability of a single atom, and β is the scaling power of the probability with the cluster mass.

It's then possible to write a q-resolved mass distribution for each charge state in the form

$$g_{\mu,\sigma}(m,q) = \mathrm{logN}(m,\mu,\sigma) \cdot w(m,q) \tag{4.10}$$

where

$$w(m,q) = w(\lambda,q) = \frac{e^{-\lambda} \cdot \lambda^{q}}{k!} \tag{4.11}$$

is a weighting function that take into account the probability of the specific charge state.

The $g_{\mu,\sigma}(m,q)$ can the be converted into the corresponding $^{m}/_{q}$ distribution

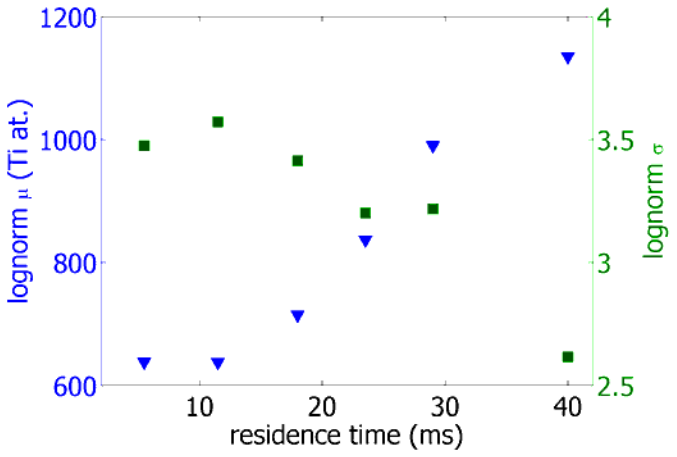

Figure 4.5: Residence time evolution of μ and σ parameters as obtained from the fitting of photon flux resolved $^m/_q$ spectra, as discussed in the text.

$$g_{\mu,\sigma}\left(\frac{m}{q}\right) = k \cdot \mathrm{logN}\left(\frac{m}{q}, \frac{\mu}{q}, \sigma\right) \cdot w(m,q) \tag{4.12}$$

Using this model, the $^m/_q$ spectra for a specific residence time window and for varying photon flux are fitted simultaneously with common μ and σ parameters. The other free parameter β is assumed common to all the residence time intervals considered. Figure 4.4 shows an example of the fitting procedure, while the results for μ and σ for all the residence time windows considered are shown in figure 4.5. The obtained value for parameter β was 0.8.

4.2.2 Event-by-event charge assignment

For each detected event, it is known the time-of-flight (TOF) t_f, the position on the detector p, the residence time t_{res} and the photon flux n_{ph}. By the calibration of the spectrometer $[t_f, p]$ can be converted to $[^m/_q, v]$. From the photon flux and the residence time we know the corresponding mass distribution to which the cluster belongs and also the relative ionization probabilities. To assign a charge state to each event, a maximum likelihood criterion was employed, as an exact direct assignment is not feasible.

Given n events in a interval of TOF $[t_1, t_2]$, the expected abundance of a charge state q is given by

$$u(q,t_{1,2}) = \frac{n \cdot \text{logN}\left(t_{1,2}, \frac{\mu}{q}, \sigma\right) \cdot w(\lambda(t_{1,2}), q)}{\sum_{k=1}^{\infty} \text{logN}\left(t_{1,2}, \frac{\mu}{q}, \sigma\right) \cdot w(\lambda(t_{1,2}), q)} \tag{4.13}$$

where the $\text{logN}(t_{1,2}, {}^{\mu}/_{q}, \sigma)$ is defined in equation (4.8) and $w(\lambda, q)$ is defined in equation (4.11).

The distribution of the charge state can be expressed by a tuple d of q_{max} elements

$$d = \left\{n_1, n_2, n_3, \ldots, n_{q_{max}}\right\} \quad : \quad \sum_{q=1}^{q_{max}} n_q = n \tag{4.14}$$

where q_{max} is an arbitrary cut-off chosen such that $u(q,t)$ is negligible for $q > q_{max}$.

The set d is chosen among all the possible sets by a maximum likelihood criterion by minimizing the quantity

$$\tilde{\chi}^2 = \frac{1}{q_{max} - 1} \cdot \sum_{q=1}^{q_{max}} \frac{(n_q - u(q,t_{1,2}))^2}{u(q,t_{1,2})} \tag{4.15}$$

To maximize the reliability of the assignment an ordering scheme of the events is introduced, based on the assumption that if two cluster with masses m_1 and m_2 are accelerated by the jet in identical conditions, then $m_1 > m_2$ implies that $v_1 < v_2$.

Of course taking n as bigger as possible can reduce the error due to the discretization of the assigned set d, but because of limited statistic it was chosen $n = 15$. In these conditions the reliability of the assignment method was estimated as 75% of good assignments.

Figure 4.6 reports the measured ${}^{m}/_{q}$ along with the reconstructed mass distributions that well fits the expected distribution described by

$$f(m) = \text{logN}\left(m, \mu\left(t_{res}\right), \sigma\left(t_{res}\right)\right) \cdot \left(1 - e^{-\lambda}\right) \tag{4.16}$$

Figure 4.7 then presents the scatter plot of the reconstructed events.

4.2.3 Estimate of gas density and velocity

At sufficiently high FEL photon flux, probability of helium double ionization becomes sufficiently high to measure a clear signal. This has made possible a direct

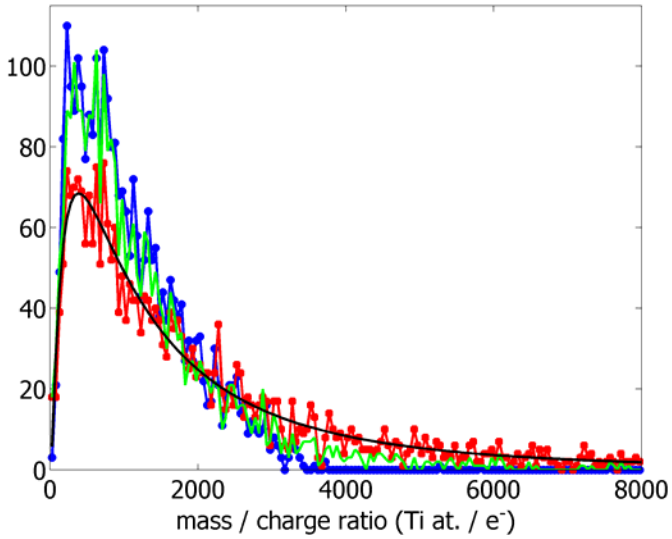

Figure 4.6: Comparison between 1) the measured m/q spectrum in the residence time window $8.5 - 14 - 5$ *ms* (blue); 2) the detected clusters mass spectrum reconstructed from the m/q data following the procedure described in the text (red); 3) the original mass distribution of detected clusters relative to the same residence time window, as described by equation (4.16) (black); 4) the m/q spectrum obtained from a simulated ionization process starting from the reconstructed original mass spectrum (green).

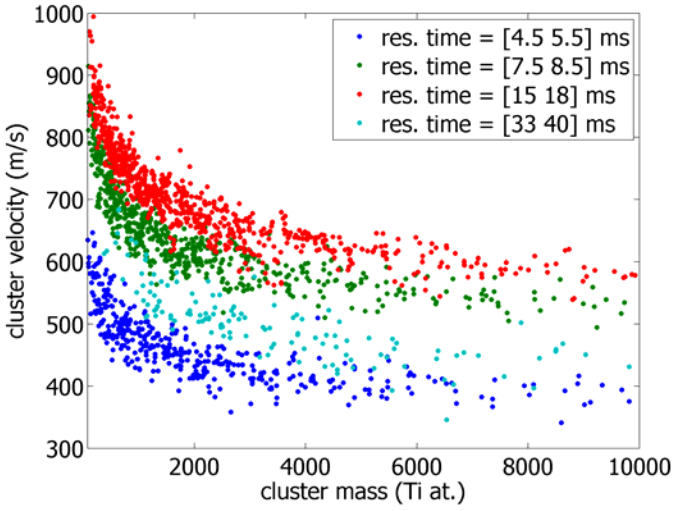

Figure 4.7: The velocity vs. mass scatter plot for clusters from selected residence time windows. The higher statistics available in this new experiment as compared to figure 4.2 is evident.

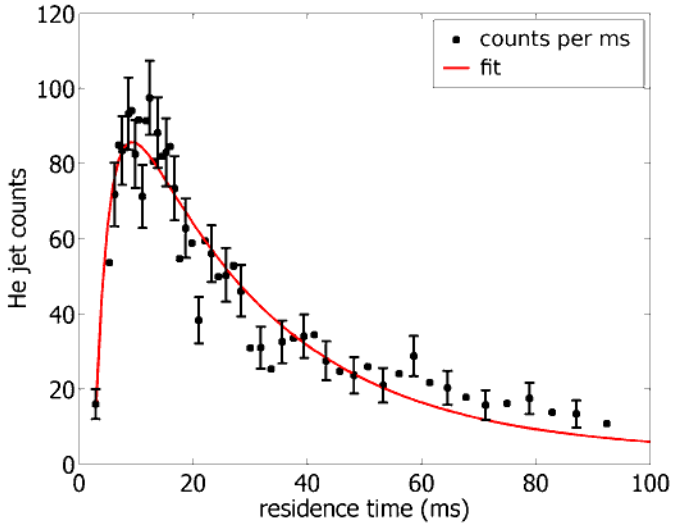

Figure 4.8: Evolution of He density in the jet with residence time, estimated by the number of counts per ms. The red curve represent the fit with the model reported in equation (4.17).

measurement of the concentration evolution of the carrier gas with residence time, and a consequential refinement of the rough approximation made in the first measurements for the concentration by assuming adiabatic expansion (see equation (4.5)).

The evolution of carrier gas concentration can be described by

$$n_{gas} = n_{gas,0} \cdot \left(1 - e^{-\frac{t-t_0}{\tau_1}}\right) \cdot e^{-\frac{t-t_0}{\tau_2}} \tag{4.17}$$

that is the superposition of two exponential curves: a fast exponential rise describing the finite time the carrier gas takes to traverse the focusing lenses, and a slow exponential decay reflecting the evolution of gas pressure inside the source. The experimental data fitted by this model are reported in figure 4.8.

Unfortunately a direct He velocity measurement for $[t_f, p]$ coordinates was not feasible because of the high dispersion of the velocity distribution (see figure 4.9a). This dispersion is most likely due to mutual electrostatic repulsion between He ions, but also the interaction with ions from the background gases could cause an additional velocity contribution.

An indirect measurement was possible by seeding the helium beam with argon atoms. The argon atoms are heavier and so less subject to Coulomb repulsion and

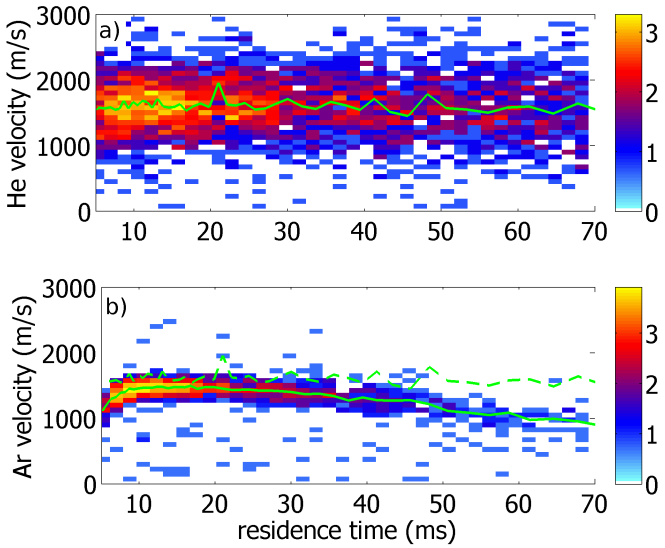

Figure 4.9: a) color map that represent the statistics of He velocity distribution vs. residence time, highlighting the huge broadening. The residence time evolution (green line), which is approximately constant, is consistent with the hypothesis that the expansion of the gas from the cluster source is isothermal. b) color map representing the Ar velocity distribution vs. residence time. The broadening is much lower than in the case of He, consistent with higher mass of Ar atoms. The green line represents the residence time dependent peak position of Ar velocity distribution; for comparison, also the He peak position is reported (dashed green line).

their velocity distribution in the beam is much better defined (see figure 4.9b). The evolution of Ar velocity with residence time was modeled with the equation (1.10), considering that from equations (1.11) and (4.4) follows

$$\beta \cdot \sigma = k \cdot n_{gas} \cdot m^{\xi} \tag{4.18}$$

assuming $m = m_{Ar}$, $\xi = 2/3$ and n_{gas} described by equation (4.17) and τ_1 and τ_2 derived by the fit of figure 4.8.

By considering the mean behavior of v_{He} (see figure 4.9a), among all the k-dependent solutions, the one that assumes constant v_{He} was chosen, that suggests that the expansion from the source is isothermal.

Figure 4.10a reports the solution of equation (1.10) for He velocity. Figure 4.10b reports the Ar velocity compared with the model solution for constant He velocity: the agreement is quite good.

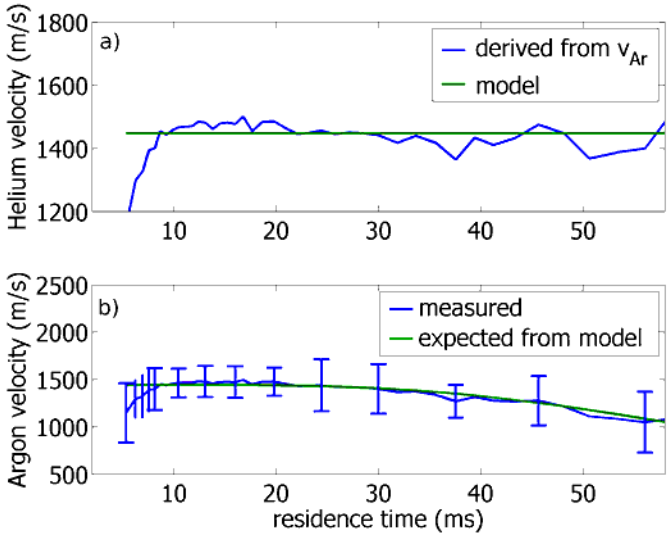

Figure 4.10: a) The solution for He velocity (blue line) which is closest to the hypothesis that the expansion from the cluster source is isothermal. The green line represent the average constant value. b) Evolution of Ar velocity with residence time compared with the model curve corresponding to a constant He velocity.

4.2.4 Accessing fractal dimension

The modeling of $v = v(m, t_{res})$ relation for clusters was performed by partially relaxing the assumption made in previous experiments (see section 4.1). In particular the main differences are:

- n_{He} is now an experimentally determined function of t_{res}.
- v_{He} is now also an experimentally determined function of t_{res}.
- k is a free parameter common to all t_{res} (see equation (4.18)).
- ξ is a t_{res} dependent parameter that from previous considerations (see section end of 4.1) can be assumed equal to $\xi = 2/D$. The fractal dimension D is then assumed to evolve exponentially with residence time from a maximum D_0 for $t_{res} = 0$ and a minimum D_∞ for $t_{res} \to \infty$ according to

$$D = D_\infty + (D_0 - D_\infty) \cdot e^{-\frac{t_{res}}{\tau}} \tag{4.19}$$

Figure 4.11 shows the dependence of the fractal dimension from residence time, as obtained by the fitting of the residence time dependent mass vs. velocity scatter

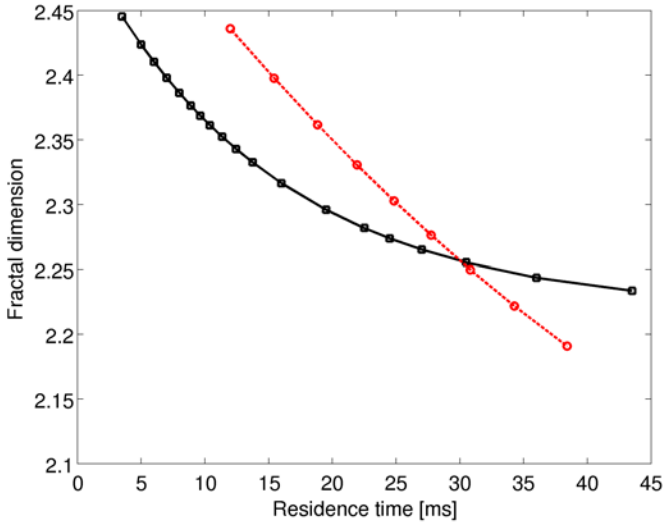

Figure 4.11: Residence time dependence of the fractal dimension in the FEL experiments (black line). For comparison is reported also the fractal dimension measured in the XAS experiments (red line).

plots (see figure 4.7) within the residence time interval $4 - 40$ *ms*.

4.3 Conclusions

The comparison of fractal dimension evolution with residence time in the XAS and FEL experiments shows a similar trend, that is a decrease of the fractal dimension with increasing residence time. Nonetheless the two evolutions are quantitative different: one reason is that in the latter experiments the model was more refined, but the main reason has to be found in the different mass distributions originating from different working regimes of the cluster source. In the XAS experiments the source was operated to get the maximum flux and thus a more intense sputtering was necessary leading to an increased aggregation and cluster size. On the other hand in the FEL experiment cluster size was remarkably smaller.

These results give quantitative and unambiguous confirmation of a picture already suggested for the interpretation of the fragmentation pattern involved in the interaction of clusters with soft x-ray photons [39], which describes the nano-objects formed by the PMCS as super-aggregates of primary particles rather than compact spherical-shaped objects. The decrease of the fractal dimension with de-

creasing stagnation temperature along with growing residence time, agrees qualitatively with common understanding of coagulation process: due to lower atomic mobility and lack of significant neck growth between colliding primary particles, coalescence slows down in the low-temperature conditions turning out in soft agglomerates with larger surface-to-volume ratio and excess surface energy [55] held together by Van der Waals forces [16].

Chapter 5

Photo-fragmentation of titanium clusters

Photo-fragmentation and ion momentum spectroscopy are techniques that have been widely used, along with photo-electron spectroscopy, in previous studies on the interaction of clusters with very intense photon beams [51, 24, 25, 6, 17].

Using the apparatus presented in section 2.3, we performed momentum resolved photo-fragmentation experiments on Ti clusters produced with the PMCS. Prior to the fragmentation experiment, the cluster beam has been characterized using FEL at low photon flux and employing SBMA technique (see section 4.2). This analysis gave information about the evolution of the original mass distribution of the clusters, before fragmentation, with residence time and provided a measure of their fractal dimension (see figure 4.11).

In this chapter, after a phenomenological analysis of the experimental results, the simulation approach that was developed in order to give a comprehensive explanation of the results is presented.

5.1 Analysis of fragmentation

In this section, the fragmentation process is analyzed in terms of its power dependence (in the range that spans from $6.0 \cdot 10^{12}$ W/cm^2 to $1.0 \cdot 10^{14}$ W/cm^2) and in its residence time dependence. The results are compared with the results on rare gas

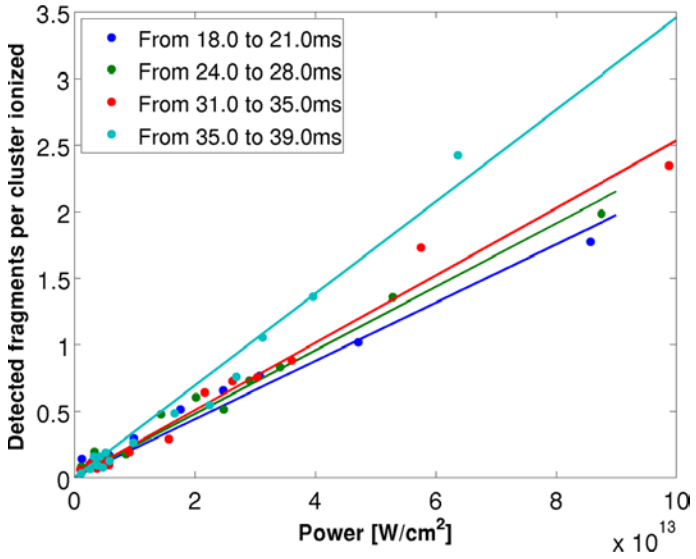

Figure 5.1: Number of detected fragments per cluster ionized (estimated) as a function of FEL intensity, for different residence time windows.

clusters from the literature and with experiments performed with the same sample, i.e. a molecular beam seeded with Ti clusters produced by the PMCS (with the same experimental conditions), using a doubled femtosecond Ti:Sapphire laser ($\lambda = 400\ nm$) as an excitation source.

5.1.1 Fragment yield

The first observable that can be taken into consideration is the fragment yield as a function of intensity. Ionization yield is expected to begin to evolve linearly at low intensities and then to show a saturation when non-linear processes begin to dominate.

Figure 5.1 reports the evolution of the fragmentation yield per ionized clusters as a function of FEL intensity. Surprisingly, the evolution seems to be linear up to a pretty high intensity, without any evidence of non-linear processes occurring. A more detailed analysis of the mass spectrum and of the fragment kinetic energy is reported next.

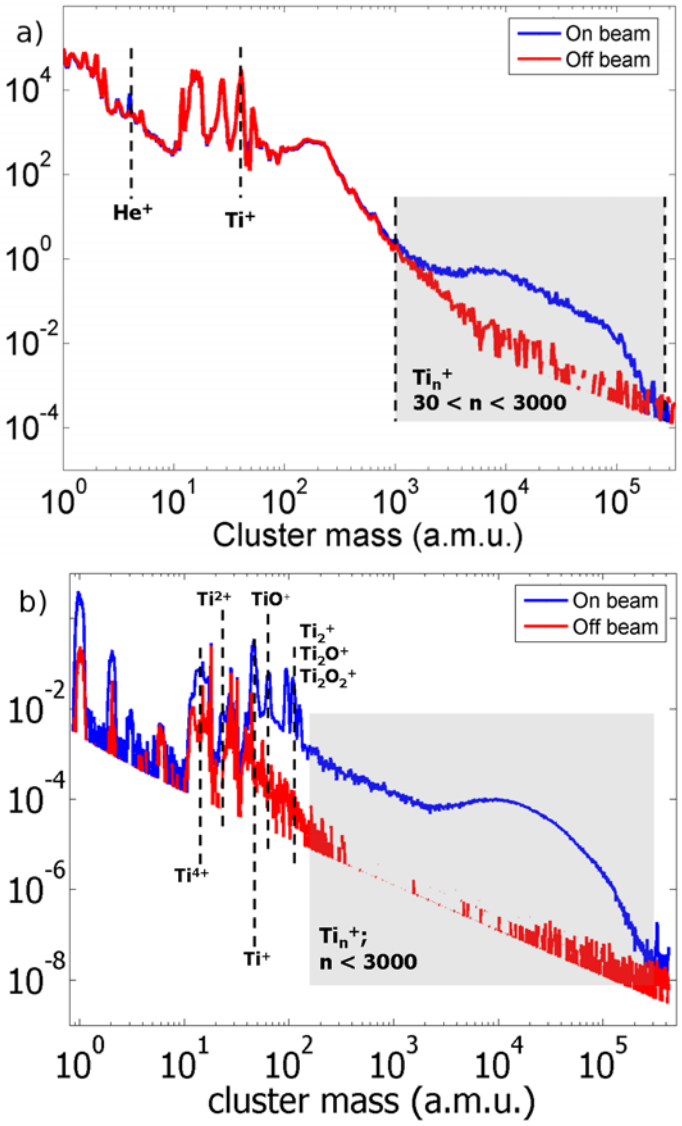

Figure 5.2: Comparison of the mass spectra of Ti clusters for experiments with the FEL (a) and with femtosecond laser (b). The red line is the background signal acquired off-beam, while the blue line is the mass spectra on-beam.

5.1.2 Ion mass spectra

What is generally expected when a cluster is exposed to an intense photon beam is a strong photon absorption, the formation of a nanoplasma and consequent Coulomb explosion. The two fingerprints of this process are the presence in the TOF spectrum of only highly charged atomic fragments (or at most very small fragments) [51, 24, 19] and an evolution of the kinetic energy of these fragments with the intensity of the photon beam [17, 49, 21].

With IR and visible femtosecond lasers, this shattering behavior is what is generally found with both rare-gas clusters and simple metal clusters (for a review see Fennel et al. [14]). With a VUV FEL source only experiments with rare-gas clusters have been performed to date and, even if the processes behind ionization and fragmentation are substantially different (see section 1.2.4), they show a similar picture.

Figure 5.2 shows the mass spectra of fragments resulting from the exposure of Ti clusters produced by the PMCS to femtosecond pulses in the VUV and visible wavelength ranges, with a power density comparable to that of the experiments done with rare gas clusters ($\sim 10^{12} - 10^{13} W/cm^2$).

The results are quite different from the generally expected results. Both experiments show an important contribution from heavy fragments that is missing in the previous experiments on rare-gas clusters. Moreover light fragments, that are a consistent part of the spectrum obtained by femtosecond laser excitation, are completely missing in the FEL measurements. The absence of atomic fragments in the fragment mass spectrum after FEL excitation cannot be related to a hindering effect by the very high signal from background ionization, as a detectable contrast should be observed anyway: a clear contribution to the spectra from doubly ionized helium can be still clearly identified.

A explanation of the observed behavior could be that the FEL focus was falling outside the molecular beam, thus exposing the clusters only to the lower photon flux present on the tails of the Gaussian beam profile; the comparison of measurements done with the same power density and different interaction volumes has demonstrated that this hypothesis can be discarded (see section 2.3 and figure 2.6).

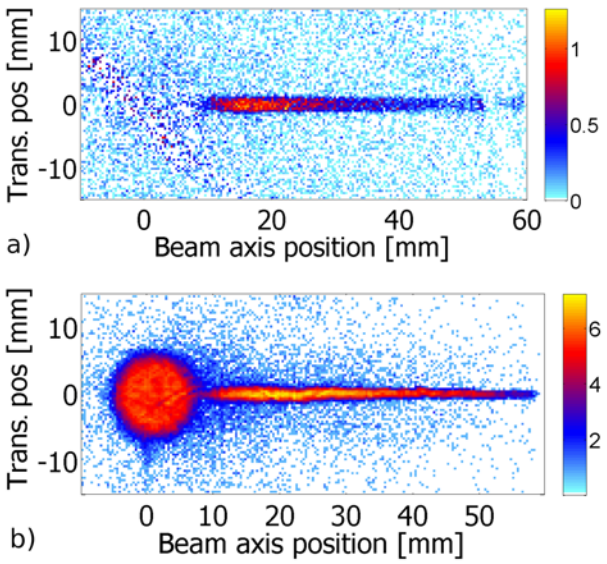

Figure 5.3: Comparison between the detector position maps of ions from experiment with the FEL (a) and with the femtosecond laser (b). In both cases the background has been subtracted.

5.1.3 Fragments kinetic energy

If a large amount of energy is absorbed by the clusters from the FEL beam, up to form a nanoplasma, the consequent fragmentation process should release this energy. This usually happens via the emission of many energetic electrons and fragments with high kinetic energy and charge state. Moreover, the kinetic energy distribution of the ions generally shifts to higher energies with the increase of laser intensity [17].

Kinetic energy of the fragments is identified by both the arrival position and time on the detector. If a broad energy distribution is present, this must be easily identifiable from the arrival position map. Figure 5.3 reports these maps for the experiments with the femtosecond visible laser and with the FEL. In the first case (figure 5.3b) two contributions can be distinguished: one from light fragments that exhibit high kinetic energy, and a second one from larger fragments, that show only the original momentum due to the acceleration undergone during molecular beam expansion. In the map from the FEL experiments (figure 5.3a) only the second contribution is present.

In the case of FEL excitation, the fragmentation process involves thus only the

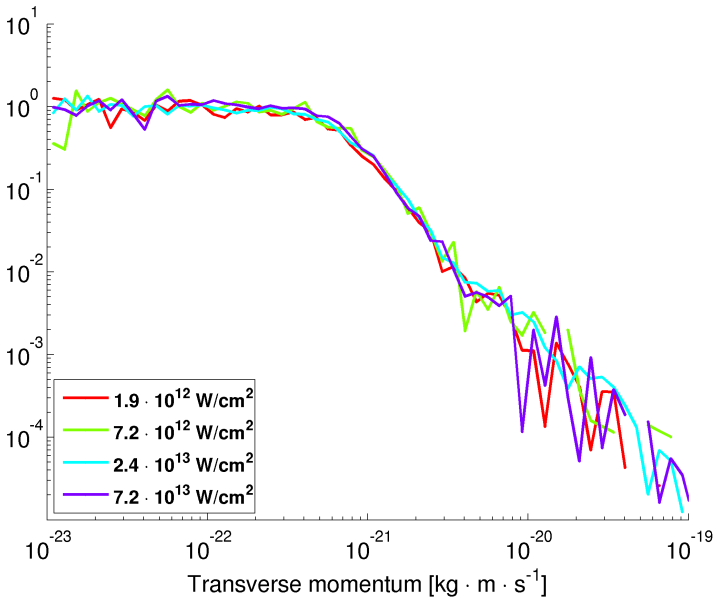

Figure 5.4: Comparison of the momentum component perpendicular the the molecular beam propagation direction of large fragments in the experiments with FEL at different photon beam intensities.

production of large fragments, that from the brief analysis described above does not show a relevant kinetic energy distribution. A more refined analysis of the kinetic energy release can be done for the large fragments by looking at the evolution of the momentum component perpendicular to the propagation direction of the molecular beam. Figure 5.4 reports the transverse momentum evolution of the large fragments as a function of FEL intensity: no relevant evolution is detected. The width of the distribution is mainly due to the native size of the molecular beam, which diameter is estimated to be around 1 *mm* in the interaction region.

Based on these results, the picture of the formation of a nanoplasma cannot hold. The fragmentation process can be identified as a fission process, that seems inconsistent with the expected extent of energy absorption in the intense beam from the FEL. One possible explanation is that in the case of complex covalent clusters the absorption process cannot be modeled simply with the atomic cross-section scaled by the number of atoms in the aggregate, as is generally assumed for the rare-gas clusters.

5.2 Interpretation of fragmentation: Montecarlo simulations

For the interpretation of the puzzling observations for the fragmentation yield dependence on cluster residence time inside the source and on FEL beam intensity, a simulation approach based on an empirical model was followed. The idea is to develop, starting from what is known from the literature, a simple empirical model for the ionization and fragmentation process that is able to reproduce quantitatively (after optimization of the parameters of a Montecarlo (MC) simulation) the fragmentation yields evolution with different residence times and FEL intensities.

The MC simulation code was then included inside a genetic algorithm framework that tries, through an extensive search of the entire phase space, to find the model parameters that are able to fit simultaneously all the fragmentation yields distributions for various residence times and intensities.

5.2.1 Genetic algorithm framework

The genetic algorithm approach was chosen instead of standard minimization algorithms, despite its intrinsically slower convergence, mainly because of two reasons: in the absence of a strong guide for the starting guess parameters it is more likely to find the global minimum of the objective function and it is more robust when dealing with a statistical quantity as the output of a MC simulation.

Some of the parameters of the model are fixed, or able to vary in a narrow range, and are determined by the experimental data. These parameters are:

1. The mass distribution, along with its dependence on residence time, that is derived from low photon flux measurements (see section 4.2.1).

2. The cluster fractal dimension, used in the electrostatic screening model of the clusters, that is derived from SBMA measurements (see section 4.2.4).

3. The target (sample) atomic density and its evolution with residence time, that is derived by the integrated mass flux detected by a quartz crystal microbalance.

4. The initial (outer) direct ionization, that is supposed to depend on the atomic ionization cross-section.

The unknown parameters of the simulation are:

1. The inner ionization cross-section.
2. The fragmentation model parameters.
3. The detector efficiency.

5.2.2 FEL-cluster interaction model

The MC code simulates a large number of ionization events ($10^4 - 10^5$ events), by following this scheme:

1. Generation of the number of clusters in the interaction volume by a Poisson deviate.
2. Assuming the clusters are uniformly distributed in the interaction region, generate for each of them the experienced photon intensity based on a Gaussian beam profile.
3. Generate for each cluster the value of its mass, by sampling a log-normal distribution.
4. Simulate inner and outer ionization yield for each cluster.
5. Simulate fragmentation and detection after accounting for finite efficiency.

The results of each ionization event are then summed up and contribute to populate the fragmentation yield distribution that is finally compared with the experimental one giving the score for that particular set of parameters.

Estimate of the interaction volume

The photon beam is assumed to have a Gaussian transverse profile. The peak intensity is calculated from the pulse energy measured by the intensity monitor and known FEL parameters. The limit of the interaction volume is assumed to be the point at which the intensity drops below a predefined cutoff threshold of

$2.0 \cdot 10^{14} {}^{ph}/_{cm^2}$, which is the photon flux that gives a ionization probability of atomic titanium of about 10^{-3}.

In the so determined volume, a Poisson's distributed number of cluster is generated. The mean number of clusters in the interaction volume, that is the parameter of the Poisson distribution, is determined by the concurrent estimate of the mean mass of the clusters and of the atomic density in the beam.

The clusters are then distributed uniformly in the radial direction in order to sample the entire range of intensities that are present in the interaction volume.

Ionization model

For each cluster generated in the interaction volume the ionization process is then simulated. The chosen ionization model employs the concepts of inner and outer ionization previously introduced (see section 1.2.4). From the electrostatic point of view, the cluster is considered as a sphere whose radius is connected to the number of atoms (or mass) by the fractal dimension as

$$r = r_s \cdot m^{1/D} \tag{5.1}$$

where r_s is the Wigner-Seitz radius of Ti.

The ionization potential of the cluster is then assumed to vary with charge z by pure electrostatic screening as

$$E_{ip} = E_\infty + \frac{1}{4\pi\epsilon_0}\left(z + \frac{1}{2}\right)\frac{e^2}{r} \tag{5.2}$$

where E_∞ is the ionization potential of bulk titanium.

Direct outer ionization of the cluster can thus occur until the IP overcomes the photon energy by building up of the Coulomb potential. The threshold number of photons that are absorbed can be estimated as

$$n_{ph} = \frac{E_{ph} - E_\infty - \frac{1}{4\pi\epsilon_0}\frac{e^2}{2r}}{\frac{1}{4\pi\epsilon_0}\frac{e^2}{r}} \tag{5.3}$$

The cluster is assumed to absorb photons by direct ionization up to this number, with the atomic cross section of Ti, that is $\sigma_{Ti} = 5 \cdot 10^{-18}\ cm^2$. After the threshold is reached, the photon absorption can continue by inner ionization, that is assumed

to be determined by a different empirical cross-section.

This gives the charge state due to direct ionization, plus the energy absorbed by the cluster by inner-ionization.

Fragmentation model

The fragmentation model is the core of the simulation and also the most critical ingredient for an effective reproduction of experimental results. At present two simple models from the vast literature on multi-fragmentation processes have been tested [50].

The first model simply assumed that the number of fragments should be Poisson distributed. The mean number of fragments was then connected to the number of charges in the clusters by an empirical model.

The second one modeled the fragmentation yield by a binomial distribution with parameters n and p_b, so that the probability of obtaining k fragments is described by

$$P_k = \binom{n}{k} \cdot p_b^k \cdot (1 - p_b)^{n-k} \tag{5.4}$$

Here n is interpreted as the number of "tries" the clusters do to emit a fragment, while p_b is the probability of a single fragment emission.

In accord with a fractal-like aggregate structure of our clusters, the number of "tries" is assumed to be connected to the number of primary particles in the cluster, that is a cluster tries to emit his primary particles, as the results from femtosecond laser experiments suggests, following this relation

$$n = \frac{m_{cl}}{m_{pp}} \tag{5.5}$$

The fragmentation probability is instead connected to the charge state of the cluster, by a distribution function that scales with the ratio between the cohesion energy (modeled by an empirical constant α) and the electrostatic repulsion, following this relation

$$p_b = e^{-\frac{\alpha \cdot r}{q^2}} \tag{5.6}$$

In both cases the finite efficiency of the detector is taken into account by the generation of random number in $(0,1)$ for each fragment and by counting only those that are within the efficiency range $(0,\epsilon)$.

5.2.3 Conclusions

The simulation code has proven to be stable, in the sense that its results are reproducible. The ionization and fragmentation models are the two critical points of the system and so the two parts that need to be improved in the future.

The ionization model implemented follows the general picture that is assumed for the ionization of rare-gas clusters. In the present case this model shows an excessive absorption and ionization of the clusters that is likely to be incompatible with the experimental results.

On the side of the fragmentation model, the simple Poisson distribution has proven to be quite good in the fitting of the fragments distributions at low FEL flux but at higher fluxes it predicts too many fragments, even with very low (and unlikely) detector efficiency (below 10%). The binomial model leads instead typically to more accurate results, but it still overestimates the number of fragments.

Chapter 6

Photo-electron spectroscopy of lead clusters

Both mass spectrometry and XPS can be exploited to obtain information about the size of nano-scale metal particles. The first by measuring their mass, whereas the latter can measure their dimension in space based on electrostatic properties of the system [38]. Despite these two measurements are sometimes regarded as redundant, this is not true when dealing with particles characterized by a complex morphology (see chapter 4).

By combining the results from the two types of characterization, performed independently on the same sample, it is possible to extract quantitative information about the structural properties of the system.

This section describes the results of the experiments performed on lead clusters produced by a PMCS. The complementary mass spectrometry analysis was done in the LGM laboratory in Milan, while the XPS characterization, considering photo-emission from the level 5d of lead, was performed at Max-Lab, with the apparatus described in section 2.2.

6.1 Mass distribution of lead clusters

The mass spectrometry was done with a linear TOF-MS in a Wiley-McLaren configuration, with a path in the field-free region of about 2.5 m. The ionization source

was an ArF excimer laser (Coherent Compex102) with wavelength of 193 nm ($E_{ph} = 6.43\ eV$), pulse length of $\sim 5\ ns$ and energy per pulse up to 160 mJ. The total photon flux was kept around $10^{15}\ {}^{ph.}/_{cm^2}$ per pulse, low enough to make sure that the average number of absorbed photons per cluster doesn't exceed one and thus to reduce fragmentation as much as possible.

A mass spectrum from Pb clusters (residence time window $20-55\ ms$) is shown in figure 6.1a. The dominating contribution to the spectrum can be modeled by a log-normal distribution with peak position around $1.2 \cdot 10^5\ {}^{amu}/_{e^-}$, corresponding to ∼600 Pb atoms per unit charge. According to the estimated interaction rate of the clusters in the beam with the laser (which results in 0.6 to 2 absorbed photons per cluster for this cluster size), this distribution can be assumed to be representative of the original cluster mass distribution yielded by the source. In fact, if the reported mass to charge ratio distribution was to be associated to a larger average size (resulting also in a larger expected number of absorbed photons), an ion yield at larger masses should be present, corresponding to the left tail of the Poisson distribution for the number of absorbed photon. Clusters ionized by a number of photons larger than one emit a corresponding number of electrons (until ionization potential exceed photon energy due to electrostatic screening) and eventually undergo fragmentation, yielding the features at the left side of the log-normal distribution in the mass spectrum. In a quantitative estimate of the fragmentation yield, it should be taken into account that the very small ($\sim 2 \cdot 10^{-4}\ sr$) solid angle subtended by the detector reduces the detection efficiency for fragment ions affected by a transverse momentum component. The detected spectral pattern from fragments is discussed in more detail below.

Residence time dependence of the original mass distribution peak position is shown in figure 6.1b. The slightly decreasing trend is not consistent with the expected increase in the average mass of the cluster population due to the growth process inside the source; this is explained taking into account that, for a given Stokes number, the mass of the clusters effectively coupled to the carrier gas stream lines in the focusing device decreases with decreasing pressure. Even though aggregation produces larger clusters at larger residence times, a decreasing focusing efficiency for larger masses results in the observed trend for the mass distribution parameter.

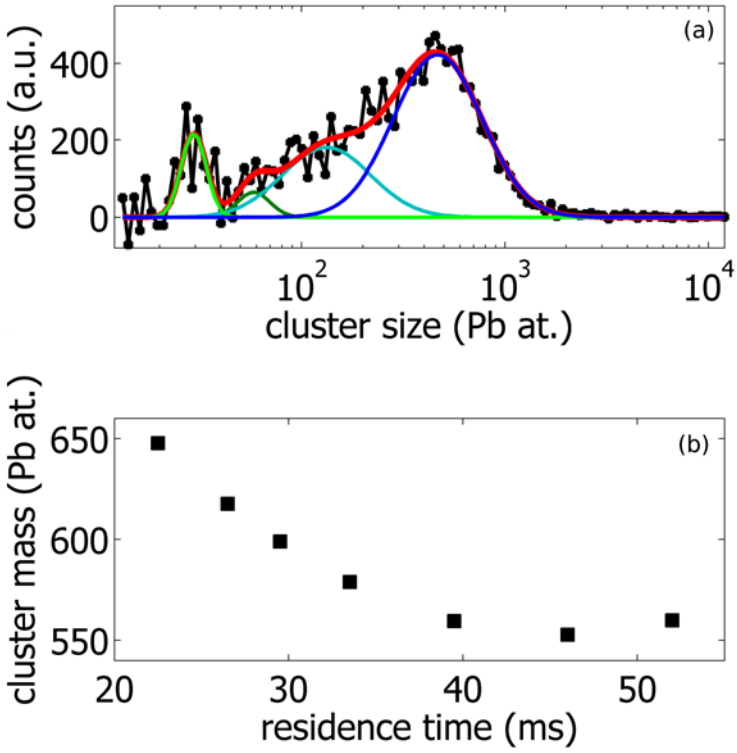

Figure 6.1: a) Time-of-flight mass spectrum from lead clusters with residence time $20 - 55\ ms$. The multi-mode character of the spectrum is represented by a fitting curve superposed to raw data and highlighted by the log-scale representation for the mass axis. The blue curve represent the original log-normal mass distribution centered around $1.2 \cdot 10^5\ a.m.u.(\sim 600\ at.)$. The contributions from multiply charged ions and fragments dominate the yield at low $^m/_q$ and are composed by a wide mode centered about 150 atoms and two sharper modes at 30 and 60 Pb atoms; as discussed in the text these two latter modes are assigned to primary particle fragments $(Pb_{30})_1$ and $(Pb_{30})_2$. b) Evolution with cluster residence time of the mode of the original cluster mass distribution as obtained from fitting of residence time resolved spectra.

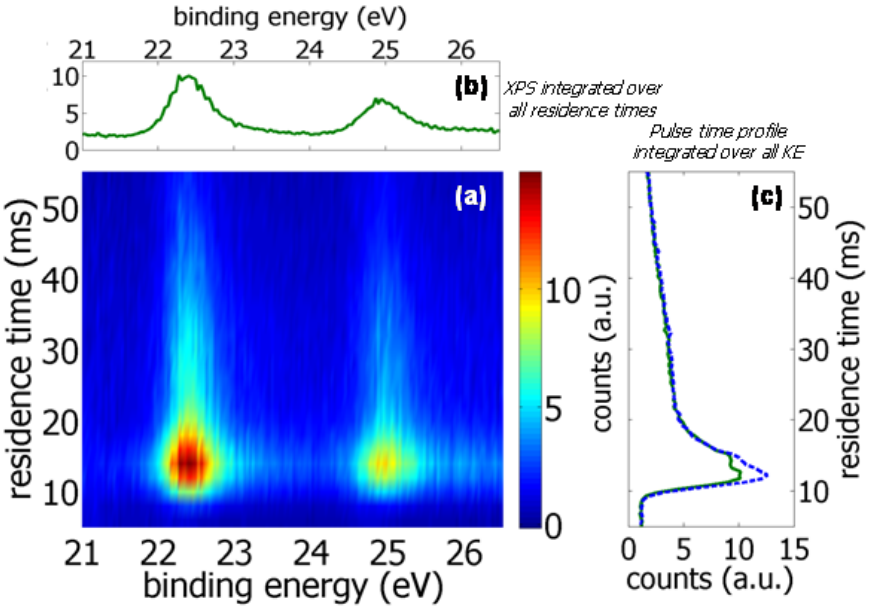

Figure 6.2: (a) Color map representation of the XPS spectra from the Pb 5d level for neutral lead clusters along the beam pulse. Horizontal sections provide residence time resolved XPS spectra, while vertical sections give cluster pulse profiles recorded at a given binding energy. (b) Photo-emission line corresponding to the integration of the yield map over the whole residence time range. (c) Pulse profile lines corresponding to the integration of the yield map over the whole energy window. Pulse profiles represent integral yield from neutral clusters only (green continuous line) and including native ions (blue dashed line).

6.2 Analysis of XPS line-shape

The size of lead clusters is estimated, based on a conducting sphere electrostatic model, from the analysis of the line-shape of core level photo-emission spectra represented in figure 6.2. If cluster mass is beyond the metal-to-nonmetal transition threshold, this model provides a good description of the electronic properties of the isolated metal nano-object. For lead clusters this threshold is around $n \sim 20$ atoms according to DFT calculations [52] and to recent experimental results [44], well below the average number of atoms of the photo-emitting clusters produced by the PMCS. Following the picture already discussed in literature (see Peredkov et al. [38] and Senz et al. [44]), a conducting Pb cluster with radius R and initial charge Z is then expected to yield a photo-emission line-shape which resembles the spectrum from solid Pb, after referring the binding energy to the vacuum level

through a size-dependent work function

$$W = W_{\infty} + E(R, Z) \tag{6.1}$$

where W_{∞} is the work function of the planar infinite solid (known for lead after ref. [38]) and $E(R, Z)$ is defined as

$$E(R, Z) = \left(Z + \frac{1}{2}\right) \cdot \frac{e^2}{R} \tag{6.2}$$

The 5d level photo-emission spectra of free Pb clusters from different residence time windows are compared with the photo-emission line from solid Pb in figure 6.3. The larger width and blue shift observed in the cluster spectra can be described as the superposition of the contributions from different cluster sizes and charge states populating the beam at a given residence time.

Like cluster sources employed in previous experiments [38, 44], the PMCS yields both neutral and ionic (positive and negative) clusters. The fraction of charged particles is generally residence time dependent and was estimated here comparing the total electron yield collected with and without applying a deflecting electrostatic field on the cluster beam before the interaction chamber. The neutral and neutral-plus-ions cluster beam profiles reported in figure 6.2c show that the contribution from ionic component of the beam is not negligible only in a restricted residence time window. Comparing the two corresponding photo-emission spectra from $11 - 16$ *ms* residence time window (figure 6.3) it is possible to identify the contribution from neutral clusters and to assign to the $Z = -1$ and $Z = +1$ charge states the additional peaks which can be singled out in the spectrum from neutral-plus-ions.

The $Z = -1$, $Z = 0$ and $Z = +1$ contributions can be modeled as the convolution between the infinite planar solid Pb photo-emission line and the "energy equivalent" of the residence time dependent cluster size distribution $E(R, Z)$, as defined in equation (6.2). As for cluster mass, also size R is log-normally distributed according to size distribution parameters μ_R, σ_R:

$$R(\mu_R, \sigma_R) = \frac{1}{r} \cdot e^{-\frac{(\log(r) - \log(\mu_R))^2}{2\log^2(\sigma_R)}} \tag{6.3}$$

By least-squares fitting the residence time resolved spectra from neutral clusters

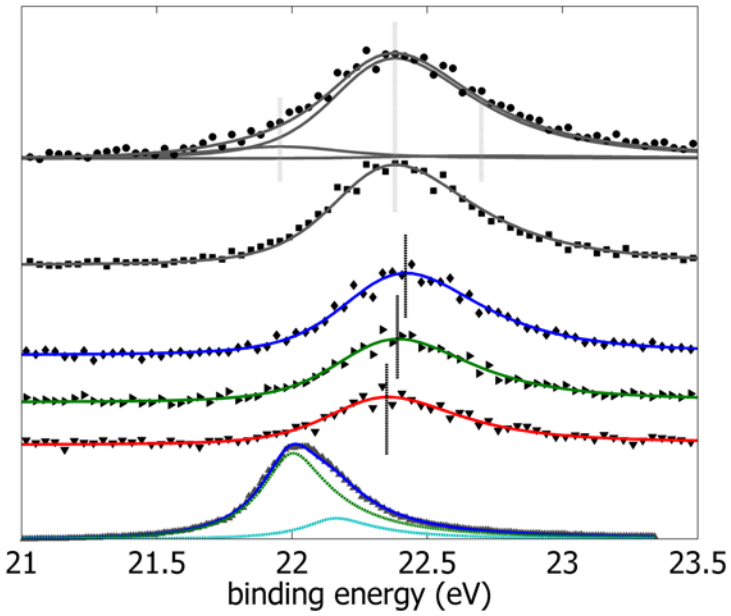

Figure 6.3: XPS spectra from the Pb $5d^5/_2$ level for different cluster beam samples compared with the photo-emission line from bulk Pb. Scatter plots represent (from the bottom to the top): 1) XPS from bulk Pb (upward gray triangles), from [11] and referred to vacuum level through work function value from [38]; the line is modeled (continuous blue line) as the superposition between inner site (dashed green) and surface site (dashed light blue) contributions, separated by [11]. 2) XPS from clusters with residence time $49-55$ *ms* (downward triangles), $31-36$ *ms* (rightward triangles), $20-25$ *ms* (rhombs) respectively, showing evident evolution with residence time in peak position. Continuous lines represent fitting spectra retrieved according to the model discussed in the text. 3) XPS from neutral (squares) and neutral-plus-ions (circles) clusters with residence time $11-16$ *ms*. Fitting curves express the same cluster size distribution for neutrals and ions; according to the fit the relative intensities are 84 neutrals, 12 anions, 4 cations. Due to the non-linear size-energy relationship the cationic contribution appears much broader and therefore much weaker than the anionic contribution. All spectra are represented after Shirley background subtraction; background calculation is included in the fitting procedure.

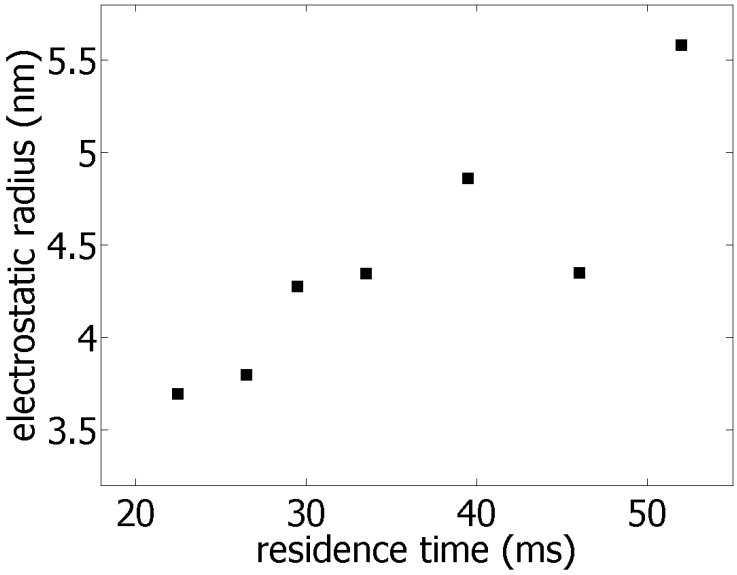

Figure 6.4: Evolution with residence time of the electrostatic radius calculated from the fitting procedure described in the text.

with the line-shape obtained with the described model, it is possible to estimate the cluster size distribution parameters μ_R and σ_R. The evolution with residence time of the cluster size mode μ_R is shown in figure 6.4.

According to the commonly accepted picture for what is usually referred to as a "cluster", the size (or radius) of the system should scale with the cubic root of the number of atoms or mass, as for compact spherical shaped objects. This is not the case for the system under study, as the increase of average cluster size (see figure 6.4) with residence time is not associated with the corresponding expected increment in the number of atoms per cluster (see figure 6.1b). This result confirms for lead clusters what is already known for titanium clusters from chapter 4, that is metal clusters produced by the PMCS are characterized by a complex fractal-like structure.

Like the Ti one, also Pb clusters can be described as super-aggregates of primary particles. Within this picture, a fractal dimension D_f can be included into the expression for the scaling law of the cluster radius with cluster mass

$$m = k \cdot \left(\frac{R}{r}\right)^{D_f} \tag{6.4}$$

where r is the primary cluster (primary particle) radius and k is a fractal dimension independent scaling factor. If m is expressed in terms of number of atoms and R, r are expressed in nanometers, $k = 137.3 \cdot (r\ [nm])^3\ \ at.$ from the expression valid for compact clusters

$$m = \frac{4\pi}{3} \cdot \rho \cdot R^3 \tag{6.5}$$

where ρ is the bulk density.

This scaling law can be applied to the average radius of many agglomerates with the same mass and primary particle size, but not to the radius of an individual agglomerate: agglomerates are not true fractals, as they are not infinitely scale invariant [55]. This is also the reason why fractal quantitative characterization needs a reference value (the primary particle radius) to scale the size of the cluster. Fractal dimension describes properly only large scale ($R \gg r$) behavior, i.e. clusters that are composed by a "large" number of primary particles.

The radius of primary particles, which may be regarded as compact spheres, can be here inferred from the analysis of the mass distribution of fragment ions (see figure 6.1a). The spectral pattern indicates as a preferential fragmentation pathway the emission of sub-clusters log-normally distributed around 30 Pb atoms; the observed feature is here interpreted as the contribution from primary particles coming from the fragmentation of super-aggregates under multiple photon absorption.

Figure 6.5 shows residence time evolution of the clusters' fractal dimension D_f retrieved from equation (6.4), after calculating the primary particle radius r corresponding to the observed mass spectrum feature according to

$$r = \left(\frac{3m}{4\pi\rho} \right)^{1/3} \tag{6.6}$$

The fractal dimension dependence of relative weight of surface and inner atoms is of course of relevance in an accurate development of the above-described model for the photo-emission spectral line-shape, because of the site-dependence of the photo-emission line position, related to the different coordination numbers of surface and inner atoms. In case of lead, the lines from surface sites and inner sites are split by 160 meV [11], well below the intrinsic peak width; overall peak position is then affected by the relative intensity of the two contribution. For precise clus-

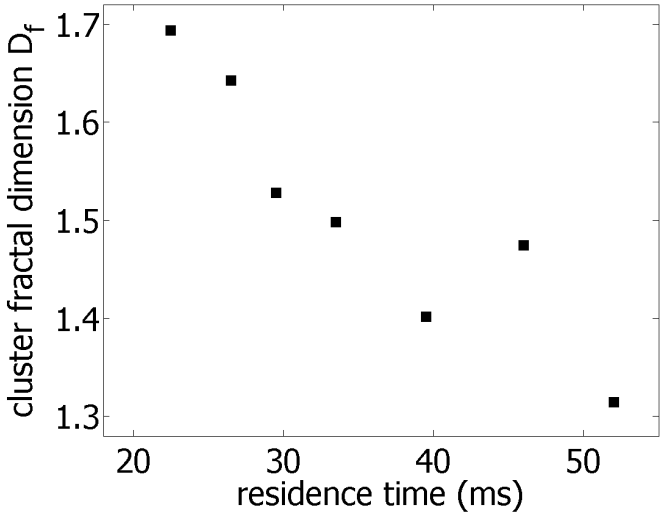

Figure 6.5: Evolution of the fractal dimension with cluster residence time.

ter size determination the D_f dependence of relative fraction of surface sites over the total number of atoms was then included in the spectrum fitting procedure for retrieving the size distribution parameters. Taking into account the complex morphology of the photo-emitting cluster, surface and inner site contributions have been assumed to be weighted by the same electron flux attenuation factor for retrieving the relative intensity in the photo-emission line.

Qualitative considerations about cluster morphology can be drawn based on the numerical values obtained for D_f. The $D_f = 2$ threshold is generally considered as discriminating between the "transparent behavior" ($D_f < 2$) and the "opaque behavior" ($D_f > 2$) [33]. For the case $D_f < 2$ the projection of the cluster does not fill the plane, and consequently in the asymptotic limit ($m \to \infty$) the surface area is proportional to the number of primary particles. Such a cluster is said to be asymptotically transparent, whereas in case of $D_f > 2$ in the projection operation some parts of the cluster are "hidden" by other parts of the same object, which is then opaque.

According to simulations performed by Meakin et al. [33], the two regimes discriminated by $D_f = 2$ can be put in relationship to different cluster-cluster aggregation models. In particular, a fractal dimension higher than 2 is obtained from ballistic aggregation with restructuring, whereas simulations based on the diffusion-limited aggregation model give clusters with a fractal dimension com-

parable to what reported here. A cluster-cluster aggregation where restructuring effects have a minority role is reasonably expected to be the dominating growth process in the very low temperature conditions of the PMCS.

The observed decreasing trend of D_f with residence time could be put into relationship with the concomitant decrease of stagnation temperature, even if a quantitative evaluation can be hardly attained as available studies based on molecular dynamics calculations do not explore this temperature range for estimating the temperature dependence of coalescence dynamics [57]. The trend is anyway qualitatively consistent with the increasing dependence of D_f on residence time reported from supersonic beam mobility measurements on Ti clusters (see chapter 4), although it should be taken into account that we are here dealing with two different kinds of measurement on two different systems.

Chapter 7

Conclusions and perspectives

Synchrotron radiation based techniques have been employed to characterize the structure and morphology of complex clusters produced by a PMCS. The results presented in this thesis have demonstrated the strong potential of techniques based on synchrotron radiation for the characterization of free nanoparticles.

X-ray absorption spectroscopy has shown how the structure of free carbon clusters evolves with residence time, moving from highly metastable clusters with high content of *sp* hybridization to more stable sp^2 clusters, an thus demonstrated how this technique can provide important insight into the dynamics of carbon particle aggregation processes.

The experiments on titanium clusters with the SCSS EUV free electron laser have combined mobility measurement in the supersonic beam with coincidence photo-fragmentation experiments; they confirmed that clusters produced by a PMCS are characterized by an evolving fractal-like structure and highlighted the fact that the cluster morphology is an important parameter in the determination of the relaxation dynamics of a nanoparticle exposed to a high intensity laser field. These preliminary results encourage the design of new experiments with the higher photon fluxes that will soon be available at the Fermi FEL under construction at Elettra.

FEL sources that became recently available in the soft X-ray spectrum will have a great importance for the development of the techniques whose early steps are reported in this work. They will, for example, open the possibility to extend photoelectron spectroscopy studies to most elements, and especially to those showing

more interest for applications that, due to the low cross-section, are exceedingly difficult to be studied with present synchrotron radiation sources.

The pioneering contribution to this new field from myself and the University of Milano group is provided and briefly described in this Thesis, with the hope and ambition to offer a useful overview to the next-coming explorers of a promising new way in nano-science.

Bibliography

[1] M. Arbeiter and T. Fennel. Ionization heating in rare-gas clusters under intense xuv laser pulses. *Phys. Rev. A*, 82(1):013201, 2010.

[2] M. Arbeiter and T. Fennel. Rare-gas clusters in intense VUV, XUV and soft x-ray pulses: Signatures of the transition from nanoplasma-driven cluster expansion to coulomb explosion in ion and electron spectra. arXiv:1011.2069v1, 2010.

[3] E. Barborini, P. Piseri, and P. Milani. A pulsed microplasma source of high intensity supersonic carbon cluster beams. *J. Phys. D Appl. Phys.*, 32(21):L105, 1999.

[4] R. Blyth, R. Delaunay, M. Zitnik, J. Krempasky, R. Krempaska, J. Slezak, K. Prince, R. Richter, M. Vondracek, R. Camilloni, L. Avaldi, M. Coreno, G. Stefani, C. Furlani, M. de Simone, S. Stranges, and M.-Y. Adam. The high resolution gas phase photoemission beamline, elettra. *J. Electron Spectrosc.*, 101–103:959–964, 1999.

[5] M. Bogana, L. Ravagnan, C. S. Casari, A. Zivelonghi, A. Baserga, A. L. Bassi, C. E. Bottani, S. Vinati, E. Salis, P. Piseri, E. Barborini, L. Colombo, and P. Milani. Leaving the fullerene road: presence and stability of sp chains in sp 2 carbon clusters and cluster-assembled solids. *New J. Phys.*, 7(1):81, 2005.

[6] C. Bostedt, H. Thomas, M. Hoener, E. Eremina, T. Fennel, K.-H. Meiwes-Broer, H. Wabnitz, M. Kuhlmann, E. Plönjes, K. Tiedtke, R. Treusch, J. Feldhaus, A. R. B. de Castro, and T. Möller. Multistep ionization of argon clusters in intense femtosecond extreme ultraviolet pulses. *Phys. Rev. Lett.*, 100(13):133401, 2008.

[7] M. Bässler, A. Ausmees, M. Jurvansuu, R. Feifel, J. O. Forsell, P. de Tarso Fonseca, A. Kivimäki, S. Sundin, S. L. Sorensen, R. Nyholm, O. Björneholm, S. Aksela, and S. Svensson. Beam line I411 at MAX II – performance and first results. *Nucl. Instrum. Meth. A*, 469(3):382–393, 2001.

[8] F. Calvo. Role of charge localization on the coulomb fragmentation of large metal clusters: A model study. *Phys. Rev. A*, 74(4):043202, 2006.

[9] J. Chen. NEXAFS investigation of transition metal oxides, nitrides, carbydes, sulfides and other interstitial compounds. *Surf. Sci. Rep.*, 30(1–3):1–152, 1997.

[10] Ž. Crljen and G. Baranović. Unusual conductance of polyyne-based molecular wires. *Phys. Rev. Lett.*, 98(11):116801, 2007.

[11] J. Dalmas, H. Oughaddou, G. L. Lay, B. Aufray, G. Tréglia, C. Girardeaux, J. Bernardini, J. Fujii, and G. Panaccione. Photoelectron spectroscopy study of Pb/Ag(111) in the submonolayer range. *Surface Science*, 600(6):1227–1230, 2006.

[12] S. DePaul, D. Pullman, and B. Friedrich. A pocket model of seeded supersonic beams. *The Journal of Physical Chemistry*, 97(10):2167–2171, 1993.

[13] P. S. Epstein. On the resistance experienced by spheres in their motion through gases. *Phys. Rev.*, 23(6):710–733, 1924.

[14] T. Fennel, K.-H. Meiwes-Broer, J. Tiggesbäumker, P.-G. Reinhard, P. M. Dinh, and E. Suraud. Laser-driven nonlinear cluster dynamics. *Rev. Mod. Phys.*, 82(2):1793–1842, 2010.

[15] A. C. Ferrari and J. Robertson. Theme issue 'raman spectroscopy in carbons: from nanotubes to diamond'. *Phil. Trans. R. Soc. Lond. A*, 362(1824):2269–2565, 2004.

[16] R. C. Flagan and M. M. Lunden. Particle structure control in nanoparticle synthesis from the vapor phase. *Mater. Sci. Eng. A*, 204(1-2):113–124, 1995. Proceedings of the Symposium on Engineering of Nanostructured Materials.

[17] H. Fukuzawa, X.-J. Liu, G. Prümper, M. Okunishi, K. Shimada, K. Ueda, T. Harada, M. Toyoda, M. Yanagihara, M. Yamamoto, H. Iwayama, K. Nagaya, M. Yao, K. Motomura, N. Saito, A. Rudenko, J. Ullrich, L. Foucar, A. Czasch, R. Dörner, M. Nagasono, A. Higashiya, M. Yabashi, T. Ishikawa, H. Ohashi, and H. Kimura. Dead-time-free ion momentum spectroscopy of multiple ionization of xe clusters irradiated by euv free-electron laser pulses. *Phys. Rev. A*, 79(3):031201, 2009.

[18] A. P. Hitchcock and C. E. Brion. Carbon k-shell excitation of C_2H_2, C_2H_4, C_2H_6 and C_6H_6 by 2.5 kev electron impact. *J. Electron Spectrosc.*, 10(3):317–330, 1977.

[19] M. Hoener, C. Bostedt, H. Thomas, L. Landt, E. Eremina, H. Wabnitz, T. Laarmann, R. Treusch, A. R. B. de Castro, and T. Möller. Charge recombination in soft x-ray laser produced nanoplasmas. *J. Phys. B: At. Mol. Opt. Phys.*, 41(18):181001, 2008.

[20] M. Huttula, S. Heinäsmäki, H. Aksela, E. Kukk, and S. Aksela. Multielectron effects in 4p photoionization of atomic cs. *J. Electron Spectrosc.*, 156–158:270–273, 2007.

[21] H. Iwayama, K. Nagaya, M. Yao, H. Fukuzawa, X.-J. Liu, G. Prümper, M. Okunishi, K. Shimada, K. Ueda, T. Harada, M. Toyoda, M. Yanagihara, M. Yamamoto, K. Motomura, N. Saito, A. Rudenko, J. Ullrich, L. Foucar, A. Czasch, R. Dörner, M. Nagasono, A. Higashiya, M. Yabashi, T. Ishikawa, H. Ohashi, and H. Kimura. Frustration of direct photoionization of ar clusters in intense extreme ultraviolet pulses from a free electron laser. *Journal of Physics B: Atomic, Molecular and Optical Physics*, 42(13):134019, 2009.

[22] O. Jagutzki, A. Cerezo, A. Czasch, R. Dorner, M. Hattas, M. Huang, V. Mergel, U. Spillmann, K. Ullmann-Pfleger, T. Weber, H. Schmidt-Bocking, and G. Smith. Multiple hit readout of a microchannel plate detector with a three-layer delay-line anode. *IEEE T. Nucl. Sci.*, 49(5):2477–2483, 2002.

[23] L. V. Keldysh. Ionization in the field of a strong electromagnetic wave. *Sov. Phys. JETP*, 20(5):1307–1314, 1965.

[24] T. Laarmann, A. R. B. de Castro, P. Gürtler, W. Laasch, J. Schulz, H. Wabnitz, and T. Möller. Interaction of argon clusters with intense vuv-laser radiation: The role of electronic structure in the energy-deposition process. *Phys. Rev. Lett.*, 92(14):143401, 2004.

[25] T. Laarmann, M. Rusek, H. Wabnitz, J. Schulz, A. R. B. de Castro, P. Gürtler, W. Laasch, and T. Möller. Emission of thermally activated electrons from rare gas clusters irradiated with intense vuv light pulses from a free electron laser. *Phys. Rev. Lett.*, 95(6):063402, 2005.

[26] N. D. Lang and P. Avouris. Oscillatory conductance of carbon-atom wires. *Phys. Rev. Lett.*, 81(16):3515–3518, 1998.

[27] N. D. Lang and P. Avouris. Carbon-atom wires: Charge-transfer doping, voltage drop, and the effect of distortions. *Phys. Rev. Lett.*, 84(2):358–361, 2000.

[28] I. Last and J. Jortner. Quasiresonance ionization of large multicharged clusters in a strong laser field. *Phys. Rev. A*, 60(3):2215–2221, 1999.

[29] I. Last, Y. Levy, and J. Jortner. Fragmentation channels of large multicharged clusters. *J. Chem. Phys.*, 123(15):154301, 2005.

[30] Z. Li and H. Wang. Gas-nanoparticle scattering: A molecular view of momentum accommodation function. *Phys. Rev. Lett.*, 95(1):014502, 2005.

[31] D. M. Lubman, C. T. Rettner, and R. N. Zare. How isolated are molecules in a molecular beam? *J. Phys. Chem.*, 86(7):1129–1135, 1982.

[32] T. Mazza. *Synchrotron Light Characterization of Free Metal and Oxide Nanoparticles*. PhD thesis, Università degli Studi di Milano, 2007.

[33] P. Meakin, B. Donn, and G. W. Mulholland. Collisions between point masses and fractal aggregates. *Langmuir*, 5(2):510–518, 1989.

[34] P. Milani and S. Iannotta. *Cluster beam synthesis of nanostructured materials*. Springer-Verlag, 1999.

[35] K. Motomura, L. Foucar, A. Czasch, N. Saito, O. Jagutzki, H. Schmidt-Böcking, R. Dörner, X.-J. Liu, H. Fukuzawa, G. Prümper, K. Ueda, M. Okunishi, K. Shimada, T. Harada, M. Toyoda, M. Yanagihara, M. Yamamoto, H. Iwayama,

K. Nagaya, M. Yao, A. Rudenko, J. Ullrich, M. Nagasono, A. Higashiya, M. Yabashi, T. Ishikawa, H. Ohashi, and H. Kimura. Multi-coincidence ion detection system for EUV-FEL fragmentation experiments at spring-8. *Nucl. Instrum. Meth. A*, 606(3):770–773, 2009.

[36] J. A. Nelson, R. J. Crookes, and S. Simons. On obtaining the fractal dimension of a 3d cluster from its projection on a plane-application to smoke agglomerates. *Journal of Physics D: Applied Physics*, 23(4):465, 1990.

[37] S. Peredkov, G. Öhrwall, J. Schulz, M. Lundwall, T. Rander, A. Lindblad, H. Bergersen, A. Rosso, W. Pokapanich, N. Mårtensson, S. Svensson, S. L. Sorensen, O. Björneholm, and M. Tchaplyguine. Free nanoscale sodium clusters studied by core-level photoelectron spectroscopy. *Phys. Rev. B*, 75(23):235407, 2007.

[38] S. Peredkov, S. L. Sorensen, A. Rosso, G. Öhrwall, M. Lundwall, T. Rander, A. Lindblad, H. Bergersen, W. Pokapanich, S. Svensson, O. Björneholm, N. Mårtensson, and M. Tchaplyguine. Size determination of free metal clusters by core-level photoemission from different initial charge states. *Phys. Rev. B*, 76(8):081402, 2007.

[39] P. Piseri, T. Mazza, G. Bongiorno, M. Devetta, M. Coreno, and P. Milani. CESyRa: A versatile setup for core-level absorption experiments on free metallic clusters using synchrotron radiation. *J. Electron Spectrosc.*, 166–167:28–37, 2008.

[40] L. Ravagnan. *Synthesis and Characterization of Carbynoid Structures in Cluster Assembled Carbon Films*. PhD thesis, Università degli Studi di Milano, 2005.

[41] L. Ravagnan, P. Piseri, M. Bruzzi, S. Miglio, G. Bongiorno, A. Baserga, C. S. Casari, A. Li Bassi, C. Lenardi, Y. Yamaguchi, T. Wakabayashi, C. E. Bottani, and P. Milani. Influence of cumulenic chains on the vibrational and electronic properties of $sp - sp^2$ amorphous carbon. *Phys. Rev. Lett.*, 98(21):216103, 2007.

[42] L. Ravagnan, F. Siviero, C. Lenardi, P. Piseri, E. Barborini, P. Milani, C. S. Casari, A. Li Bassi, and C. E. Bottani. Cluster-beam deposition

and in situ characterization of carbyne-rich carbon films. *Phys. Rev. Lett.*, 89(28):285506, 2002.

[43] G. Scoles. *Atomic and Molecular Beam Methods*, volume 1. Oxford University Press, 1987.

[44] V. Senz, T. Fischer, P. Oelßner, J. Tiggesbäumker, J. Stanzel, C. Bostedt, H. Thomas, M. Schöffler, L. Foucar, M. Martins, J. Neville, M. Neeb, T. Möller, W. Wurth, E. Rühl, R. Dörner, H. Schmidt-Böcking, W. Eberhardt, G. Gantefür, R. Treusch, P. Radcliffe, and K.-H. Meiwes-Broer. Core-hole screening as a probe for a metal-to-nonmetal transition in lead clusters. *Phys. Rev. Lett.*, 102(13):138303, 2009.

[45] T. Shintake, H. Tanaka, T. Hara, T. Tanaka, K. Togawa, M. Yabashi, Y. Otake, Y. Asano, T. Bizen, T. Fukui, S. Goto, A. Higashiya, T. Hirono, N. Hosoda, T. Inagaki, S. Inoue, M. Ishii, Y. Kim, H. Kimura, M. Kitamura, T. Kobayashi, H. Maesaka, T. Masuda, S. Matsui, T. Matsushita, X. Marechal, M. Nagasono, H. Ohashi, T. Ohata, T. Ohshima, K. Onoe, K. Shirasawa, T. Takagi, S. Takahashi, M. Takeuchi, K. Tamasaku, R. Tanaka, Y. Tanaka, T. Tanikawa, T. Togashi, S. Wu, A. Yamashita, K. Yanagida, C. Zhang, H. Kitamura, and T. Ishikawa. A compact free-electron laser for generating coherent radiation in the extreme ultraviolet region. *Nat. Photonics*, 2(9):555–559, 2008.

[46] H. Siekmann, C. Luder, J. Faehrmann, H. Lutz, and K. Meiwes-Broer. The pulsed-arc cluster ion-source (pacis). *Z. Phys. D-Atoms Mol. Clusters*, 20(1-4):417–420, 1991.

[47] J. Stöhr. *NEXAFS Spectroscopy*. Springer-Verlag, 1992.

[48] M. Tchaplyguine, S. Peredkov, H. Svensson, J. Schulz, G. Ohrwall, M. Lundwall, T. Rander, A. Lindblad, H. Bergersen, S. Svensson, M. Gisselbrecht, S. L. Sorensen, L. Gridneva, N. Martensson, and O. Bjorneholm. Magnetron-based source of neutral metal vapors for photoelectron spectroscopy. *Rev. Sci. Instr.*, 77(3):033106, 2006.

[49] H. Thomas, C. Bostedt, M. Hoener, E. Eremina, H. Wabnitz, T. Laarmann, E. Plönjes, R. Treusch, A. R. B. de Castro, and T. Möller. Shell explosion

and core expansion of xenon clusters irradiated with intense femtosecond soft x-ray pulses. *Journal of Physics B: Atomic, Molecular and Optical Physics*, 42(13):134018, 2009.

[50] M. B. Tsang and P. Danielewicz. Nuclear arrhenius-type plots. *Phys. Rev. Lett.*, 80(6):1178–1181, 1998.

[51] H. Wabnitz, L. Bittner, A. R. B. de Castro, R. Döhrmann, P. Gürtler, T. Laarmann, W. Laasch, J. Schulz, A. Swiderski, K. von Haeften, T. Möller, B. Faatz, A. Fateev, J. Feldhaus, C. Gerth, U. Hahn, E. Saldin, E. Schneidmiller, K. Sytchev, K. Tiedtke, R. Treusch, and M. Yurkov. Multiple ionization of atom clusters by intense soft x-rays from a free-electron laser. *Nature*, 420:482–485, 2002.

[52] B. Wang, J. Zhao, X. Chen, D. Shi, and G. Wang. Atomic structures and covalent-to-metallic transition of lead clusters $pb_n(n = 2 - 22)$. *Phys. Rev. A*, 71(3):033201, 2005.

[53] M. Weimer, W. Hieringer, F. D. Sala, and A. Görling. Electronic and optical properties of functionalized carbon chains with the localized hartree-fock and conventional kohn-sham methods. *Chem. Phys.*, 309(1):77–87, 2005.

[54] B. Wrenger and K. H. Meiwes-Broer. The application of a wien filter to mass analysis of heavy clusters from a pulsed supersonic nozzle source. *Rev. Sci. Instrum.*, 68(5):2027–2030, 1997.

[55] M. Wu and S. Friedlander. Enhanced power law agglomerate growth in the free molecule regime. *J. Aerosol Sci.*, 24(3):273–282, 1993.

[56] Y. Yamaguchi, L. Colombo, P. Piseri, L. Ravagnan, and P. Milani. Growth of $sp - sp^2$ nanostructures in a carbon plasma. *Phys. Rev. B*, 76(13):134119, 2007.

[57] M. R. Zachariah and M. J. Carrier. Molecular dynamics computation of gas-phase nanoparticle sintering: a comparison with phenomenological models. *J. Aerosol Sci.*, 30(9):1139–1151, 1999.